



Universiteit
Leiden
The Netherlands

Operando Spectro-electrochemical investigations of Pt and Pt-alloys as fuel cell catalysts

Nagra, H.J.

Citation

Nagra, H. J. (2025, September 25). *Operando Spectro-electrochemical investigations of Pt and Pt-alloys as fuel cell catalysts*. Retrieved from <https://hdl.handle.net/1887/4262106>

Version: Publisher's Version

License: [Licence agreement concerning inclusion of doctoral thesis in the Institutional Repository of the University of Leiden](#)

Downloaded from: <https://hdl.handle.net/1887/4262106>

Note: To cite this publication please use the final published version (if applicable).

Operando Spectro-electrochemical investigations of Pt and Pt-alloys as Fuel Cell Catalysts

Hassan Javed Nagra

Promotor:

Prof. dr. M. T. M. Koper

Co-promotor:

Dr. R. V. Mom

Promotiecommissie:

Prof. dr. M. Ubbink

Prof. dr. L.J.C. Jeuken

Prof. dr. J.M. van Ruitenbeek

Prof. dr. E. A. Lladó (AMOLF Amsterdam)

Dr. I. Khalakhan (Charles University, Prague)

The work presented in this thesis was financially supported by the Netherlands Organization for Scientific Research (NWO, grant # ECCM.TT.001).

ISBN: _____

Operando Spectro-electrochemical investigations of Pt and Pt-alloys as Fuel Cell Catalysts

Proefschrift

ter verkrijging van
de graad van doctor aan de Universiteit Leiden,
op gezag van rector magnificus prof.dr.ir. H. Bijl,
volgens besluit van het college voor promoties
te verdedigen op donderdag 25 september 2025
klokke 14.30 uur

door

Hassan Javed Nagra
geboren te Lahore, Pakistan
in 1992

Table of Contents

Chapter-1: Introduction.....	1
1.1 Oxygen Reduction Reaction and Polymer Electrolyte Fuel Cells.....	1
1.2 Degradation Mechanisms in a Fuel Cell.....	2
1.3 Near Ambient Pressure X-ray Photoelectron Spectroscopy.....	6
1.4 Soft X-ray Absorption Spectroscopy.....	8
1.5 Outline of the thesis.....	9
References.....	10
Chapter-2: A Laboratory based electrochemical NAP-XPS system for operando electrocatalysis studies.....	14
2.1 Introduction.....	15
2.2 System Design.....	16
i) In situ EC-XPS cell extension.....	17
ii) Membrane electrode assembly (MEA).....	19
2.3 Experimental Methods.....	22
2.4 Results.....	23
i) Pt oxidation in Acidic media.....	23
2.5 Conclusions.....	29
References.....	30
Chapter-3: A structural model for transient Pt oxidation during fuel cell start-up using electrochemical XPS.....	35
3.1 Introduction.....	36
3.2 Methods.....	37
i) Electrochemical measurements	37
ii) In situ X-ray spectroscopy	38
3.3 Results and Discussions.....	39

i) Electrochemical measurements	39
ii) In-situ oxidation of Pt.....	41
iii) Pt oxide thickness modelling.....	42
3.4 Conclusions.....	44
References.....	46
Chapter-4: The potential-dependent structure of Pt₃Ni alloy electrocatalysts and its effect on electrocatalytic activity.....	51
4.1 Introduction.....	52
4.2 Methods.....	53
i) In situ X-ray spectroscopy.....	53
ii) Electrochemical measurements.....	53
4.3 Results and Discussions.....	54
4.4 Conclusions.....	61
References.....	62
A: Supplementary Information for Chapter 2.....	67
A2.1 Manipulator and load lock design.....	68
A2.2 Main Chamber.....	69
A2.3 X-ray source and Analyzer.....	69
A2.4 Electrolyte and Gas Supply.....	70
A2.5 Safety Interlock System.....	71
i) Pressure Safety Interlock.....	71
ii) Power Failure Interlock.....	72
A2.6 Bake out.....	72
A2.7 Cleaning process.....	72
A2.8 Curve fitting parameters for Pt 4f.....	72
A2.9 SEM Images of graphene on MEA.....	73
References.....	75

B: Supplementary Information for Chapter 3.....	76
B3.1 In situ cell sample preparation.....	77
B3.2 Change in oxidation states of Pt with potential.....	77
B3.3 Catalyst wetting observed via XAS spectra.....	78
B3.4 XPS data fitting parameters.....	79
B3.5 Charge transfer calculation for the XPS data.....	80
B3.6 XAS experiments with consecutive voltage pulses.....	81
B3.7 Extended potential pulse experiments.....	81
B3.8 Modelling oxide layer thickness.....	82
B3.9 Ertl and Kupper's model.....	83
References.....	85
C: Supplementary Information for Chapter 4.....	86
C4.1 Nafion membrane activation.....	87
C4.2 Glassy carbon electrode preparation.....	87
C4.3 Membrane electrode assembly preparation.....	87
C4.4 Graphene deposition on Nafion MEA.....	87
C4.5 EDX sample analysis.....	88
C4.6 Cell design.....	88
C4.7 Pt 4f XPS data fitting.....	89
C4.8 Pt 4f/ Ni 2p peak area integration.....	90
C4.9 Pt ₃ Ni SEM.....	90
C4.10 XAS data processing for Ni L ₃ edge.....	91
C4.11 Pt & Pt ₃ Ni cyclic voltammetry and activity.....	92
C4.12 Ni 2p potential dependent XPS spectra.....	93
References.....	94
D: Summary & Outlook.....	95

Summary.....	96
Nederlandse samenvatting.....	98
Outlook.....	100
Perspectief op vervolgonderzoek.....	101
E: List of publications.....	102
F: Curriculum vitae.....	103
G: Acknowledgements.....	104

Chapter 1

Introduction

The notion that excessive CO₂ emissions from decades of burning fossil fuels has driven mankind to the verge of a dangerous environmental predicament, has already been thoroughly exhausted in just about every thesis, publication, conference paper and book report. It is assumed that the reader already has that context, so that this introduction can focus on the state of the art of the research concerning platinum and its alloys as fuel cell catalysts. Pulling on the thread that the devil is in the details, this thesis explores the intricacies of the electrode-electrolyte interface of Pt-based catalysts and their effects on electrocatalyst performance using X-ray spectroscopy techniques.

The overall theme of this thesis is to complement the electrochemical data acquired in fuel cell research with in situ X-ray photoelectron spectroscopy (XPS) and soft X-ray absorption spectroscopy (XAS). On the basis of recent theoretical and experimental studies in the literature, it has been revealed that electrocatalysts experience dynamic changes under experimental conditions, adapting their initial state to the changing environment^{1–3}. Therefore, in situ identification of these changes in the electrocatalyst is key to understanding the atomic features that are associated with the performance of the electrocatalyst, separating them from spectator species. Precisely decoding the atomic scale configurations under realistic operation conditions has been a long-standing challenge in the electrocatalysis community due to experimental challenges, which we try to address in this thesis. The methodology described in this thesis forms a general approach that can be used for a wide variety of electrocatalytic systems. However, here we have focused on the oxygen reduction reaction (ORR) on platinum based catalysts.

1.1 Oxygen Reduction Reaction (ORR) and Polymer Electrolyte Fuel Cells

Fuel cells have the potential to play a pivotal role in the green energy transition⁴. Their main role is to supply carbon neutral energy when and where it is needed using a renewable fuel such as green hydrogen. Platinum and its alloys are at present the benchmark catalysts for the widely used proton exchange membrane fuel cell (PEMFC) because of their relatively high stability and low activation barrier for both half-cell reactions, i.e. the hydrogen oxidation reaction and the ORR⁵ (see Figure 1.1). To understand the reaction environment that these Pt catalysts experience, I briefly describe the basic working principle of the PEMFC. The cell is divided into an anode and a cathode chamber, separated by a proton exchange membrane (e.g. Nafion). The anode and the cathode are connected electrically through an external circuit to which the cell delivers electrical power. Hydrogen gas is introduced into the anode chamber where it is oxidized into protons (Hydrogen Oxidation Reaction, HOR) which travel through the PEM membrane towards the cathode chamber. The electrons released during the hydrogen oxidation travel through the external circuit to the cathode where they combine with protons

and oxygen (from the air) to produce water via the oxygen reduction reaction (ORR). The Gibbs free energy change for the overall reaction is 237.14 kJ/mol_{H₂}, so that the fuel cell could theoretically deliver a potential of 1.23 V. However, energy losses within the fuel cell reduce the potential delivered when current is drawn. These energy losses arise to a large extent from the high activation barrier for the ORR⁶, making this a key research focus in fuel cell research.

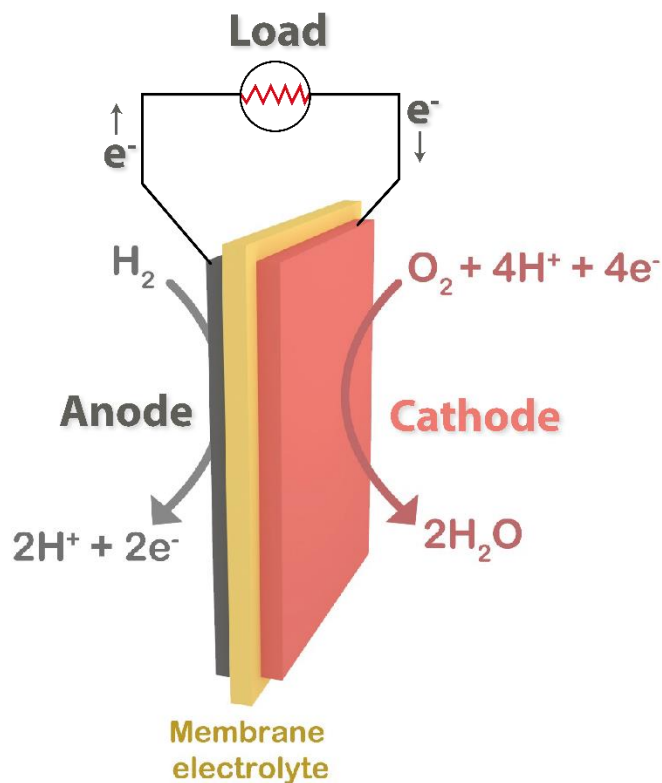


Figure 1.1: Schematic overview of a PEM Fuel Cell

Another key focus point for the research on Pt fuel cell catalysts is to lower the amount of Pt that is used in the catalyst film. The cost of the Pt in the fuel cell is one of the major hurdles towards its large-scale commercialization⁷, since the Pt catalyst cost alone makes up for 40-60% of the price of the fuel cell stack. In this regard, extensive research has led to the reduction in Pt loading in commercial fuel cells, from 28 mg_{Pt}cm⁻² to 0.4 mg_{Pt}cm⁻² at the cathode and 0.05 mg_{Pt}cm⁻² at the anode⁸, and there are continuous efforts to push towards even lower Pt loadings⁹. A key bottleneck for further reducing the catalyst loading is the degradation of the Pt catalyst on the cathode side during operation. Due to this degradation, an excess amount of catalyst has to be used to maintain long-term performance¹⁰. Therefore, understanding and mitigating Pt degradation is crucial to achieve affordable and long-term stable fuel cells.

1.2 Degradation Mechanisms in a Fuel Cell

There are a number of factors that are responsible for the decline in fuel cell performance over time such as platinum sintering, catalyst layer dissolution at the cathode and carbon support corrosion¹¹. All of these primarily occur during changes in the potential of the fuel cell, for example when the fuel cell is started or when more or less current is drawn. Under these conditions, Pt atoms can detach from the catalyst nanoparticles and dissolve as ions into the

polymer electrolyte. In part, these ions migrate towards the larger neighboring particles and attach to increase the particle size. This phenomenon is known as Ostwald ripening and becomes greater in magnitude with decreasing average particle size because of the greater thermodynamic driving force¹². Ostwald ripening leads to an increasing average particle size over time and a decrease in the electrochemically active surface area (ECSA)^{13,14}, which lowers the catalytic activity during the ORR. In addition to Ostwald ripening, migration of the dissolved Pt into the polymer membrane also presents a major challenge, as it constitutes a loss of active material.

First hints about the chemistry involved in the Pt dissolution can be extracted from the thermodynamics of Pt. As depicted in the Pourbaix diagram¹⁵ in Figure 1.2, metallic Pt is stable at potentials lower than $\sim 1.05 V_{\text{RHE}}$ whereas higher oxidation states PtO (Pt²⁺) and PtO₂ (Pt⁴⁺) are stable at more positive potentials^{8,16,17}. The onset oxidation on the surface of Pt nanoparticles starts a little earlier than predicted by the Pourbaix diagram (Figure 1.2), i.e. around $0.9 V_{\text{RHE}}$. In relation to this, the rate of loss of active surface area of the catalyst has been shown to increase at potentials above $0.9 V_{\text{RHE}}$. Furthermore, the dissolution rate is relatively much larger under dynamic potential conditions (load changes, startup/ shutdown) as compared to constant potential conditions (steady state operation)^{18–20}. Therefore, Pt dissolution has been linked to the formation and reduction of Pt oxides^{21,22}. Indeed, operando Pt dissolution measurements have shown that the Pt dissolution spikes during oxide formation and reduction, especially when the upper potential is $>1.3 V_{\text{RHE}}$ ^{23–25}. In fuel cells, this is situation occurs during start-up/shut-down. Under these conditions, the fuel cell cathode potential temporarily reaches values of $\sim 1.4 V_{\text{RHE}}$, causing significant oxidation of the surface²⁶. This potential spike lasts around a ~ 5 s before the potential returns to a steady state operation value ($0.7 V_{\text{RHE}}$ – $0.8 V_{\text{RHE}}$) and causes a significant dissolution of the catalyst, as discussed earlier^{26–30}. Despite that these start-up/shut-down potential spikes take up only a minute fraction of the operating time of a fuel cell, they cause around a 3rd of the overall deterioration^{26,31}, as shown in Figure 1.3. Due to this fast dissolution rate, (simulated) start-up/shut-down spikes are often used to study the mechanisms of Pt degradation.

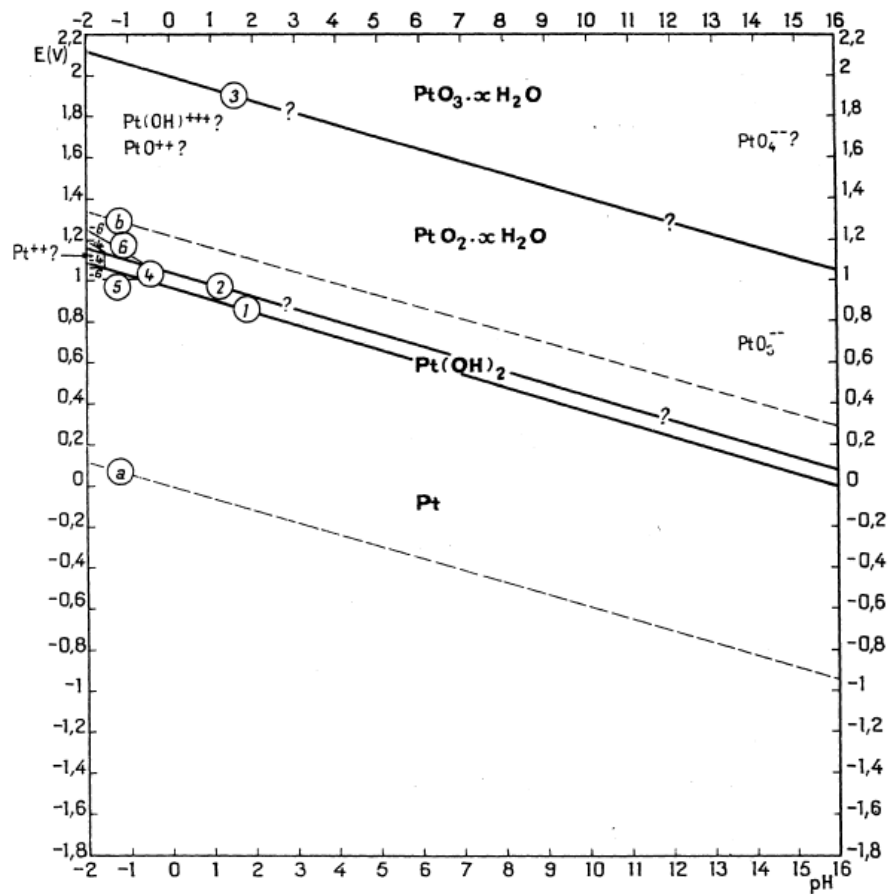


Figure 1.2: Potential-pH equilibrium diagram for the platinum-water system at 25°C¹⁵

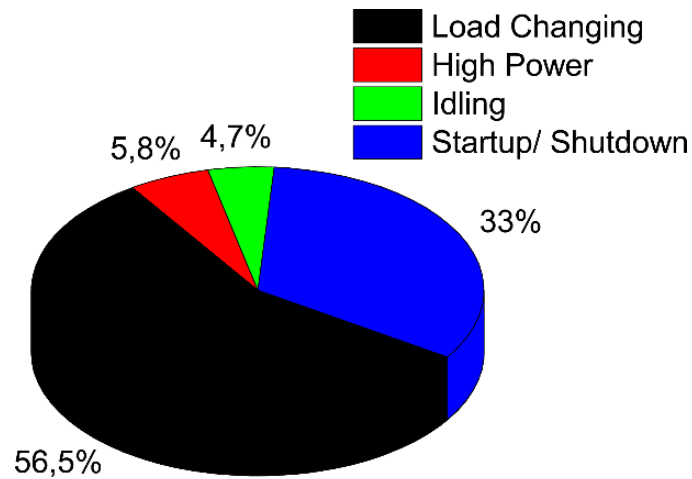


Figure 1.3: PEMFC degradation under different operating conditions³²

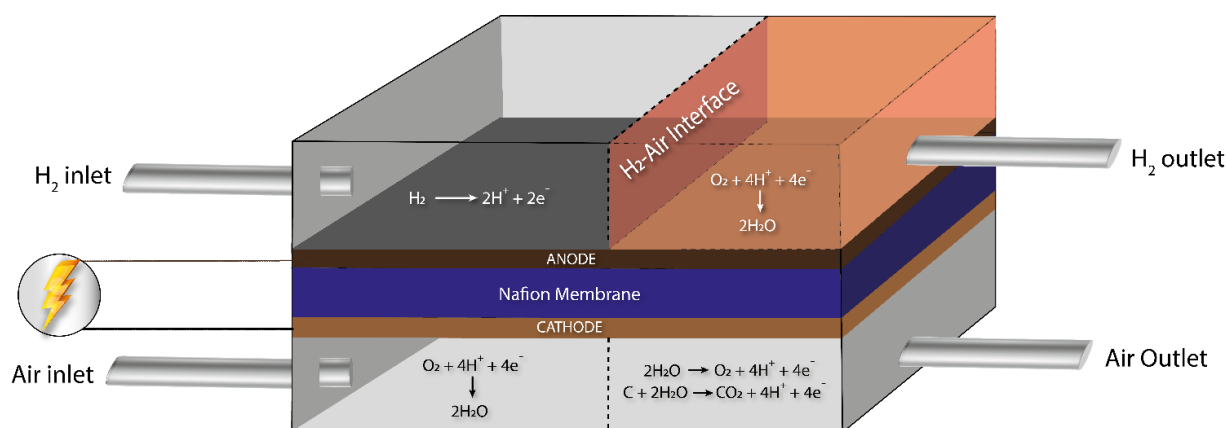


Figure 1.4: Establishment of H_2 -Air interface in the Anodic chamber of the fuel cell, causing large potential spikes at the cathode during startup/shutdown stages of the fuel cell

Zhang and coworkers³² have investigated the reasons behind the transient voltage spikes and concluded that the formation of a H_2 -Air interface (Figure 1.4) in the anodic chamber of the fuel cell produces momentary high potentials at the cathode surface, leading to oxidation of the catalyst as well as degradation of the catalyst support. Since the fuel cell startup and shut down fluctuations can be hard to simulate accurately, accelerated stress testing (AST) methods in regular liquid phase laboratory cells are frequently relied upon^{33–35}. This is exemplified in Figure 1.5, where it can be seen that transient voltage fluctuations indeed have a rapid degradation effect on supported Pt nanoparticle catalyst, visible as a loss in active surface area. We will make use of this methodology in Chapter 3.

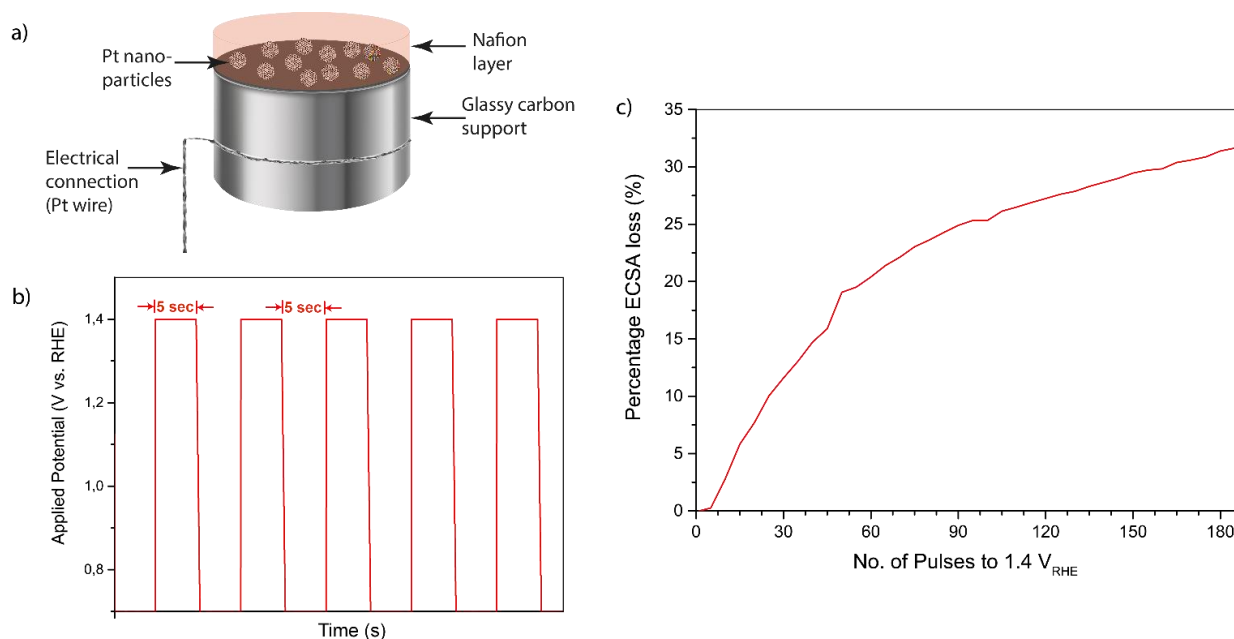


Figure 1.5: Pt transient degradation observed in 0.1 M H_2SO_4 electrolyte; a) shows 5 nm thick Pt nanoparticle catalyst sputter deposited onto a polished glassy carbon working electrode and coated with Nafion ionomer, b) shows the potential applied simulating transient voltage pulses, with 5 second duration for peak (1.4 V_{RHE}) and base (0.7 V_{RHE}) potentials and c) shows the progressive loss of active surface area as a consequence of transient degradation

While the discussion above shows that the conditions leading to fuel cell degradation are fairly well understood, the molecular-scale mechanisms for Pt degradation remain a debated topic in the electrochemical community. The integration of in situ X-ray spectroscopy alongside conventional electrochemical measurements has a strong potential for unraveling these mechanisms, as it offers the possibility to directly couple electrochemical signals to atomic-scale surface structures. In this thesis, I will explore this direction using in situ X-ray photoelectron spectroscopy and soft X-ray absorption spectroscopy.

In our Spectro-electrochemical studies, we have focused not only on pure Pt catalysts, but also on a Pt₃Ni alloy. In recent years, alloying Pt with transition metal catalysts such as Ni and Co has emerged as a highly effective strategy to improve the activity and stability of the fuel cell catalyst. Through modulation of the (electronic) structure of the surface Pt layers^{36,37}, Pt-Ni alloy catalysts to have exceptionally high ORR activity when compared to benchmark commercial Pt catalysts^{38,39}. Also, catalyst degradation studies on Pt-alloy catalysts have revealed the suppression of mechanisms such as coalescence and Ostwald ripening⁴⁰.

1.3 Near-ambient Pressure X-ray Photoelectron Spectroscopy

To facilitate the Spectro-electrochemical analysis of my samples and to be able to do that independent of the time and logistical limitations of the synchrotron, I undertook the task of commissioning the in situ X-ray Photoelectron Spectroscopy set-up at our own lab in the Leiden Institute of Chemistry. From buying the smallest of the screws to facilitating the purchase of the analyzer module, today it stands in all its glory measuring both ex situ and in situ electrochemical samples. The purpose of this section is to refresh the reader's knowledge about the working principle of in situ XPS.

Starting off with the customary tribute to the inventors, the concept of XPS is based on the photoelectric effect discovered by Heinrich Hertz in 1887. Photoemission as a result of irradiation by X-rays was first discovered in 1914 by Robinson and Rawlinson, and its first demonstration as a method of material analysis can be accredited to Steinhardt and Serfass in 1951⁴¹. The bulk of the work done to formally develop XPS as it is used today is attributed to Kai Siegbahn from the University of Upsala in the 1970s, for which he was awarded the Nobel prize in 1981⁴².

XPS is a surface-sensitive technique where soft X-rays (<2 keV) are bombarded onto the sample, which excites electrons inside the material^{43,44}, as shown schematically in Figure 1.6. The electrons absorb the photon energy and are expelled from the material, after which their kinetic energy is measured by the electron energy analyzer. The emission of the electron is a result of complete transfer of the photon energy to the electron, which can be expressed mathematically through Equation 1⁴⁵.

$$h\nu = B.E + K.E + \phi_{\text{spectrometer}} \quad (1)$$

where $h\nu$ is the energy of the incoming X-rays, B.E and K.E are the binding energy and the kinetic energy of the core electron and $\phi_{\text{spectrometer}}$ is the spectrometer work function, which is a constant. Using Equation 1, the measured kinetic energy can be converted into a binding energy. This binding energy is typical to the element and core level from which the electron

was ejected. Consequently, an XPS spectrum displays separate peaks for every element and core level, as exemplified in Figure 1.7.

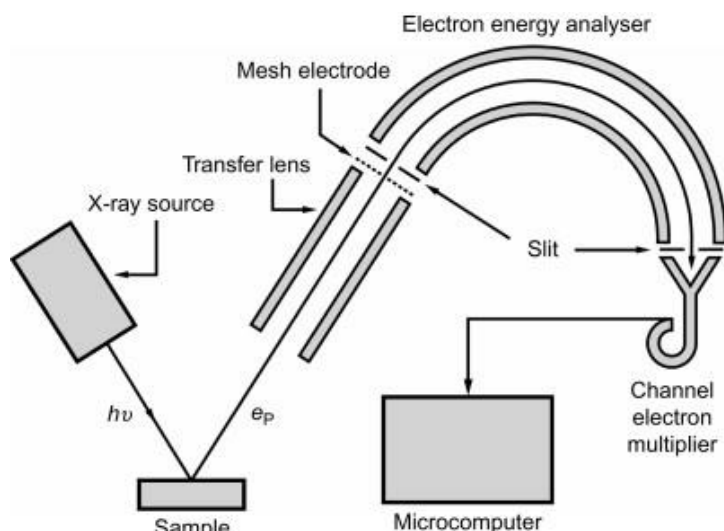


Figure 1.6: Working principal of the XPS ⁴⁶

Figure 1.7 shows the XPS survey spectrum of a gold single crystal electrode, where the peaks from different Au core levels can be seen. The spectrum also shows O 1s and C 1s peaks, originating from adsorbates on the surface. This sensitivity to surface species is a key property of XPS, which originates from the measurement principle: only the photo-electrons emitted a few nanometers from the surface will be able to make it out of the sample to reach the detector. As a result, the detected XPS signal only reflects the properties of the top 1-8 nm of the sample.

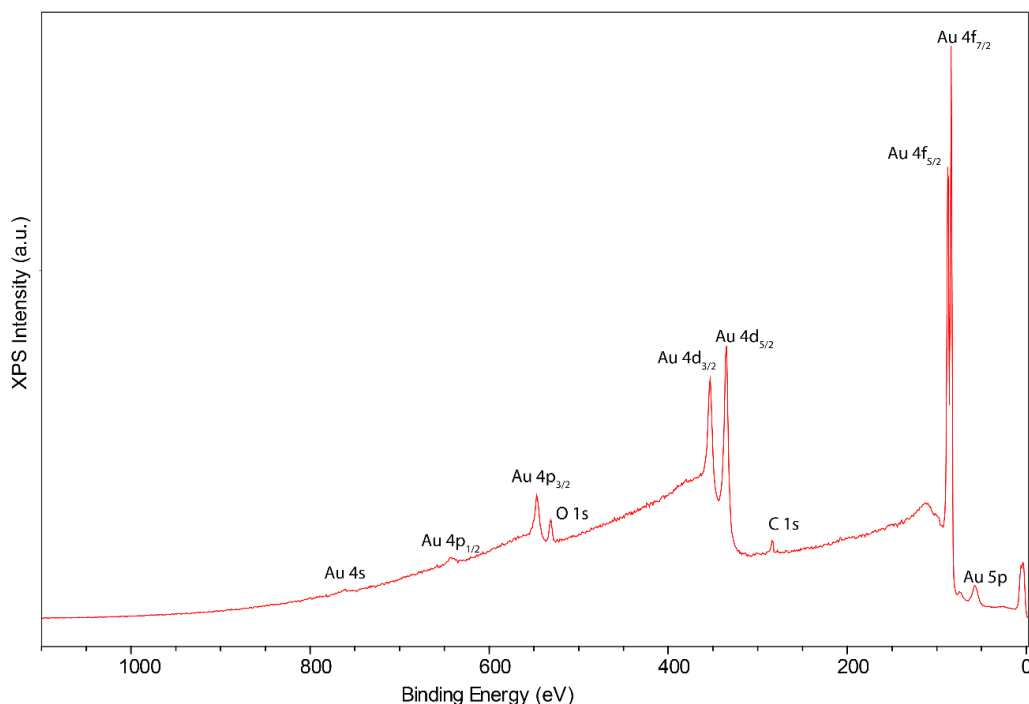


Figure 1.7: XPS Survey spectrum of an Au electrode

XPS experiments are normally done in an ultra-high vacuum environment to reduce the scattering of the emitted photoelectrons by gas phase molecules as they fly from the sample to the detector, and to avoid surface contamination. Also, the X-ray source operates at a very high voltage (~ 15 kV) and will cause arcing even at low vacuum pressures.

In near-ambient pressure XPS (NAP-XPS), the latter problem is solved by introducing a silicon nitride (SiN_x) window, which separates the measurement chamber from the X-ray source enabling the measurement chamber to operate at a higher (near-ambient, ~ 1 mbar) pressures while the X-ray source is at a high vacuum. In addition, several differential pumping stages are placed between the main chamber and the electron energy analyzer, producing ~ 9 orders of magnitude reduction in pressure. This greatly reduces scattering of the photoelectrons with gas molecules, making it possible to detect photoelectrons while there is a mbar pressure in the main chamber. In this way, the catalyst-adsorbate interaction can be probed under reaction conditions, which is critical for correlating the activity and stability of a catalyst with the change in its structural properties under reaction conditions.

The instrument present in our lab is an electrochemical NAP-XPS, which is capable of doing precisely that; resolving the oxidation states at the surface as well as the chemical state of the adsorbates under electrochemical conditions. To maintain a stable electrolyte film on the electrode surface under vacuum conditions, the electrocatalyst is sandwiched between a membrane and bilayer graphene, as further detailed in *Chapter 2*. Previously, access to membrane-based electrochemical XPS was limited to a few synchrotron beamlines in the world and even those were highly limited in the choice of electrolytes. Our setup removes both of these limitations and allows us to employ XPS to investigate changes in both sides of the electrode-electrolyte interface as a function of applied potential. This enables us to study a wide array of reactions under operando electrochemical conditions. The details of this instrument will be discussed in *Chapter 2* of this thesis.

1.4 Soft X-ray Absorption Spectroscopy

Another spectroscopy technique that was employed using the same experimental geometry, was soft X-ray Absorption Spectroscopy (XAS). XAS is a powerful tool which yields element-specific information about the unoccupied states in the electronic structure of the catalyst. Unlike XPS, the X-ray energy is swept during a measurement, and the X-ray absorption as a function of X-ray energy is measured. Due to the requirement of a tunable X-ray energy, one needs to go to a synchrotron facility for the measurements.

In the studies presented in this thesis XAS is used to complement XPS. The excitations of core electrons to unoccupied valence states are highly sensitive to the bonding environment of an atom, often more so than in XPS. In the following chapters, we will exploit this sensitivity to track subtle changes in the bonding configuration and electronic structure of the catalyst.

The photon energy of the X-rays defines the type of XAS being used; they are broadly categorized into soft (< 2 keV), tender ($2\text{--}5$ keV) and hard X-rays (> 5 keV)⁴⁷. Due to the nature of absorption edges required in the research work presented in this thesis, we rely on soft X-rays for our XAS measurements.

1.5 Outline of the thesis

This thesis aims to combine electrochemical measurements with in situ electrochemical X-ray spectroscopy to explore the (near) surface chemistry of fuel cell catalysts, addressing the mechanisms responsible for their activity and stability.

Chapter 2 presents the details of the in situ electrochemical NAP-XPS commissioned at Leiden Institute of Chemistry. We provide the details of the design and the components used to construct the instrument, and highlight its application to study all components of the electrode-electrolyte interface in electrochemical systems using the case study of the Pt-0.1 M H₂SO₄ interface.

Chapter 3 explores the evolution of oxidation states of Pt within the potential range relevant for fuel cell start-up degradation. We present a data model comparing the electrochemical signals measured during AST cycles to the oxidation state evolution detected by in situ spectroscopy, which directly links electrochemistry to the surface oxide structure on the Pt nanoparticles.

Chapter 4 describes the potential-dependent restructuring of a Pt₃Ni alloy catalyst. We show that, even though the catalyst surface of the Pt-alloy catalyst is composed of pure Pt, the subsurface Ni takes part in the surface chemistry via electron density donation and subsurface migration. We show that this migration has a profound effect on the catalytic activity of the material, making the catalytic properties of the Pt-Ni alloy potential-dependent.

I believe that in order design the optimal fuel cell catalyst, we have to improve our understanding right down to the Pt atom, understand its environment, see what it sees at reaction conditions, so in short: try to observe the world from its point of view. Through the course of these chapters, we try to achieve that by recreating those conditions and then probing them spectroscopically in real time to improve the atomistic understanding of the electrode-electrolyte interface. I hope the readers find that journey as insightful as I did.

References

- (1) Chang, C. J.; Lin, S. C.; Chen, H. C.; Wang, J.; Zheng, K. J.; Zhu, Y.; Chen, H. M. Dynamic Reoxidation/Reduction-Driven Atomic Interdiffusion for Highly Selective CO₂ Reduction toward Methane. *J Am Chem Soc* **2020**, *142* (28), 12119–12132. <https://doi.org/10.1021/jacs.0c01859>.
- (2) Wang, J.; Tan, H. Y.; Zhu, Y.; Chu, H.; Chen, H. M. Linking the Dynamic Chemical State of Catalysts with the Product Profile of Electrocatalytic CO₂ Reduction. *Angewandte Chemie - International Edition* **2021**, *60* (32), 17254–17267. <https://doi.org/10.1002/anie.202017181>.
- (3) Zhu, Y.; Wang, J.; Chu, H.; Chu, Y. C.; Chen, H. M. In Situ/ Operando Studies for Designing Next-Generation Electrocatalysts. *ACS Energy Letters* **2020**, *5* (4), 1281–1291. <https://doi.org/10.1021/acsenergylett.0c00305>.
- (4) Zawodzinski, C.; Gottesfeld, S.; Materials, E.; Group, D.; Lahoralory, L. A. N.; Alamos, L. PEM Fuel Cells for Transportation and Stationary Generation Applications. *International Association of Hydrogen Energy* **1997**, *22*, 1137–1144.
- (5) Rasmussen, K. D.; Wenzel, H.; Bangs, C.; Petavratzi, E.; Liu, G. Platinum Demand and Potential Bottlenecks in the Global Green Transition: A Dynamic Material Flow Analysis. *Environ Sci Technol* **2019**, 11541–11551. <https://doi.org/10.1021/acs.est.9b01912>.
- (6) Borup, R.; Meyers, J.; Pivovar, B.; Kim, Y. S.; Mukundan, R.; Garland, N.; Myers, D.; Wilson, M.; Garzon, F.; Wood, D.; Zelenay, P.; More, K.; Stroh, K.; Zawodzinski, T.; Boncella, X. J.; Mcgrath, J. E.; Inaba, O. M.; Miyatake, K.; Hori, M.; Ota, K.; Ogumi, Z.; Miyata, S.; Nishikata, A.; Siroma, Z.; Uchimoto, Y.; Yasuda, K.; Kimijima, K.; Iwashita, N. Scientific Aspects of Polymer Electrolyte Fuel Cell Durability and Degradation. *Chem Rev* **2007**, *107* (10), 3904–3951. <https://doi.org/10.1021/cr050182l>.
- (7) US Department of Energy. Heavy-Duty Fuel Cell System Cost - 2022. *DOE Hydrogen and Fuel Cells Program Record* **2023**, 1–11.
- (8) Yousfi-steiner, N.; Moc, P. A Review on Polymer Electrolyte Membrane Fuel Cell Catalyst Degradation and Starvation Issues : Causes , Consequences and Diagnostic for Mitigation. **2009**, *194*, 130–145. <https://doi.org/10.1016/j.jpowsour.2009.03.060>.
- (9) Tang, H.; Geng, K.; Aili, D.; Ju, Q.; Pan, J.; Chao, G.; Yin, X.; Guo, X.; Li, Q.; Li, N. Low Pt Loading for High-Performance Fuel Cell Electrodes Enabled by Hydrogen-Bonding Microporous Polymer Binders. *Nat Commun* **2022**, *13* (1). <https://doi.org/10.1038/s41467-022-34489-x>.
- (10) Wu, J.; Zi, X.; Martin, J. J.; Wang, H.; Zhang, J.; Shen, J.; Wu, S.; Merida, W. A Review of PEM Fuel Cell Durability : Degradation Mechanisms and Mitigation Strategies. **2008**, *184*, 104–119. <https://doi.org/10.1016/j.jpowsour.2008.06.006>.
- (11) Yu, Y.; Li, H.; Wang, H.; Yuan, X.; Wang, G.; Pan, M. A Review on Performance Degradation of Proton Exchange Membrane Fuel Cells during Startup and Shutdown Processes : Causes , Consequences , and Mitigation Strategies. *J Power Sources* **2012**, *205* (1), 10–23. <https://doi.org/10.1016/j.jpowsour.2012.01.059>.
- (12) Yu, Y.; Tu, Z.; Zhang, H.; Zhan, Z.; Pan, M. Comparison of Degradation Behaviors for Open-Ended and Closed Proton Exchange Membrane Fuel Cells during Startup and Shutdown Cycles. *J Power Sources* **2011**, *196* (1), 5077–5083. <https://doi.org/10.1016/j.jpowsour.2011.01.075>.

- (13) Lopes, P. P.; Tripkovic, D.; Martins, P. F. B. D. B. D.; Strmcnik, D.; Ticianelli, E. A.; Stamenkovic, V. R.; Markovic, N. M. Dynamics of Electrochemical Pt Dissolution at Atomic and Molecular Levels. *Journal of Electroanalytical Chemistry* **2017**, 819 (September), 0–1. <https://doi.org/10.1016/j.jelechem.2017.09.047>.
- (14) Cherevko, S.; Zeradjanin, A. R.; Keeley, G. P.; Mayrhofer, K. J. J. A Comparative Study on Gold and Platinum Dissolution in Acidic and Alkaline Media. *J Electrochem Soc* **2014**, 161 (12), H822–H830. <https://doi.org/10.1149/2.0881412jes>.
- (15) Goeke, R. S.; Datye, A. K.; Atanassov, P.; St-Pierre, J. Model Electrode Structures for Studies of Electrocatalyst Degradation. *ECS Trans* **2010**, 33 (1), 361–368. <https://doi.org/10.1149/1.3484534>.
- (16) MOSELEY, P. T. International Workshop on Degradation Issues in Fuel Cells. *J Power Sources* **2008**, 182 (2), 389–475.
- (17) Merte, L. R.; Behafarid, F.; Miller, D. J.; Friebe, D.; Cho, S.; Mbuga, F.; Sokaras, D.; Alonso-mori, R.; Weng, T. C.; Nordlund, D.; Nilsson, A.; Cuenya, B. R.; Roldan Cuenya, B. Electrochemical Oxidation of Size-Selected Pt Nanoparticles Studied Using in Situ High-Energy-Resolution X - Ray Absorption Spectroscopy. *ACS Catal* **2012**, 2 (11), 2371–2376. <https://doi.org/10.1021/cs300494f>.
- (18) Ettingshausen, F.; Kleemann, J.; Marcu, A.; Toth, G.; Fuess, H.; Roth, C. Dissolution and Migration of Platinum in PEMFCs Investigated for Start/Stop Cycling and High Potential Degradation. *Fuel Cells* **2011**, 11 (2), 238–245. <https://doi.org/10.1002/fuce.201000051>.
- (19) Borup, R. L.; Davey, J. R.; Garzon, F. H.; Wood, D. L.; Inbody, M. A. PEM Fuel Cell Electrocatalyst Durability Measurements. *J Power Sources* **2006**, 163 (1 SPEC. ISS.), 76–81. <https://doi.org/10.1016/j.jpowsour.2006.03.009>.
- (20) Guilminot, E.; Corcella, A.; Charlot, F.; Maillard, F.; Chatenet, M. Detection of Pt[Sup Z+] Ions and Pt Nanoparticles Inside the Membrane of a Used PEMFC. *J Electrochem Soc* **2007**, 154 (1), B96. <https://doi.org/10.1149/1.2388863>.
- (21) Ahluwalia, R. K.; Arisetty, S.; Peng, J.-K.; Subbaraman, R.; Wang, X.; Kariuki, N.; Myers, D. J.; Mukundan, R.; Borup, R.; Polevaya, O. Dynamics of Particle Growth and Electrochemical Surface Area Loss Due to Platinum Dissolution. *J Electrochem Soc* **2014**, 161 (3), F291–F304. <https://doi.org/10.1149/2.051403jes>.
- (22) Mitsushima, S.; Kawahara, S.; Ota, K.; Kamiya, N. Consumption Rate of Pt under Potential Cycling. *J Electrochem Soc* **2007**, 154 (2), B153. <https://doi.org/10.1149/1.2400596>.
- (23) Topalov, A. A.; Cherevko, S.; Zeradjanin, A. R.; Meier, J. C.; Katsounaros, I.; Mayrhofer, K. J. J. Towards a Comprehensive Understanding of Platinum Dissolution in Acidic Media. *Chem Sci* **2014**, 5 (2), 631–638. <https://doi.org/10.1039/c3sc52411f>.
- (24) Topalov, A. A.; Katsounaros, I.; Auinger, M.; Cherevko, S.; Meier, J. C.; Klemm, S. O.; Mayrhofer, K. J. J. Dissolution of Platinum: Limits for the Deployment of Electrochemical Energy Conversion? *Angewandte Chemie - International Edition* **2012**, 51 (50), 12613–12615. <https://doi.org/10.1002/anie.201207256>.
- (25) Cherevko, S.; Keeley, G. P.; Geiger, S.; Zeradjanin, A. R.; Hodnik, N.; Kulyk, N.; Mayrhofer, K. J. J. Dissolution of Platinum in the Operational Range of Fuel Cells. *ChemElectroChem* **2015**, 2 (10), 1471–1478. <https://doi.org/10.1002/celc.201500098>.

- (26) Ferreira-aparicio, P.; Chaparro, A. M.; Folgado, M. A.; Conde, J. J.; Brightman, E.; Hinds, G.; Antonia, M.; Conde, J. J.; Brightman, E.; Hinds, G. Degradation Study by Start-Up/Shut-Down Cycling of Superhydrophobic Electrosprayed Catalyst Layers Using a Localized Reference Electrode Technique. *ACS Appl Mater Interfaces* **2017**, 9 (1), 10626–10636. <https://doi.org/10.1021/acsami.6b15581>.
- (27) Jo, Yooyeon; Cho, Eunae; Kim, J. A Study on Performance Degradation of PEMFC by Repetitive Startup_Shutdown Cycling. *Transacitons of the Korean Hydrogen and New Energy Society* **2009**, 20 (8), 318–322.
- (28) Babu, S. K.; Spornjak, D.; Dillet, J.; Lamibrac, A.; Maranzana, G.; Didierjean, S.; Lottin, O.; Borup, R. L.; Mukundan, R. Spatially Resolved Degradation during Startup and Shutdown in Polymer Electrolyte Membrane Fuel Cell Operation. *Appl Energy* **2019**, 254 (August), 113659. <https://doi.org/10.1016/j.apenergy.2019.113659>.
- (29) Joo, S.; Kim, S.; In, J.; Woong, C.; Lee, J.; Song, I.; Lee, N.; Kim, K.; Park, J. Lifetime Prediction of a Polymer Electrolyte Membrane Fuel Cell via an Accelerated Startup e Shutdown Cycle Test. *Int J Hydrogen Energy* **2012**, 37 (12), 9775–9781. <https://doi.org/10.1016/j.ijhydene.2012.03.104>.
- (30) Æ, P. P.; Chang, Q.; Tang, T. A Quick Evaluating Method for Automotive Fuel Cell Lifetime. *Int J Hydrogen Energy* **2008**, 33 (1), 3829–3836. <https://doi.org/10.1016/j.ijhydene.2008.04.048>.
- (31) Bruijn, F. A. De; Dam, V. A. T.; Janssen, G. J. M. Review : Durability and Degradation Issues of PEM Fuel Cell Components. *Fuel Cells* **2008**, 8 (1), 3–22. <https://doi.org/10.1002/fuce.200700053>.
- (32) Zhang, T.; Wang, P.; Chen, H.; Pei, P. A Review of Automotive Proton Exchange Membrane Fuel Cell Degradation under Start-Stop Operating Condition. *Appl Energy* **2018**, 223 (January), 249–262. <https://doi.org/10.1016/j.apenergy.2018.04.049>.
- (33) Myers, D. J.; Wang, X.; Smith, M. C.; More, K. L. Potentiostatic and Potential Cycling Dissolution of Polycrystalline Platinum and Platinum Nano-Particle Fuel Cell Catalysts. *J Electrochem Soc* **2018**, 165 (6), F3178–F3190. <https://doi.org/10.1149/2.0211806jes>.
- (34) Mitsushima, S.; Koizumi, Y.; Uzuka, S.; Ota, K. I. Dissolution of Platinum in Acidic Media. *Electrochim Acta* **2008**, 54 (2), 455–460. <https://doi.org/10.1016/j.electacta.2008.07.052>.
- (35) Shao-Horn, Y.; Sheng, W. C.; Chen, S.; Ferreira, P. J.; Holby, E. F.; Morgan, D. Instability of Supported Platinum Nanoparticles in Low-Temperature Fuel Cells. *Top Catal* **2007**, 46 (3–4), 285–305. <https://doi.org/10.1007/s11244-007-9000-0>.
- (36) Marković, N. M.; Gasteiger, H. A.; Ross, P. N.; Division, M. S. Oxygen Reduction on Platinum Low Index Single Crystal Surfaces in Sulfuric Acid Solution. **1995**, 99 (11), 3411–3415.
- (37) Brazovski, S. A.; Rice, M. J.; Mele, E. J.; Jackiw, R.; Semenov, G.; Goldstone, J.; Wilczek, F.; Kivelson, S.; Ortega, J.; Flores, F.; Yeom, H. W.; Thouless, D. J.; Niu, Q.; Thouless, D. J.; Hughes, T. L.; Peierls, R. F.; Marzari, N.; Mostofi, A. A.; Yates, J. R.; Souza, I.; Vanderbilt, D.; Xiao, D.; Niu, Q. Identification of Active Sites in CO Oxidation and Water-Gas Shift over Supported Pt Catalysts. **2015**, 350 (6257), 185–189.
- (38) Bunch, J. S.; Van Der Zande, A. M.; Verbridge, S. S.; Frank, I. W.; Tanenbaum, D. M.; Parpia, J. M.; Craighead, H. G.; McEuen, P. L. Improved Oxygen Reduction Activity on Pt₃Ni(111) via Increased Surface Site Availability. *Science (1979)* **2007**, 315 (5811), 490–493. <https://doi.org/10.1126/science.1136836>.

- (39) Cui, C.; Gan, L.; Heggen, M.; Rudi, S.; Strasser, P. Compositional Segregation in Shaped Pt Alloy Nanoparticles and Their Structural Behaviour during Electrocatalysis. *Nat Mater* **2013**, *12* (8), 765–771. <https://doi.org/10.1038/nmat3668>.
- (40) Colón-Mercado, H. R.; Popov, B. N. Stability of Platinum Based Alloy Cathode Catalysts in PEM Fuel Cells. *J Power Sources* **2006**, *155* (2), 253–263. <https://doi.org/10.1016/j.jpowsour.2005.05.011>.
- (41) Steinhardt, R. G.; Serfass, E. J. X-Ray Photoelectron Spectrometer for Chemical Analysis. *Anal Chem* **1951**, *23* (11), 1585–1590. <https://doi.org/10.1021/ac60059a019>.
- (42) Siegbahn, K. Electron Spectroscopy for Atoms, Molecules and Condensed Matter - an Overview. *J Electron Spectros Relat Phenomena* **1985**, *36* (2), 113–129. [https://doi.org/10.1016/0368-2048\(85\)80013-X](https://doi.org/10.1016/0368-2048(85)80013-X).
- (43) J., C. *Handbook of X-Ray Photoelectron Spectroscopy*; 1992.
- (44) Susi, T.; Pichler, T.; Ayala, P. X-Ray Photoelectron Spectroscopy of Graphitic Carbon Nanomaterials Doped with Heteroatoms. *Beilstein Journal of Nanotechnology* **2015**, *6* (1), 177–192. <https://doi.org/10.3762/bjnano.6.17>.
- (45) Stevie, F. A.; Donley, C. L. Introduction to X-Ray Photoelectron Spectroscopy. *Journal of Vacuum Science & Technology A: Vacuum, Surfaces, and Films* **2020**, *38* (6). <https://doi.org/10.1116/6.0000412>.
- (46) Seyama, H.; Soma, M.; Theng, B. K. G. *X-Ray Photoelectron Spectroscopy*, 1st ed.; Elsevier Inc., 2013; Vol. 5. <https://doi.org/10.1016/B978-0-08-098259-5.00007-X>.
- (47) Smith, J. W.; Saykally, R. J. Soft X-Ray Absorption Spectroscopy of Liquids and Solutions. *Chem Rev* **2017**, *117* (23), 13909–13934. <https://doi.org/10.1021/acs.chemrev.7b00213>.

Chapter 2

A laboratory-based electrochemical NAP-XPS system for operando electrocatalysis studies

Abstract

During electrocatalytic reactions, the electrode, adsorbates, electrolyte ions, and solvent molecules at the electrode-electrolyte interface each play an important role. Electrochemical X-ray photoelectron spectroscopy (XPS) holds great promise for deciphering these roles, providing the oxidation state or bonding environment of every element present at the interface. However, combining the vacuum required for XPS with the wet environment needed for electrochemistry constitutes a technical challenge, requiring purpose-built instrumentation and spectro-electrochemical cell design. Here, we present a laboratory-based electrochemical XPS instrument optimized for *operando* studies on nano-structured electrocatalysts. We show that using a spectro-electrochemical cell design based on a membrane-catalyst-graphene assembly, the system is able to probe the electrode surface, interfacial water, and interfacial ions under well-defined potential control. Importantly, the system facilitates the transport of any molecule or ion towards the working electrode, facilitating measurements under a wide variety of electrocatalytic conditions. This is exemplified for the oxygen reduction reaction.

This Chapter has been published in Vacuum:

Javed, H.; Kolmeijer, K.; Klein, N.; Trindell, J. A.; Schneider, G.; Mom, R. V. A Laboratory-Based Electrochemical NAP-XPS System for Operando Electrocatalysis Studies. *Vacuum* 2025, 231 (PA), 113755. <https://doi.org/10.1016/j.vacuum.2024.113755>.

Chapter 2 : A laboratory-based electrochemical NAP-XPS system for *operando* electrocatalysis studies

2.1 Introduction

An atomic-level understanding of the relationship between the applied potential and the electrode-electrolyte interface structure is crucial for advancing electrochemical systems, including batteries, electrolyzers, and fuel cells^{1–4}. X-ray photoelectron spectroscopy (XPS) is among the most powerful characterization techniques for achieving this understanding^{5–14}, offering insights into oxidation states, bonding environments, and the local electrostatic potential¹⁵ (in e.g. the double layer). However, the vacuum required for XPS measurements makes in situ measurements under electrochemical conditions non-trivial. To interface the wet environment needed for electrochemistry with the vacuum required for XPS, several experimental arrangements have been developed, such as the dip-and-pull method^{16–18}, polymer electrolyte membrane approach^{19,20} and graphene window-based approaches^{21–23}. This has made it possible to study several important electrochemical systems, such as the oxygen evolution reaction^{24–26} and the CO₂ reduction reaction^{27,28}.

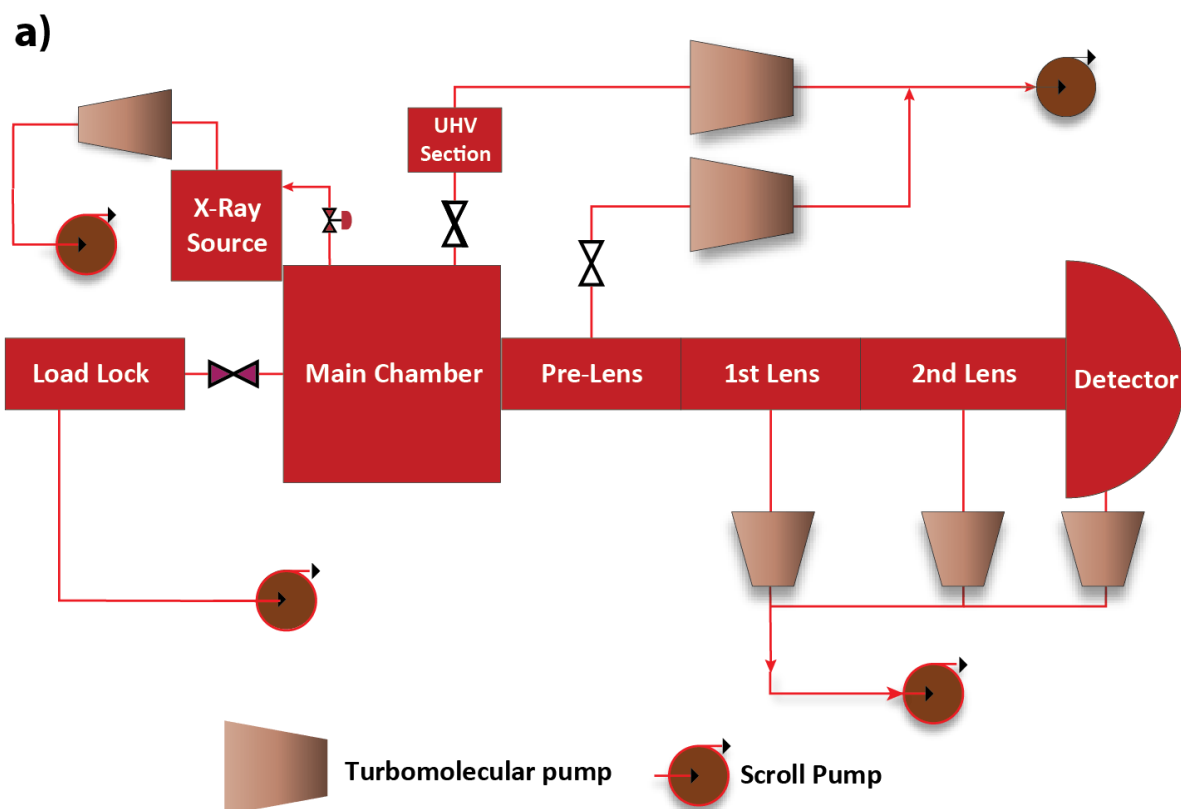
While these applications highlight the potential of electrochemical XPS, the current reliance on synchrotron facilities limits access to the technique. Wider use could be achieved through the development of laboratory-based electrochemical XPS. First efforts in this direction have emerged^{29–33}, making use of the lab-based near-ambient-pressure XPS (NAP-XPS) instrumentation that has recently become available. For example, Liu et al. employed a Cr source to perform dip-and-pull type measurements using tender X-rays²⁹, in direct analogy to the dip-and-pull set-ups available at synchrotrons. A different approach was used by Haug et al.³³, who used an Al soft X-ray source in combination with a tilted thin film cell. Both approaches rely on the formation of a 10–30 nm electrolyte film on the electrode, which is thick enough for a realistic electrode-electrolyte interface structure to form, but thin enough for photoelectrons to traverse in order to reach the electron analyzer. Due to the limited mass transport through the ultrathin electrolyte film, this strategy is primarily suited for the study of the electrode-electrolyte interface under non-faradaic conditions, i.e. when little electrochemical current passes²⁰.

To extend the applicability of laboratory electrochemical XPS to electrocatalytic systems with significant electrochemical current, we present a system based on a membrane-electrode-assembly type cell, analogous to fuel cells and electrolyzers. This approach builds on the membrane cells developed in the Gericke group at the BESSY II synchrotron, which have proven successful for the study of e.g. oxygen evolution electrocatalysis^{21,34–39} at significant current density. Here, we introduce the use of a porous polycarbonate membrane in the MEA, which facilitates the transport of any molecular or ionic reactant to the working electrode, enabling in situ studies on a wide variety of electrocatalytic reactions. We demonstrate the capabilities of the instrument using the oxidation of Pt, adsorption of SO₄²⁻, and the oxygen reduction reaction.

Chapter 2 : A laboratory-based electrochemical NAP-XPS system for *operando* electrocatalysis studies

2.2 System design

The electrochemical XPS setup exhibits a modular arrangement (as shown in Figure 2.1), consisting of 1) a load-lock with a manipulator that holds the electrochemical cell, 2) the main chamber, to which the 3) X-ray source, 4) ultra-high-vacuum (UHV) pumping section and 5) the electron analyzer are attached. In addition, electrolyte/gas supply and safety interlock systems support the operation of the set-up. Most components in the system are standard commercial components. However, the load lock, main chamber, and the support systems have been designed in-house specifically for electrochemical experiments. In the coming sections, we will focus on the design of the most crucial part of the set-up, the cell design. A detailed description of other components of the system is provided in the supporting information (supplementary information A2.1-2.6).



Chapter 2 : A laboratory-based electrochemical NAP-XPS system for *operando* electrocatalysis studies

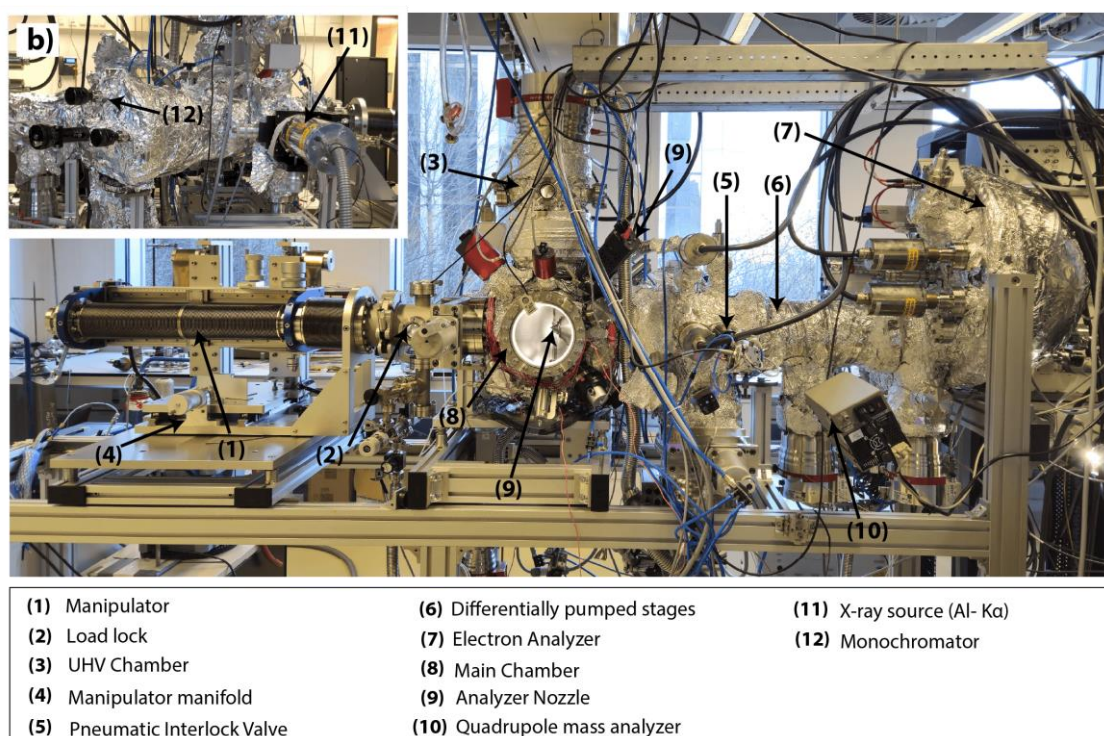


Figure 2.1 : Overview of the EC-NAP-XPS. a) Schematic diagram showing the layout of the system and b) Labelled system photograph displaying a detailed view of the NAP-XPS setup

i) In situ spectro-electrochemical (EC-XPS) cell extension

The electrochemical extension contains the electrochemical cell, electrolyte and electrical connections, and safety valves (Figure 2.2 and Figure 2.3). The extension contains a fixed and an interchangeable part. The fixed part is inserted into the tube of the manipulator (see supplementary information A2.1), separating it from the vacuum and contains the electrolyte lines along with the electrical connections that remain mounted on the inner manipulator tube. The interchangeable part comprises of the electrochemical cell that can be removed from the manipulator, facilitating easy sample/cell exchange.

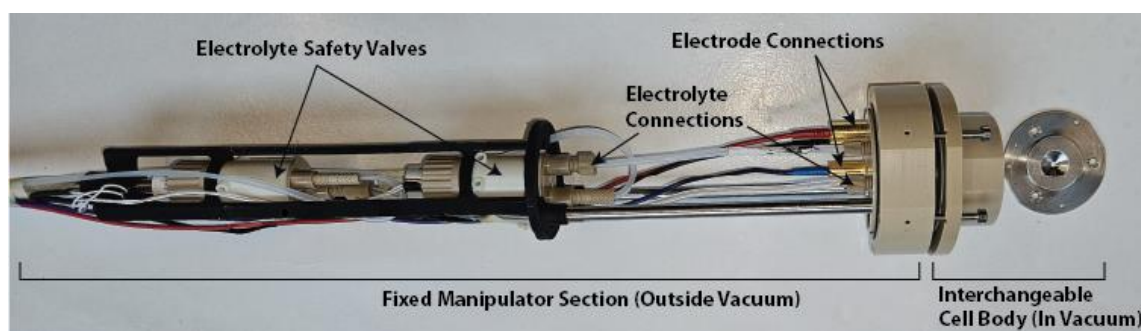


Figure 2.2 : Electrochemical manipulator construction

Chapter 2 : A laboratory-based electrochemical NAP-XPS system for *operando* electrocatalysis studies

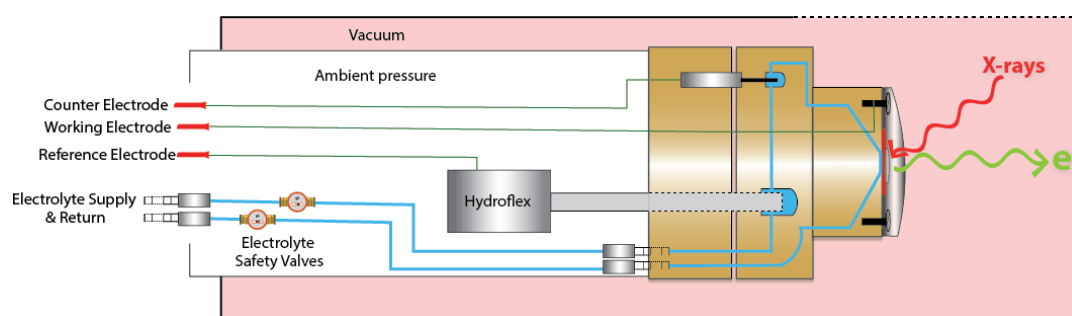


Figure 2.3 : Schematic diagram of the electrochemical manipulator

Figure 2.4 (A, B and C) show the detailed component view of the exchangeable part, i.e. the electrochemical cell. In Figure 2.4 A, the cell body (1) is made from PEEK using 3D printing (Bond3D Production BV), with channels for electrolyte flow (2) as well as connections for reference and counter electrodes built into the cell body.

The reference electrode (3) is a standard hydroflex (Gaskatel) which is screwed in via a brass coupling into a dedicated cavity in the cell body. The design choice of having the reference electrode horizontally at the back of the cell outside the vacuum (Figure 2.3) allows us to use the larger version of the hydroflex, which is more stable over the long run. The counter electrode (4) is a platinum rod attached to the cell body by a PEEK coupling and extends into the electrolyte channel. This Pt rod can be disassembled from its coupling to be cleaned and annealed separately. Figure 2.4 B shows the top view of the cell; a membrane electrode assembly (working electrode) is mounted underneath the titanium contact plate (6) which is in contact with a brass coupling (5) screwed through the PEEK body of the cell, establishing an electrical connection to the working electrode. The top plate contains a 2 mm opening, which is the measurement area for XPS (7). Electrical connection between the cell's electrodes and the fixed manipulator section is established via spring contacts, minimizing the amount of screws involved in cell mounting.

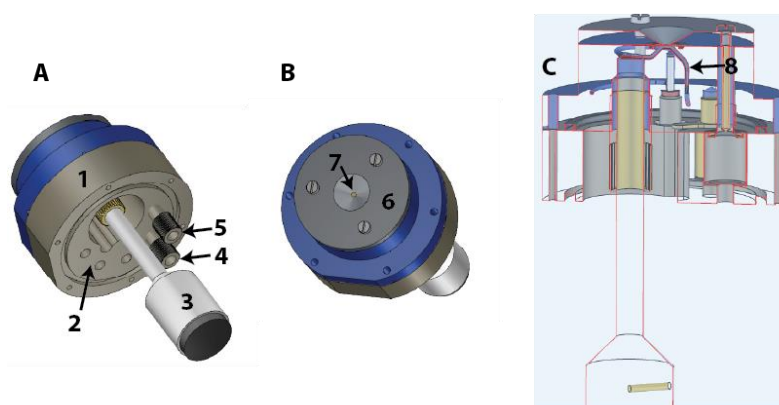


Figure 2.4 : Spectro electrochemical Cell Design for NAP-XPS; A. Side view of the PEEK body of the cell (1), connections for electrolyte (2), the Hydroflex RHE (3), connections for working and Pt counter electrodes (4,5). B. Top view, with the titanium top plate (6) , XPS measurement area (7) and C. Cross-section showing the 3D printed electrolyte channels (8) inside the cell body

Chapter 2 : A laboratory-based electrochemical NAP-XPS system for *operando* electrocatalysis studies

PEEK is chosen here because of its high chemical inertness⁴⁰. Meanwhile, 3D printing has the key advantage that connections and electrolyte lines can be shaped in any form with very little restrictions from the manufacturing method. The cell has several other salient features: i) It offers a compact design where all the electrolyte connections, the electrical connections and the reference electrode can be conveniently situated at the backside of the cell outside the vacuum, ii) the cell can be built as one piece with a minimal amount of connections, and iii) the cell has a very small internal volume which facilitates quick switching to a different electrolyte and limits the amount of electrolyte that can spill into the vacuum chamber in event of a leakage

The potentiostat connections for the electrodes as well as the electrolyte supply and return lines are connected to the fixed part of the manipulator. The electrolyte connections (2) are present at the rear of the cell and are connected to the electrolyte supply and return lines that run through the inner tube of the manipulator. As a safety precaution, individual SOVs (Solenoid Operated Valves) are installed on each electrolyte line, immediately cutting off the electrolyte supply upon detecting an electrolyte leak from the cell into the main chamber. These, in addition to other safety interlocks, are discussed in the supplementary information A2.5.

All the surfaces of the electrochemical manipulator that come in contact with the electrolyte can be cleaned to according to regular electrochemical lab standards using acidified KMnO_4 , dilute piranha solution ($\text{H}_2\text{SO}_4 + \text{H}_2\text{O}_2$) and warm water. We note that such cleaning is crucial to ensure well-controlled electrochemistry inside the cell and reliable Spectro-electrochemical results. Detailed cleaning process is explained in the supplementary information A2.7.

ii) Membrane electrode assembly (MEA)

The samples used in the electrochemical cell are a special type of membrane electrode assembly based on the design developed at ISIS Beamline at BESSY-II^{21,41}. In short, the electrocatalyst of choice is deposited on membrane, which can either be porous or a polymer electrolyte (Figure 2.5). Subsequently, the catalyst is covered with a bilayer of graphene. During the electrochemical XPS measurements, the membrane-catalyst-graphene assembly is in contact with electrolyte from the backside of the membrane. This electrolyte can permeate through the membrane in order to reach the catalyst, providing electrochemical contact. Meanwhile, the graphene functions as an evaporation barrier, so that a liquid film is maintained around the catalyst particles. In previous work⁴¹, our assembly was based on polymer ion-exchange membranes (e.g Nafion), which only allow water molecules and protons to pass through to the working electrode. Here, we make use of a porous polycarbonate (PC) membrane (50 nm pore size Polycarbonate PVP treated Membrane, it4ip SA), which allows any molecule or ion to reach the electrocatalyst. This makes it possible to study a much wider array of electrochemical reactions, as will be exemplified below for the oxygen reduction reaction. Importantly, the porous PC membrane is chemically stable against both low and high pH.

Chapter 2 : A laboratory-based electrochemical NAP-XPS system for *operando* electrocatalysis studies

Figure 2.6 shows scanning electron microscope images of the MEAs in ‘as prepared’ state and after an XPS experiment. The as prepared sample (Figure 2.6 A) shows an evenly distributed thin catalyst layer mixed with the 50 nm pores that are visible as black. Images following 6-8 hours of voltametric measurements and XPS measurements (Figure 2.6 B) show essentially the same configuration, but with a more pronounced cracking pattern due to physical strain on the MEA once it is pressed under the top plate of the electrochemical cell and potentially slight catalyst degradation. Note that in both cases, the graphene cannot be discerned due to the high magnification and uniformity of the graphene layer in the region imaged. However, the SEM images collected at lower magnifications and in different regions on the graphene-Pt-membrane assembly clearly shown the presence of the graphene layer (additional images in supplementary information A2.9). Additionally, a strong aromatic C 1s peak from the graphene can be seen in the survey spectrum (Figure 2.11). Corresponding cyclic voltammograms to these SEM images show characteristic Pt peaks in both the cases, although the latter having smaller peak currents which may be attributed to Pt catalyst degradation mechanisms such as dissolution and Ostwald ripening^{42–47}. Importantly, these measurements show that prolonged electrochemical contact can be maintained even under circumstances where electrode degradation occurs.

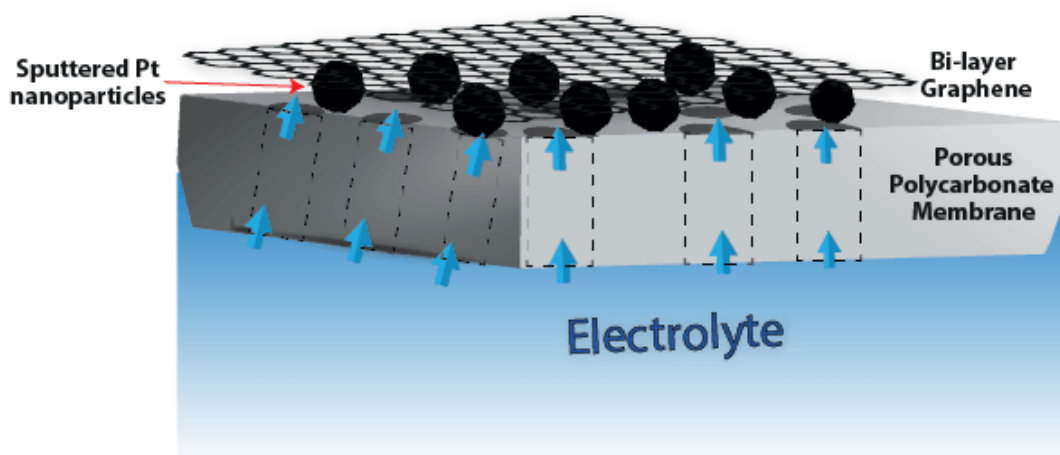


Figure 2.5 : Schematic diagram of Graphene-Platinum-Polycarbonate membrane assembly

Chapter 2 : A laboratory-based electrochemical NAP-XPS system for *operando* electrocatalysis studies

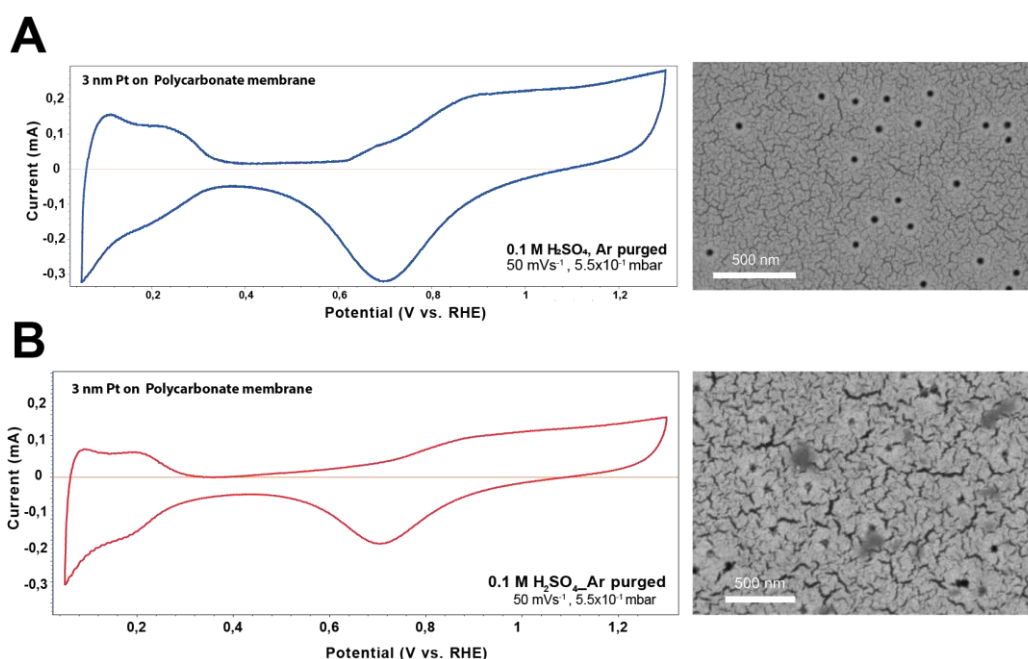


Figure 2.6 : SEM Images recorded for Graphene-Platinum-Membrane Assembly as prepared (A) and following 6-8 hours of spectro-electrochemical measurements in dilute acidic media (B) shown with their corresponding cyclic voltammograms

To test the mass transport through the porous membrane, we conducted oxygen reduction electrocatalysis experiments. Note that this is an extreme test, because the reactant O₂ can only be dissolved in the electrolyte in extremely low concentrations. Nonetheless, Figure 2.7 shows a clear response to the presence/absence of O₂ in the electrolyte, confirming that O₂ is readily transported through the porous membrane to the electrode under in situ XPS conditions. However, it should be noted that the response is small indicating that some mass transport limitations do exist, as can be expected based on sample geometry observed in Figure 2.5. Nonetheless, the oxygen permeation experiment highlights the possibility of studying a wide variety of electrochemical reactions in the NAP-XPS set-up, including those with neutral molecules or dissolved gases.

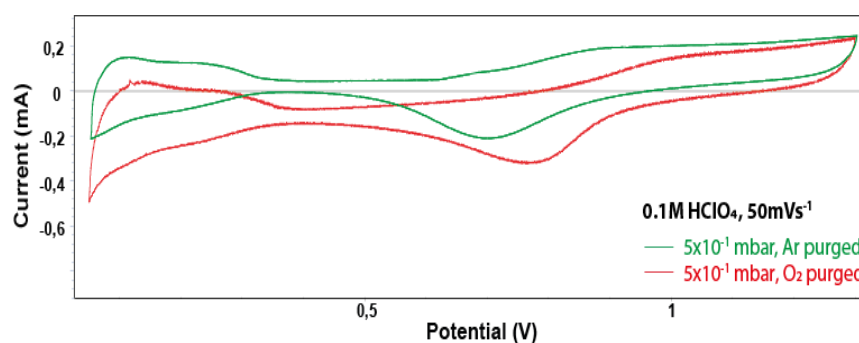


Figure 2.7 : Oxygen permeation behavior of the 50 nm pore size Polycarbonate membrane evidenced by the voltametric response of Pt, showing effect of equilibrium oxygen concentration under ambient and rough vacuum pressures

Chapter 2 : A laboratory-based electrochemical NAP-XPS system for *operando* electrocatalysis studies

2.3 Experimental methods

To conduct proof-of-concept measurements, 3 nm Pt was sputtered onto a porous polycarbonate membrane (50 nm pore size Polycarbonate PVP treated Membrane, it4ip SA) using a Cressington sputter coater. In-house prepared graphene was transferred onto membrane-catalyst assembly according to previously established procedure²¹ and stored dry. Prior to use in an in situ experiment, the sample is immersed in ultrapure water for ~15 minutes to hydrate the pores. The membrane-catalyst-graphene assembly is mounted on the cell with the graphene is centered on the XPS measurement area, facing the vacuum side (Figure 2.8). The electrochemistry is controlled using a SP-200 Biologic potentiostat. This allows us to perform all the standard electrochemical techniques within the *operando* spectroscopic experiment, ranging from performing simple cyclic voltammograms, pulse voltammograms, linear sweep voltammograms to more complex experiments involving a series of these techniques one after the other during the XPS operation.

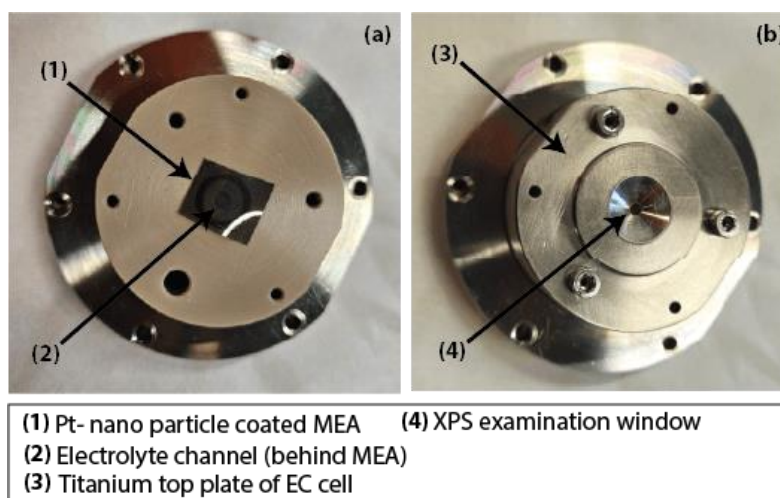


Figure 2.8 : Membrane electrode assembly mounting on the EC cell; (a) Graphene-Platinum-Membrane assembly has to be centered on the electrolyte channel (b) Titanium top plate is mounted as an electrical contact to the membrane

Once electrolyte circulation is established, the sample is placed inside the load lock and pumped to rough vacuum while checking for visible leaks. Proper electrochemistry under vacuum conditions is verified using the (stable) open circuit potential and cyclic voltammetry. After placing the sample in the cell and establishing the electrolyte circulation at a steady state, a cyclic voltammogram was measured between $0.05 V_{\text{RHE}} - 1.3 V_{\text{RHE}}$ at 50 mVs^{-1} to remove any memory effects and to know the electrochemically active surface area of the deposited Pt nano-particles. The cell position is optimized with respect to the X-ray source and the analyzer nozzle using a high-resolution camera and the XPS count rate (see Figure 2.9).

Chapter 2 : A laboratory-based electrochemical NAP-XPS system for *operando* electrocatalysis studies

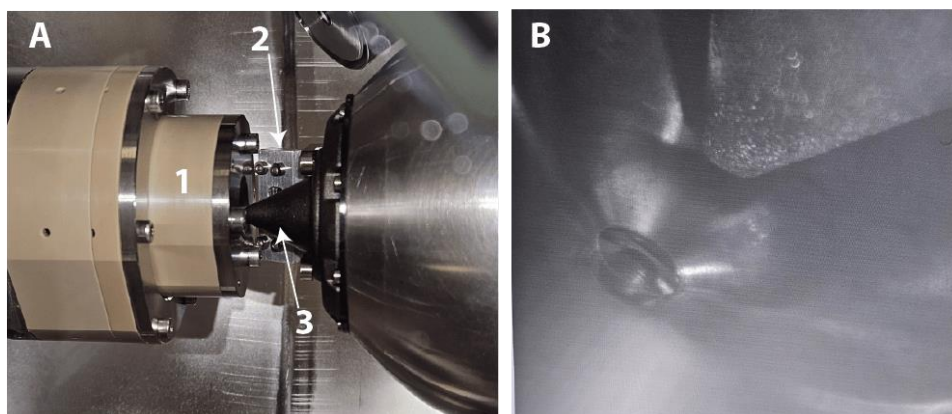


Figure 2.9 : Electrochemical cell alignment; A) shows the EC-XPS cell (1) aligned with the X-ray source NAP extension (2) and the analyzer nozzle (3) and B) shows fine tuning of the sample distance with the analyzer nozzle

2.4 Results

i) Pt Oxidation in Acidic Media

In this section, we demonstrate that the lab-based electrochemical NAP-XPS that we have commissioned is capable of conducting in situ studies on Pt oxidation using a lab-scale X-ray source. The precise nature of Pt oxidation is an important topic in electrocatalysis due to e.g. its implications on fuel cell stability^{48,49}. In previous work, we have studied Pt oxidation using synchrotron facilities^{21,35,41}, allowing for a direct comparison.

As a first step, we benchmarked the electrochemical behavior of the membrane-Pt-graphene assembly by comparison to graphite-supported Pt nanoparticles in a conventional glass cell. Figure 2.10 shows the cyclic voltammograms for the glass cell and the Spectro-electrochemical cell side by side. Clearly, very similar behavior is observed, confirming the proper electrochemical performance of the in situ spectroscopy cell. The small differences that can be observed are likely related to the difference in support effect between the glassy carbon electrode and the polycarbonate membrane.

Chapter 2 : A laboratory-based electrochemical NAP-XPS system for *operando* electrocatalysis studies

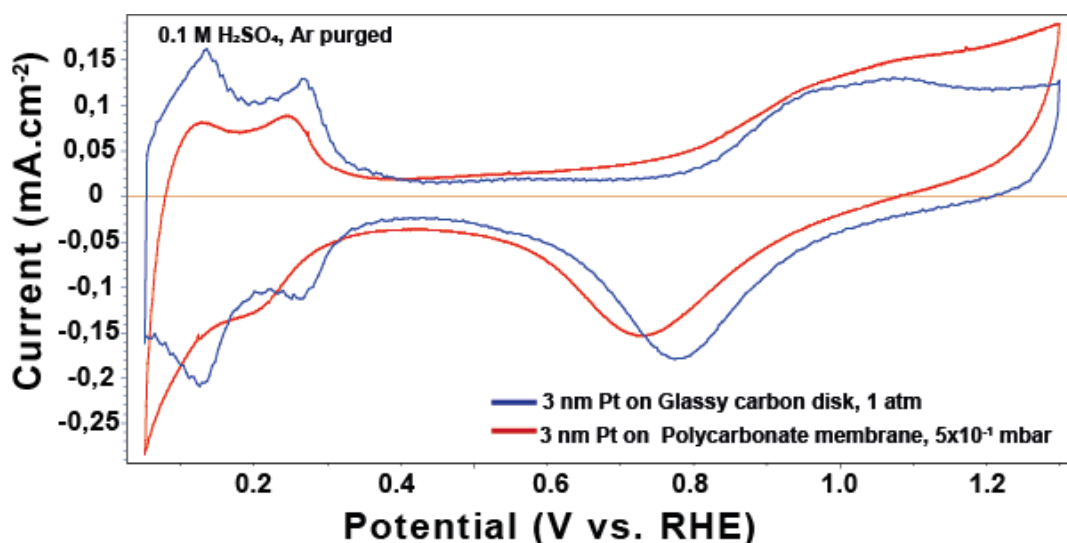


Figure 2.10 : Cyclic Voltammograms on 3 nm Pt nano-particles in glass cell (blue curve) using a glassy carbon support and (red curve) in EC-XPS flow cell using PC membrane support

The low leak rate of the cell and membrane-catalyst-graphene assembly is verified using the chamber pressure: $\sim 1 \times 10^{-1}$ mbar only being pumped through the 300 μm analyzer nozzle. This leak rate is achieved for both high and low pH electrolyte and any electrode potential. An advantage of the low chamber pressure is that there is minimal signal loss due to photoelectron-gas scattering.

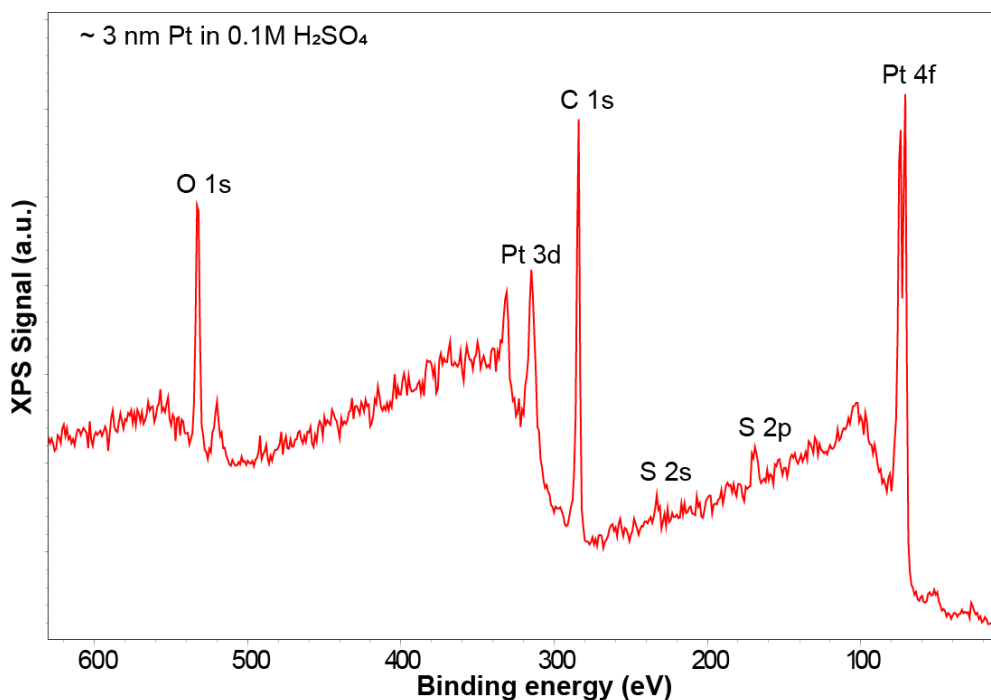


Figure 2.11 : XPS Survey spectrum for the membrane electrode assembly in acidic electrolyte (0.1M H_2SO_4)

Chapter 2 : A laboratory-based electrochemical NAP-XPS system for *operando* electrocatalysis studies

A survey spectrum was recorded prior to the anodization (Figure 2.11) which shows the expected elemental contributions from the aqueous electrolyte (O 1s), the catalyst (Pt 4f) and the support (C 1s and O 1s). C 1s appears as one of the most intense peaks, which mainly arises from the bilayer graphene covering the MEA and partially from the polycarbonate membrane support, which also contributes partially to the O 1s signal. XPS spectra are measured by anodizing the sample in steps, while recording spectra at each step potential (Figure 2.12). Pt 4f spectra were recorded at 10 eV analyzer pass energy with an acquisition time of ~5 min. The Pt spectra were fitted using different oxidation states of Pt; Pt⁰ (Pt 4f_{7/2} at 71.0 eV), Pt^{δ+} (71.8 eV), Pt²⁺ (72–72.7 eV) and Pt⁴⁺ (73.7 eV) doublets (the details of the curve fitting parameters are given in supplementary information A2.8).

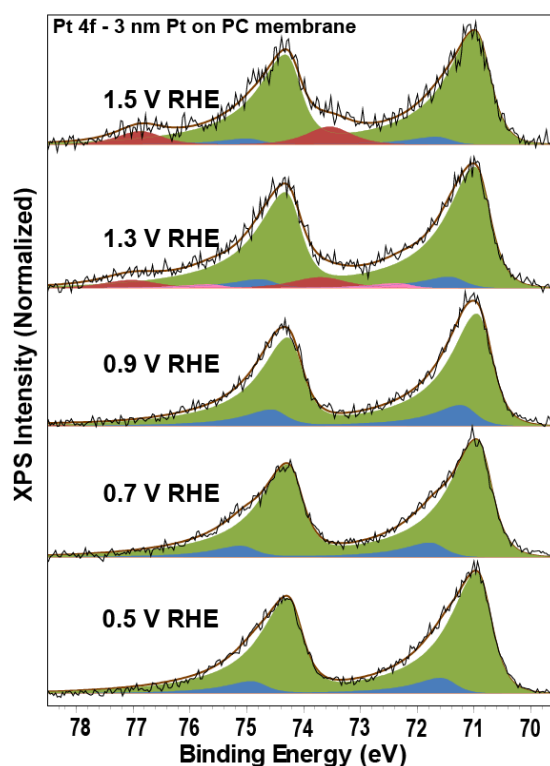


Figure 2.12 : Step-wise anodization of the Pt-nano particles in 0.1 M H₂SO₄, Pt 4f spectra are fit using Pt⁰ (green), Pt^{δ+} (blue), Pt²⁺ (pink), and Pt⁴⁺ (red) doublets.

At 0.5 V_{RHE}, the XPS spectra in Figure 2.12 show large contributions from metallic Pt and Pt^{δ+}. The Pt^{δ+} contribution at this low potential where no Pt oxides are expected, is related to the presence of adsorbates on the Pt surface, as also observed in our previous work^{35,41}. At 1.3 V_{RHE}, Pt is well within its oxidation regime and accordingly, prominent oxidized Pt contributions can be observed. In line with previous work, a mixture of Pt^{δ+}, Pt²⁺, and Pt⁴⁺ oxidation states is observed showing that an irregular surface oxide structure is formed. Upon increasing the potential further to 1.5 V_{RHE}, deeper oxidation of the nano-particles is induced which can be seen from a large contribution from Pt⁴⁺. It is important to note that based on modeling of the XPS signals, we previously estimated that the oxide film on the particles is approximately one monolayer thick⁴¹. This was done by modelling the oxide to metal ratios observed in Figure

Chapter 2 : A laboratory-based electrochemical NAP-XPS system for *operando* electrocatalysis studies

2.12 as a function of potential using planar and nanoparticle overlayer models^{50,51}. Thus the data presented here provide a clear showcase of the sensitivity that can be reached using lab-based electrochemical XPS.

A key feature of electrochemical XPS is that not only the chemistry of the electrode can be investigated, but also the behavior of the interfacial electrolyte. The binding energy shift with applied potential for the electrolyte species can be utilized to identify their location with respect to the working electrode^{20,35}. This binding energy shift originates from the change in the electrostatic potential experienced by the electrolyte when a potential is applied (see Figure 2.13). When the electrode is grounded, the shift for bulk electrolyte species (outside of the double layer) is described as:

$$E_{\text{binding,apparent}} = E_{\text{binding,actual}} + q_e \Delta U \quad (1)$$

Where $E_{\text{binding,apparent}}$ and $E_{\text{binding,actual}}$ show the observed and the real binding energies of the electrolyte species, q_e is the charge of an electron and ΔU is the change in the electrolyte potential with respect to the setup. Equation 1 indicates that bulk electrolyte species shift -1 eV when the electrode potential is increased by 1 V. In the double layer, the shift progressively reduces the closer the electrolyte species is to the electrode surface.

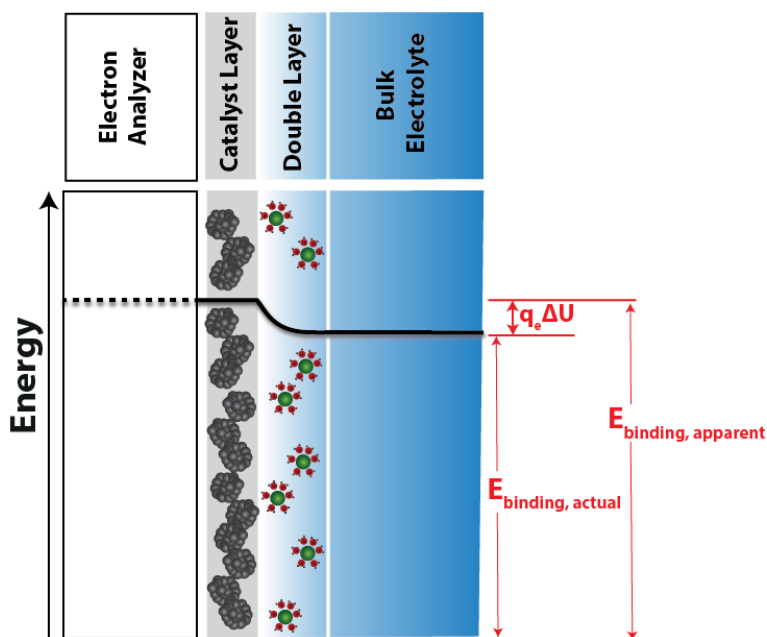


Figure 2.13: Difference between apparent and real binding energies as a result of change in the electrolyte potential. The product of electronic charge ' q_e ' and change in electrolyte potential ' ΔU ' equals the difference between apparent and real binding energies

The potential-dependent effect is clearly observed in O 1s spectra (Figure 2.14), which are dominated by water. Based on the ~ -1 eV/ V_{RHE} binding energy shift observed, it is clear that most of the probed water molecules are not located in the double layer. This is consistent with recent measurements on the double layer of the 0.1 M H_2SO_4 – RuO_2 interface, where it was

Chapter 2 : A laboratory-based electrochemical NAP-XPS system for *operando* electrocatalysis studies

shown that the double layer is $<1 \text{ nm}^{20}$, well below the probing depth of our XPS in liquid water⁵². The -1:1 shift for H_2O , but the lack of such a shift for the grounded Pt electrode establish that a proper electrode-electrolyte interface is formed in our cell.

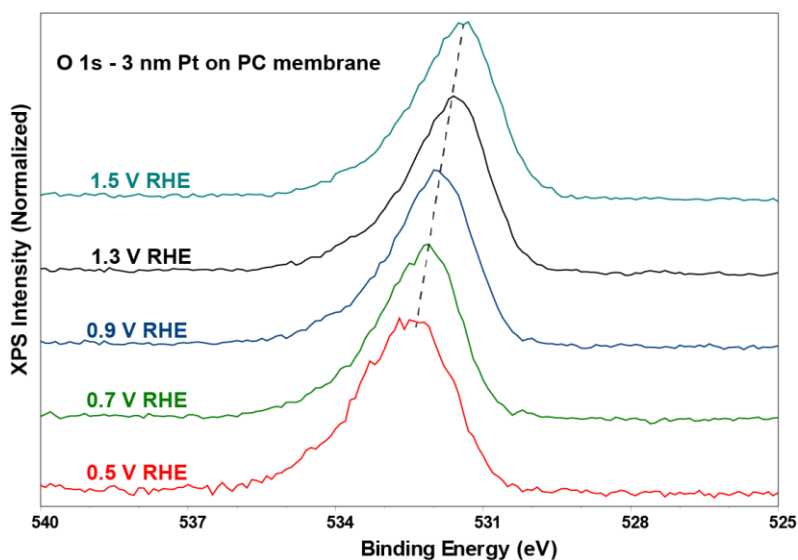


Figure 2.14 : Binding energy shift for O 1s spectra as a function of potential

Since the experiment was done in 0.1 M H_2SO_4 , it is also important to track the contribution of sulfur as a function of polarization (Figure 2.15). It can be clearly observed that the sulfate S 2p does not shift in the same way as the water O 1s peak. This can be explained by the fact that sulfate is known to adsorb on Pt electrodes (contributing to the $\text{Pt}^{\delta+}$ observed in the Pt 4f spectra). As a consequence, the sulfate ions are grounded to the working electrode and do not experience any electrostatic potential shift with increasing applied potential. As small S 2p shift can be observed for the spectra at 1.3 V_{RHE} and 1.5 V_{RHE} spectra, however. This shift is likely related to the different chemical environment experience by sulfate ions when adsorbed on metallic Pt ($<1.3 \text{ V}_{\text{RHE}}$) vs. on PtO_x (at or above 1.3 V_{RHE}).

Chapter 2 : A laboratory-based electrochemical NAP-XPS system for *operando* electrocatalysis studies

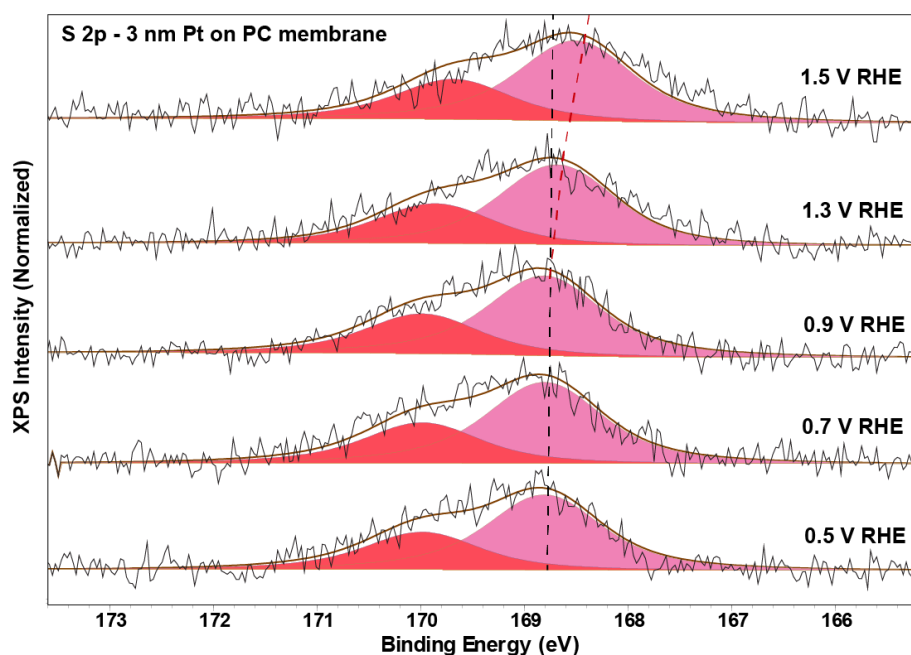


Figure 2.15 : Step-wise anodization of the Pt-nano particles in 0.1 M H_2SO_4 , S 2p spectra are fit using pink and red doublets. Black dashed line shows an absence of a spectral shift at lower potentials while deviating red dashed line shows a binding shift at higher potentials due to changing nature of chemical interaction between sulfate and Pt oxides

With the case study on Pt oxidation, we showcase how our laboratory-based electrochemical XPS system is able to resolve both sides of the electrode-electrolyte interface. Exploiting the chemical stability of the polycarbonate support and its non-selective electrolyte conduction to the working electrode, a wide range of chemical reactions could be studied using the setup under *operando* conditions.

Chapter 2 : A laboratory-based electrochemical NAP-XPS system for *operando* electrocatalysis studies

2.5 Conclusion

We have described a lab-based electrochemical NAP-XPS instrument optimized for electrocatalysis studies. The instrument is specifically designed to 1) facilitate measurements on a wide variety of electrochemical reactions under *operando* conditions, 2) enable simple, clean and (vacuum) safe operation, and 3) allow for fast sample and electrolyte exchange. Key to the design is the use of a spectro-electrochemical cell based on a membrane-electrode-graphene assembly. We show that this assembly facilitates measurements on all components of the electrode-electrolyte interface for any nanoparticle electrocatalyst and any aqueous electrolyte. Furthermore, we show that the membrane-catalyst-graphene assembly allows adequate mass transport of reactants, even for reactions involving dissolved gasses, as exemplified for the oxygen reduction reaction. We foresee that the step from the synchrotron to the lab is key for integrating electrochemical XPS into the electrochemist's toolbox, enabling a day-to-day feedback loop with the electrochemical lab.

Chapter 2 : A laboratory-based electrochemical NAP-XPS system for *operando* electrocatalysis studies

References

- (1) Handoko, A. D.; Wei, F.; Jenndy; Yeo, B. S.; Seh, Z. W. Understanding Heterogeneous Electrocatalytic Carbon Dioxide Reduction through Operando Techniques. *Nature Catalysis*. Nature Publishing Group December 1, 2018, pp 922–934. <https://doi.org/10.1038/s41929-018-0182-6>.
- (2) Chu, S.; Cui, Y.; Liu, N. The Path towards Sustainable Energy. *Nature Materials*. Nature Publishing Group December 20, 2016, pp 16–22. <https://doi.org/10.1038/nmat4834>.
- (3) Wakisaka, M.; Asizawa, S.; Watanabe, M.; Uchida, H.; Watanabe, M. In Situ STM Observation of Morphological Changes of the Pt(111) Electrode Surface during Potential Cycling in 10 MM HF Solution. *Physical Chemistry Chemical Physics* **2010**, 12 (16), 4184–4190. <https://doi.org/10.1039/b923956a>.
- (4) Marković, N. M.; Ross, P. N. Surface Science Studies of Model Fuel Cell Electrocatalysts. *Surf Sci Rep* **2002**, 45 (4–6), 117–229. [https://doi.org/10.1016/s0167-5729\(01\)00022-x](https://doi.org/10.1016/s0167-5729(01)00022-x).
- (5) Nguyen, L.; Tao, F. F.; Tang, Y.; Dou, J.; Bao, X. J. Understanding Catalyst Surfaces during Catalysis through Near Ambient Pressure X-Ray Photoelectron Spectroscopy. *Chemical Reviews*. American Chemical Society June 26, 2019, pp 6822–6905. <https://doi.org/10.1021/acs.chemrev.8b00114>.
- (6) Opitz, A. K.; Nenning, A.; Rameshan, C.; Kubicek, M.; Götsch, T.; Blume, R.; Hävecker, M.; Knop-Gericke, A.; Rupprechter, G.; Klötzer, B.; Fleig, J. Surface Chemistry of Perovskite-Type Electrodes during High Temperature CO₂ Electrolysis Investigated by Operando Photoelectron Spectroscopy. *ACS Appl Mater Interfaces* **2017**, 9 (41), 35847–35860. <https://doi.org/10.1021/acsami.7b10673>.
- (7) Opitz, A. K.; Nenning, A.; Rameshan, C.; Rameshan, R.; Blume, R.; Hävecker, M.; Knop-Gericke, A.; Rupprechter, G.; Fleig, J.; Klötzer, B. Enhancing Electrochemical Water-Splitting Kinetics by Polarization-Driven Formation of near-Surface Iron(0): An in Situ XPS Study on Perovskite-Type Electrodes. *Angewandte Chemie - International Edition* **2015**, 54 (9), 2628–2632. <https://doi.org/10.1002/anie.201409527>.
- (8) Zhong, L.; Chen, D.; Zafeirotos, S. A Mini Review of in Situ Near-Ambient Pressure XPS Studies on Non-Noble, Late Transition Metal Catalysts. *Catalysis Science and Technology*. Royal Society of Chemistry 2019, pp 3851–3867. <https://doi.org/10.1039/c9cy00632j>.
- (9) Stevie, F. A.; Donley, C. L. Introduction to X-Ray Photoelectron Spectroscopy. *Journal of Vacuum Science & Technology A: Vacuum, Surfaces, and Films* **2020**, 38 (6). <https://doi.org/10.1116/6.0000412>.
- (10) Ketenoglu, D. A General Overview and Comparative Interpretation on Element-Specific X-Ray Spectroscopy Techniques: XPS, XAS, and XRS. *X-Ray Spectrometry* **2022**, 51 (5–6), 422–443. <https://doi.org/10.1002/xrs.3299>.
- (11) Baraldi, A.; Comelli, G.; Lizzit, S.; Kiskinova, M.; Paolucci, G. Real-Time X-Ray Photoelectron Spectroscopy of Surface Reactions. *Surface Science Reports*. Elsevier 2003, pp 169–224. [https://doi.org/10.1016/S0167-5729\(03\)00013-X](https://doi.org/10.1016/S0167-5729(03)00013-X).

Chapter 2 : A laboratory-based electrochemical NAP-XPS system for *operando* electrocatalysis studies

- (12) Babenkov, S. V.; Aristov, V. Y.; Molodtsova, O. V.; Winkler, K.; Glaser, L.; Shevchuk, I.; Scholz, F.; Seltmann, J.; Viehhaus, J. A New Dynamic-XPS End-Station for Beamline P04 at PETRA III/DESY. *Nucl Instrum Methods Phys Res A* **2015**, 777, 189–193. <https://doi.org/10.1016/j.nima.2014.12.065>.
- (13) Salmeron, M. From Surfaces to Interfaces: Ambient Pressure XPS and Beyond. *Top Catal* **2018**, 61 (20), 2044–2051. <https://doi.org/10.1007/s11244-018-1069-0>.
- (14) Arrigo, R.; Hävecker, M.; Schuster, M. E.; Ranjan, C.; Stotz, E.; Knop-Gericke, A.; Schlögl, R. In Situ Study of the Gas-Phase Electrolysis of Water on Platinum by NAP-XPS. *Angewandte Chemie - International Edition* **2013**, 52 (44), 11660–11664. <https://doi.org/10.1002/anie.201304765>.
- (15) Favaro, M.; Jeong, B.; Ross, P. N.; Yano, J.; Hussain, Z.; Liu, Z.; Crumlin, E. J. Unravelling the Electrochemical Double Layer by Direct Probing of the Solid/Liquid Interface. *Nat Commun* **2016**, 7. <https://doi.org/10.1038/ncomms12695>.
- (16) Temperton, R. H.; Kawde, A.; Eriksson, A.; Wang, W.; Kokkonen, E.; Jones, R.; Gericke, S. M.; Zhu, S.; Quevedo, W.; Seidel, R.; Schnadt, J.; Shavorskiy, A.; Persson, P.; Uhlig, J. Dip-and-Pull Ambient Pressure Photoelectron Spectroscopy as a Spectroelectrochemistry Tool for Probing Molecular Redox Processes. *Journal of Chemical Physics* **2022**, 157 (24). <https://doi.org/10.1063/5.0130222>.
- (17) Teschner, D.; Plescher, J.; Piccinin, S.; Jones, T. E.; Hammud, A.; Schmidt, F.; Knop-Gericke, A.; Bluhm, H.; Shavorskiy, A. Understanding Anomalous Gas-Phase Peak Shifts in Dip-and-Pull Ambient Pressure XPS Experiments. *Journal of Physical Chemistry C* **2024**. <https://doi.org/10.1021/acs.jpcc.4c00113>.
- (18) Capone, F. G.; Sottmann, J.; Meunier, V.; Pérez Ramírez, L.; Grimaud, A.; Iadecola, A.; Scardamaglia, M.; Rueff, J. P.; Dedryvère, R. Operando Observation of the Dynamic SEI Formation on a Carbonaceous Electrode by Near-Ambient Pressure XPS. *Energy Environ Sci* **2024**, 17 (4), 1509–1519. <https://doi.org/10.1039/d3ee03228k>.
- (19) Casalongue, H. S.; Kaya, S.; Viswanathan, V.; Miller, D. J.; Friebe, D.; Hansen, H. A.; Nørskov, J. K.; Nilsson, A.; Ogasawara, H. Direct Observation of the Oxygenated Species during Oxygen Reduction on a Platinum Fuel Cell Cathode. *Nat Commun* **2013**, 4. <https://doi.org/10.1038/ncomms3817>.
- (20) Velasco-Velez, J. J.; Falling, L. J.; Bernsmeier, D.; Sear, M. J.; Clark, P. C. J.; Chan, T. S.; Stotz, E.; Hävecker, M.; Kraehnert, R.; Knop-Gericke, A.; Chuang, C. H.; Starr, D. E.; Favaro, M.; Mom, R. V. A Comparative Study of Electrochemical Cells for in Situ X-Ray Spectroscopies in the Soft and Tender x-Ray Range. *J Phys D Appl Phys* **2021**, 54 (12). <https://doi.org/10.1088/1361-6463/abd2ed>.
- (21) Falling, L. J.; Mom, R. V.; Sandoval Diaz, L. E.; Nakhaie, S.; Stotz, E.; Ivanov, D.; Hävecker, M.; Lunkenbein, T.; Knop-Gericke, A.; Schlögl, R.; Velasco-Vélez, J. J. Graphene-Capped Liquid Thin Films for Electrochemical Operando X-Ray Spectroscopy and Scanning Electron Microscopy. *ACS Appl Mater Interfaces* **2020**, 12 (33), 37680–37692. <https://doi.org/10.1021/acsami.0c08379>.
- (22) Weatherup, R. S.; Eren, B.; Hao, Y.; Bluhm, H.; Salmeron, M. B. Graphene Membranes for Atmospheric Pressure Photoelectron Spectroscopy. *Journal of Physical Chemistry Letters* **2016**, 7 (9), 1622–1627. <https://doi.org/10.1021/acs.jpclett.6b00640>.
- (23) Kolmakov, A.; Dikin, D. A.; Cote, L. J.; Huang, J.; Abyaneh, M. K.; Amati, M.; Gregoratti, L.; Günther, S.; Kiskinova, M. Graphene Oxide Windows for in Situ Environmental Cell Photoelectron Spectroscopy. *Nat Nanotechnol* **2011**, 6 (10), 651–657. <https://doi.org/10.1038/nnano.2011.130>.

Chapter 2 : A laboratory-based electrochemical NAP-XPS system for *operando* electrocatalysis studies

- (24) Stoerzinger, K. A.; Favaro, M.; Ross, P. N.; Hussain, Z.; Liu, Z.; Yano, J.; Crumlin, E. J. Stabilizing the Meniscus for Operando Characterization of Platinum During the Electrolyte-Consuming Alkaline Oxygen Evolution Reaction. *Top Catal* **2018**, 61 (20), 2152–2160. <https://doi.org/10.1007/s11244-018-1063-6>.
- (25) Ali-Löytty, H.; Louie, M. W.; Singh, M. R.; Li, L.; Sanchez Casalongue, H. G.; Ogasawara, H.; Crumlin, E. J.; Liu, Z.; Bell, A. T.; Nilsson, A.; Friebel, D. Ambient-Pressure XPS Study of a Ni-Fe Electrocatalyst for the Oxygen Evolution Reaction. *Journal of Physical Chemistry C* **2016**, 120 (4), 2247–2253. <https://doi.org/10.1021/acs.jpcc.5b10931>.
- (26) Favaro, M.; Drisdell, W. S.; Marcus, M. A.; Gregoire, J. M.; Crumlin, E. J.; Haber, J. A.; Yano, J. An Operando Investigation of (Ni-Fe-Co-Ce)Ox System as Highly Efficient Electrocatalyst for Oxygen Evolution Reaction. *ACS Catal* **2017**, 7 (2), 1248–1258. <https://doi.org/10.1021/acscatal.6b03126>.
- (27) Wang, Y.; Wang, W.; Xie, J.; Wang, C. H.; Yang, Y. W.; Lu, Y. C. Electrochemical Reduction of CO₂ in Ionic Liquid: Mechanistic Study of Li–CO₂ Batteries via in Situ Ambient Pressure X-Ray Photoelectron Spectroscopy. *Nano Energy* **2021**, 83. <https://doi.org/10.1016/j.nanoen.2021.105830>.
- (28) Permyakova, A. A.; Herranz, J.; El Kazzi, M.; Diercks, J. S.; Povia, M.; Mangani, L. R.; Horisberger, M.; Pătru, A.; Schmidt, T. J. On the Oxidation State of Cu₂O upon Electrochemical CO₂ Reduction: An XPS Study. *ChemPhysChem* **2019**, 20 (22), 3120–3127. <https://doi.org/10.1002/cphc.201900468>.
- (29) Liu, C.; Dong, Q.; Han, Y.; Zang, Y.; Zhang, H.; Xie, X.; Yu, Y.; Liu, Z. Understanding Fundamentals of Electrochemical Reactions with Tender X-Rays: A New Lab-Based Operando X-Ray Photoelectron Spectroscopy Method for Probing Liquid/Solid and Gas/Solid Interfaces across a Variety of Electrochemical Systems. *Chinese Journal of Catalysis* **2022**, 43 (11), 2858–2870. [https://doi.org/10.1016/S1872-2067\(22\)64092-0](https://doi.org/10.1016/S1872-2067(22)64092-0).
- (30) Griesser, C.; Winkler, D.; Moser, T.; Haug, L.; Thaler, M.; Portenkirchner, E.; Klötzer, B.; Diaz-Coello, S.; Pastor, E.; KunzeLiebhäuser, J. Lab-Based Electrochemical X-Ray Photoelectron Spectroscopy for in-Situ Probing of Redox Processes at the Electrified Solid/Liquid Interface. *Electrochemical Science Advances* **2023**. <https://doi.org/10.1002/elsa.202300007>.
- (31) Jürgensen, A.; Esser, N.; Hergenröder, R. Near Ambient Pressure XPS with a Conventional X-Ray Source. In *Surface and Interface Analysis*; 2012; Vol. 44, pp 1100–1103. <https://doi.org/10.1002/sia.4826>.
- (32) Arble, C.; Jia, M.; Newberg, J. T. Lab-Based Ambient Pressure X-Ray Photoelectron Spectroscopy from Past to Present. *Surface Science Reports*. Elsevier B.V. May 1, 2018, pp 37–57. <https://doi.org/10.1016/j.surfrep.2018.02.002>.
- (33) Haug, L.; Griesser, C.; Thurner, C. W.; Winkler, D.; Moser, T.; Thaler, M.; Bartl, P.; Rainer, M.; Portenkirchner, E.; Schumacher, D.; Dierschke, K.; Köpfle, N.; Penner, S.; Beyer, M. K.; Loerting, T.; Kunze-Liebhäuser, J.; Klötzer, B. A Laboratory-Based Multifunctional near Ambient Pressure X-Ray Photoelectron Spectroscopy System for Electrochemical, Catalytic, and Cryogenic Studies. *Review of Scientific Instruments* **2023**, 94 (6). <https://doi.org/10.1063/5.0151755>.
- (34) Plodinec, M.; Knop-gericke, A.; Schlo, R.; Jones, T. E. In Situ X - Ray Spectroscopy of the Electrochemical Development Of. *Journal of Physical Chemistry C* **2019**, 123 (1), 9146–9152. <https://doi.org/10.1021/acs.jpcc.9b00731>.

Chapter 2 : A laboratory-based electrochemical NAP-XPS system for *operando* electrocatalysis studies

- (35) Mom, R.; Frevel, L.; Velasco-Vélez, J. J.; Plodinec, M.; Knop-Gericke, A.; Schlögl, R. The Oxidation of Platinum under Wet Conditions Observed by Electrochemical X-Ray Photoelectron Spectroscopy. *J Am Chem Soc* **2019**, *141* (16), 6537–6544. <https://doi.org/10.1021/jacs.8b12284>.
- (36) Frevel, L. J.; Mom, R.; Velasco-Vélez, J. J.; Plodinec, M.; Knop-Gericke, A.; Schlögl, R.; Jones, T. E. In Situ X-Ray Spectroscopy of the Electrochemical Development of Iridium Nanoparticles in Confined Electrolyte. *Journal of Physical Chemistry C* **2019**, *123* (14), 9146–9152. <https://doi.org/10.1021/acs.jpcc.9b00731>.
- (37) Mom, R. V.; Falling, L. J.; Kasian, O.; Algara-Siller, G.; Teschner, D.; Crabtree, R. H.; Knop-Gericke, A.; Mayrhofer, K. J. J.; Velasco-Vélez, J. J.; Jones, T. E. Operando Structure-Activity-Stability Relationship of Iridium Oxides during the Oxygen Evolution Reaction. *ACS Catal* **2022**, *12* (9), 5174–5184. <https://doi.org/10.1021/acscatal.1c05951>.
- (38) Velasco-Vélez, J. J.; Jones, T. E.; Streibel, V.; Hävecker, M.; Chuang, C. H.; Frevel, L.; Plodinec, M.; Centeno, A.; Zurutuza, A.; Wang, R.; Arrigo, R.; Mom, R.; Hofmann, S.; Schlögl, R.; Knop-Gericke, A. Electrochemically Active Ir NPs on Graphene for OER in Acidic Aqueous Electrolyte Investigated by in Situ and Ex Situ Spectroscopies. *Surf Sci* **2019**, *681* (September 2018), 1–8. <https://doi.org/10.1016/j.susc.2018.10.021>.
- (39) Velasco-Velez, J. J.; Pfeifer, V.; Hävecker, M.; Weatherup, R. S.; Arrigo, R.; Chuang, C.; Stotz, E.; Weinberg, G.; Salmeron, M.; Schlögl, R.; Knop-Gericke, A. Photoelectron Spectroscopy at the Graphene–Liquid Interface Reveals the Electronic Structure of an Electrodeposited Cobalt/Graphene Electrocatalyst. *Angewandte Chemie* **2015**, *127* (48), 14762–14766. <https://doi.org/10.1002/ange.201506044>.
- (40) VICI AG International. *Chemical Resistance PEEK® and Other Polymers General Reference*. https://www.daichem.co.jp/system/wp-content/themes/daichem2017/pdf/Chemical_resistance_jour.pdf. (accessed 2nd September, 2024)
- (41) Javed, H.; Knop-Gericke, A.; Mom, R. V. Structural Model for Transient Pt Oxidation during Fuel Cell Start-up Using Electrochemical X-Ray Photoelectron Spectroscopy. *ACS Appl Mater Interfaces* **2022**, *14* (31), 36238–36245. <https://doi.org/10.1021/acscami.2c09249>.
- (42) Myers, D. J.; Wang, X.; Smith, M. C.; More, K. L.; Soc, J. E.; Myers, D. J.; Wang, X.; Smith, M. C.; More, K. L. Potentiostatic and Potential Cycling Dissolution of Polycrystalline Platinum and Platinum Nano-Particle Fuel Cell Catalysts. *J Electrochem Soc* **2018**, *165* (6), F3178–F3190. <https://doi.org/10.1149/2.0211806jes>.
- (43) Lopes, P. P.; Tripkovic, D.; Martins, P. F. B. D. B. D.; Strmcnik, D.; Ticianelli, E. A.; Stamenkovic, V. R.; Markovic, N. M. Dynamics of Electrochemical Pt Dissolution at Atomic and Molecular Levels. *Journal of Electroanalytical Chemistry* **2017**, *819* (September), 0–1. <https://doi.org/10.1016/j.jelechem.2017.09.047>.
- (44) Holby, E. F.; Morgan, D. Application of Pt Nanoparticle Dissolution and Oxidation Modeling to Understanding Degradation in PEM Fuel Cells. *J Electrochem Soc* **2012**, *159* (5), B578–B591. <https://doi.org/10.1149/2.011204jes>.

Chapter 2 : A laboratory-based electrochemical NAP-XPS system for *operando* electrocatalysis studies

- (45) Yu, Y.; Tu, Z.; Zhang, H.; Zhan, Z.; Pan, M. Comparison of Degradation Behaviors for Open-Ended and Closed Proton Exchange Membrane Fuel Cells during Startup and Shutdown Cycles. *J Power Sources* **2011**, *196* (1), 5077–5083. <https://doi.org/10.1016/j.jpowsour.2011.01.075>.
- (46) Zhang, S.; Yuan, X.; Ng, J.; Hin, C.; Wang, H.; Friedrich, K. A.; Schulze, M. A Review of Platinum-Based Catalyst Layer Degradation in Proton Exchange Membrane Fuel Cells. *J Power Sources* **2009**, *194* (1), 588–600. <https://doi.org/10.1016/j.jpowsour.2009.06.073>.
- (47) Yeon, Y.; Cho, E.; Hyeun, J.; Lim, T.; Oh, I.; Kim, S.; Kim, H.; Hyun, J. Degradation of Polymer Electrolyte Membrane Fuel Cells Repetitively Exposed to Reverse Current Condition under Different Temperature. *J Power Sources* **2011**, *196* (23), 9906–9915. <https://doi.org/10.1016/j.jpowsour.2011.08.035>.
- (48) Randrianarizafy, B.; Schott, P.; Gerard, M.; Bultel, Y. Modelling Carbon Corrosion during a PEMFC Startup : Simulation of Mitigation Strategies. **2020**, 10–16. <https://doi.org/10.3390/en13092338>.
- (49) Yu, Y.; Li, H.; Wang, H.; Yuan, X.; Wang, G.; Pan, M. A Review on Performance Degradation of Proton Exchange Membrane Fuel Cells during Startup and Shutdown Processes : Causes , Consequences , and Mitigation Strategies. *J Power Sources* **2012**, *205* (1), 10–23. <https://doi.org/10.1016/j.jpowsour.2012.01.059>.
- (50) Shard, A. G. A Straightforward Method for Interpreting XPS Data from Core-Shell Nanoparticles. *Journal of Physical Chemistry C* **2012**, *116* (31), 16806–16813. <https://doi.org/10.1021/jp305267d>.
- (51) Ertl, G., Küppers, J., & Grasserbauer, M. Low Energy Electrons and Surface Chemistry. *Anal Chim Acta* **1987**, *199* (1), 272–273. [https://doi.org/https://doi.org/10.1016/s0003-2670\(00\)82831-7](https://doi.org/https://doi.org/10.1016/s0003-2670(00)82831-7).
- (52) Shinotsuka, H.; Da, B.; Tanuma, S.; Yoshikawa, H.; Powell, C. J.; Penn, D. R. Calculations of Electron Inelastic Mean Free Paths. XI. Data for Liquid Water for Energies from 50 eV to 30 keV. *Surface and Interface Analysis* **2017**, *49* (4), 238–252. <https://doi.org/10.1002/sia.6123>.

Chapter 3

A structural model for transient Pt oxidation during fuel cell start-up using electrochemical X-ray photoelectron spectroscopy

Abstract:

Potential spikes during the start-up and shutdown of fuel cells are a major cause of platinum electrocatalyst degradation, which limits the lifetime of the device. The electrochemical oxidation of platinum (Pt) that occurs on the cathode during the potential spikes plays a key role in this degradation process. However, the composition of the oxide species formed, as well as their role in catalyst dissolution remains unclear. In this study, we employ a special arrangement of XPS (X-ray Photoelectron Spectroscopy), in which the platinum electrocatalyst is covered by a graphene spectroscopy window, making the in situ examination of the oxidation/reduction reaction under wet conditions possible. We use this assembly to investigate the change in the oxidation states of Pt within the potential window relevant to fuel cell operation. We show that above 1.1 V_{RHE} (potential vs. Reversible Hydrogen Electrode), a mixed Pt^{δ+}/Pt²⁺/Pt⁴⁺ surface oxide is formed, with an average oxidation state that gradually increases as the potential is increased. By comparing a model based on the XPS data to the oxidation charge measured during potential spikes, we show that our description of Pt oxidation is also valid during the transient conditions of fuel cell start-up and shut-down. This is due to the rapid Pt oxidation kinetics during the pulses. As a result of the irreversibility of Pt oxidation, some remnants of oxidized Pt remain at typical fuel cell operating potentials after a pulse.

This Chapter has been published in ACS Advanced Materials & Interfaces:

Javed, H.; Knop-Gericke, A.; Mom, R. V. Structural Model for Transient Pt Oxidation during Fuel Cell Start-up Using Electrochemical X-Ray Photoelectron Spectroscopy. *ACS Appl. Mater. Interfaces* 2022, 14 (31), 36238–36245. <https://doi.org/10.1021/acsami.2c09249>.

Chapter 3 : A structural model for transient Pt oxidation during fuel cell start-up using electrochemical X-ray photoelectron spectroscopy

3.1 Introduction

Fuel cells have the potential to play a pivotal role in the transition to sustainable energy systems. They are employed in a wide range of applications, including transportation, power generation, and material handling, offering a potentially CO₂-free alternative to the traditional internal combustion engines^{1–4}. Presently, platinum is the best catalyst for polymer electrolyte fuel cells (PEMFCs), for both the anodic and the cathodic half reactions. However, the activity of the cathode decreases over time due to Pt dissolution, which causes a reduction of the electrochemically active surface area (ECSA)^{5–7}. At present, this degradation of the cathode is limiting the life time of fuel cells^{4,5,8–10}. Hence, mitigating Pt dissolution is a key step in fuel cell development.

The degradation of fuel cell cathodes primarily occurs during changes in the operating conditions, such as startup/shut down (SU/SD), fuel supply fluctuations, and load variations^{11–13}. Especially for automotive applications, such transient conditions are inevitable due to starting and stopping of the vehicle^{4,14}. Pei and coworkers divided the working conditions in a PEMFC into four categories; load changing, SU/SD, high power and idling. They found that the SU/SD alone contributes ~33% to the degradation of the cathode, even though the fuel cell was only fully shut down once per hour of driving time^{11–13}. The reason for this disproportionate contribution of SU/SD is that uncontrolled transient voltage spikes up to 1.4 V_{RHE} occur during the SU/SD¹⁵. These cause significant degradation of Pt due to rapid oxidation/reduction and corrosion of the carbon support¹⁶. Indeed, transient degradation of the Pt catalyst has been found to occur at a much faster rate compared to steady state operation where such high potentials are rarely reached^{12,18–22}. Son and coworkers verified this in their publications, where they found that the Pt loading at the cathode decreases by half just after 1500 SU/SD cycles at 100% relative humidity, and noticed a significant decrease in the current density and ECSA^{9,23–25}. It has been shown that the reduction in ECSA is closely linked to the dissolution of Pt nanoparticles^{6,7,26}. In turn, Pt dissolution has been linked to oxidation/reduction of Pt^{27–29}, highlighting the key role of Pt oxides in fuel cell degradation.

A point of debate is the mechanism by which Pt oxide formation/reduction is linked to the degradation mechanisms that occur in fuel cells. Since Pt dissolution can occur during both oxide formation and reduction, as well as under (highly anodic) potentiostatic conditions, several types of dissolution reactions seem to occur. Oxidative, reductive and chemical dissolution reactions have all been proposed, each with sub-varieties depending on whether Pt, Pt-OH_{ads}, Pt-O_{ads}, PtO, or PtO₂ is involved^{27,28,30–35}.

An important reason for the co-existence of this plethora of proposed Pt dissolution mechanisms is that the composition of the oxides involved in the process is not known. For equilibrium conditions, it has been established that electrochemical oxidation of Pt at potentials above ~1 V_{RHE} yields an amorphous oxide layer, which typically contains a mixture of oxidation states^{20,34,36,37}. Even for the very early stages of oxidation, the entire oxidation state range of Pt^{δ+}, Pt²⁺, and Pt⁴⁺ can be detected. The question now arises whether this also holds for the transient conditions relevant to the start-up or shutdown of fuel cells. In addition, the reduction potential for Pt oxides lies within the range 0.9-0.5 V_{RHE} and the operating

Chapter 3 : A structural model for transient Pt oxidation during fuel cell start-up using electrochemical X-ray photoelectron spectroscopy

potential of fuel cell is $\sim 0.7 V_{\text{RHE}}^{12}$, making it uncertain whether complete reduction will be achieved after a start-up pulse.

In this publication, we address these questions through the combination of in situ X-ray photoelectron spectroscopy (XPS), X-ray absorption spectroscopy (XAS), and electrochemical measurements. To enable the in situ measurements, we made use of our previously developed confined electrolyte approach^{20,38,39}, in which the Pt nanoparticles are sandwiched between a proton exchange membrane and a graphene window that separates the wet electrochemical environment from the vacuum of the spectroscopy set-up. Using this methodology, we investigated the oxidation behavior of platinum during steady state and transient conditions. Detailed XP spectra show the evolution of the Pt surface structure during both oxidation and reduction. Based on this data, a model is derived to predict the oxidation charge measured in electrochemical measurements. We show that this model is in good agreement with the oxidation charge measured during SU/SD potential spikes reproduced in an electrochemical cell, thus underlining the universality of the model even for transient conditions.

3.2 Methods

i) Electrochemical measurements

The electrochemical measurements were done in a home-made electrochemical cell. The cell utilizes a three-electrode setup, with a Platinum wire (ChemPUR, 99.9%) as a counter electrode and an RHE as a reference electrode. Experiments were done in a two-compartment glass cell cleaned with acidic potassium permanganate (0.5 M H₂SO₄ solution (Sigma-Aldrich, 95.0 – 97.0%) containing 1 g L⁻¹ KMnO₄ (Sigma-Aldrich, $\geq 99.0\%$)) and dilute piranha solution (~ 1 M H₂SO₄ (Sigma-Aldrich, 95.0 – 97.0%) and $\sim 6\%$ H₂O₂ (Merck KGaA, 35%)) followed by repetitive boiling in ultra-pure water ((Merck Milli-Q® IQ 7000, < 5 ppb total organic content (TOC), $18.2 \text{ M}\Omega\cdot\text{cm}$ at 298 K)). The working electrode was prepared by sputter depositing platinum onto a glassy carbon substrate. The catalyst loading was kept at 3–3.5 nm, as verified using a quartz crystal microbalance. Throughout this manuscript, the catalyst loading here is expressed as layer thickness. After Pt deposition, a thin layer of Nafion ionomer (Sigma Aldrich, 5% solution) was deposited on the Pt/C electrode by drop casting. The Nafion drop on the working electrode was dried in a lab-made desiccator to give a uniform layer of ionomer on top of the platinum nanoparticles. The Nafion coated working electrode was transferred to the cell from the dessicator covered in a droplet of ultra-pure water to avoid contamination from the ambient. The electrolyte used in the cell was prepared at a concentration of 0.1 M using a Sulphuric acid stock solution (Sigma Aldrich, 99.9% solution) and ultra-pure deionized water (Merck). Before the start of the experiments, the Pt wire used as the counter electrode was flame-annealed and cooled in ultra-pure water and the working electrode was cycled between $0.05 V_{\text{RHE}}$ and $1.3 V_{\text{RHE}}$ to verify the quality and the cleanliness of the solution. The experiment was carried out using 0.1 M H₂SO₄. The setup was connected to a potentiostat (AutoLab, VSP-300) to conduct the electrochemical experiments. The maximum vertex potentials applied during the experiments were $0.05 V_{\text{RHE}}$ – $1.4 V_{\text{RHE}}$. All the experiments are carried out at room temperature using a static electrode configuration with a hanging meniscus maintained between the electrolyte and the working electrode.

Chapter 3 : A structural model for transient Pt oxidation during fuel cell start-up using electrochemical X-ray photoelectron spectroscopy

ii) In situ XPS

For the current application, a special arrangement of an in situ electrochemical cell was used. The construction of this cell has been described in detail in one of our earlier publications^{20,39,38} so here only a brief overview is given. The cell is made up of platinum nanoparticles sandwiched between a proton exchange membrane and a graphene layer, as shown in Figure 3.1. A Pt wire (ChemPUR, 99.9% pure) is used as a counter electrode and a Ag/AgCl reference electrode, both housed in a flow channel behind the membrane. A detailed account of the sample preparation of the in situ spectroscopy cell is given in the supporting information (supplementary information B3.1).

For the purpose of analysis later, the potentials were converted to an RHE scale. The purpose of the graphene layer is to serve as an electrical contact between the catalyst nanoparticles even if they are scattered, as well as prevent excessive evaporation of the electrolyte into the vacuum when the in situ cell is being examined by XPS and XAS. Due to a steady flow of the electrolyte diffusing through the proton exchange membrane combined with reduced evaporation owing to the graphene capping, we can probe the catalyst under wet electrochemical conditions. It has been investigated previously that the graphene layer installed on top of the catalyst layer is transparent to photoelectrons ($>300\text{ eV}$ K.E for single layer graphene and $>400\text{ eV}$ K.E for double layer graphene)^{20,38}.

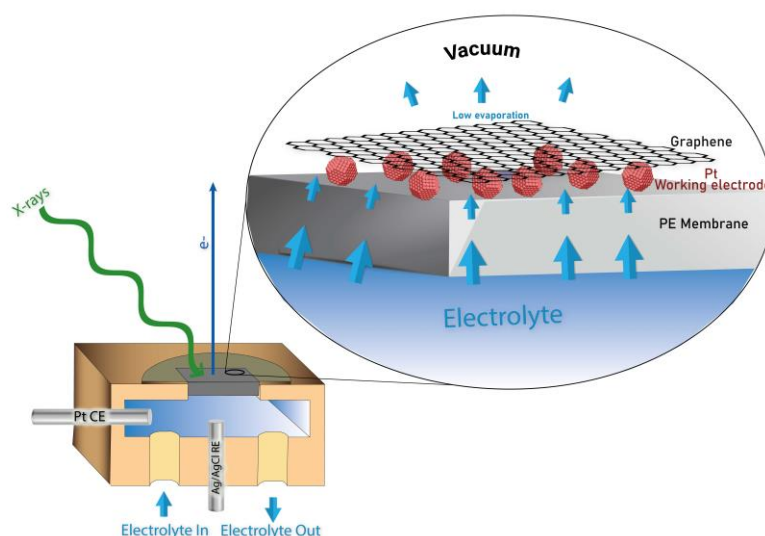


Figure 3.1: Schematic diagram and functioning of the in situ XPS cell

For the purpose of this study, we use double layer graphene as our electron transparent window. The platinum (Electronen-Optik-Service GmbH target) was deposited on the proton exchange membrane using a Cressington sputter coater yielding a uniform layer thickness of approximately 2-3 nm.

The proton exchange membrane used in the cell was Nafion 117 (Ion Power), which allows the diffusion of water and protons to and from the Pt particles. For in situ XPS examination, the near-ambient pressure XPS end station (NAPXPS1) of the ISSS beamline at the BESSY II/HZB synchrotron facility in Berlin, Germany was utilized. There were no gases introduced into the cell and the chamber pressure was determined at 0.05 mbar to 0.15 mbar. Regarding the XAS

Chapter 3 : A structural model for transient Pt oxidation during fuel cell start-up using electrochemical X-ray photoelectron spectroscopy

measurements, a partial electron yield signal was collected by the analyzer at a kinetic energy of 385 eV. Prior to the measurements, the potential was cycled between the 0.05-1.3 V_{RHE} several times at 50 mVs⁻¹ beforehand, to prevent any memory effects from interfering with the results.

During the measurements, care was taken that the cell assembly does not endure beam damage. Therefore, all the individual measurements were taken at fresh spots on the surface.

The data from X-ray photoelectron spectroscopy experiments was processed in CASA XPS software. The platinum 4f spectra were deconvoluted into peaks and fitted using 4 doublets corresponding to Pt⁰, Pt²⁺, Pt^{δ+} and Pt⁴⁺ with corresponding binding energies taken from the literature⁴⁰ and the spin-orbit splitting between the doublets kept constant at +3.33eV. Details of the fitting procedure are given in supplementary information B3.4.

3.3 Results and discussions

For our electrochemical characterization, accurate potential control of the working electrode is essential. We therefore employed a model catalyst that could be inserted into a classical three-electrode glass cell with an RHE reference electrode. As described in the methods section, our model catalyst contains the principal components of a fuel cell cathode, consisting of a glassy carbon support coated with Pt nanoparticles and covered with a thin layer of Nafion. As shown in Figure 3.2, our model system yields a cyclic voltammogram that exhibits the characteristic features of clean Pt nanoparticles, in good agreement with literature results⁴¹ and PEMFC performance studies carried out under gas diffusion electrode conditions (using Pt/Carbon + Nafion ink)^{42–44}.

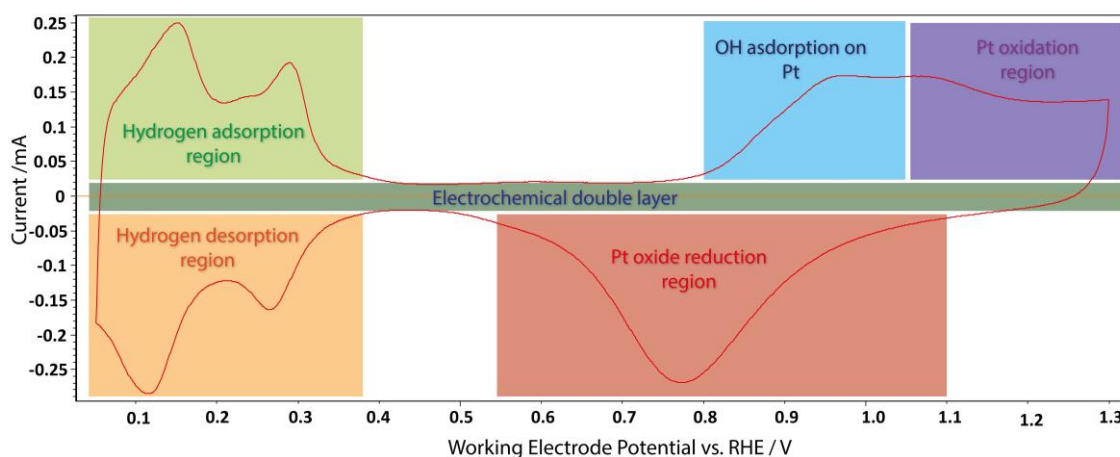


Figure 3.2: Cyclic voltammogram recorded from the electrochemical cell for Pt nanoparticles on a glassy carbon support with a Nafion film covering in an Ar saturated 0.1M H₂SO₄ electrolyte at a sweep rate of 50 mVs⁻¹

Typical hydrogen adsorption/ desorption features are observed between 0.05 V_{RHE} and 0.4 V_{RHE}⁴⁵. The electrochemically active surface area (ECSA) of Pt was calculated via the area of the hydrogen desorption peaks in the cyclic voltammograms using equation (1):

Chapter 3 : A structural model for transient Pt oxidation during fuel cell start-up using electrochemical X-ray photoelectron spectroscopy

$$ECSA (cm^2) = \frac{Q_H}{0.21} \quad (1)$$

Where Q_H represents the hydrogen desorption charge ($mC.cm^{-2}$) and $0.21 mC.cm^{-2}$ stands for the charge that is needed to oxidize a monolayer of H adsorbed on Pt surface^{46,47}. The ECSA calculated using this expression will be used to normalize the oxidation/reduction currents in the following sections.

To replicate the potential spikes that occur during the start-up or shutdown of a fuel cell, we applied 5 second pulses to potentials in the range of $1.2 V_{RHE}$ to $1.4 V_{RHE}$. Modeling and local potential measurements during fuel cell start-up/shut-down^{17,48,49} showed that such high potentials indeed occur on fuel cell cathodes when the gas feed on the anode is changed from air to H_2 or vice versa. The potential range between $1.2 V_{RHE}$ and $1.4 V_{RHE}$ is enough to oxidize the Pt particles. To determine the amount of oxide formed during the pulse, the oxide was reduced in a linear sweep voltammogram (LSV) at $50 mVs^{-1}$ (see Figure 3.3a).

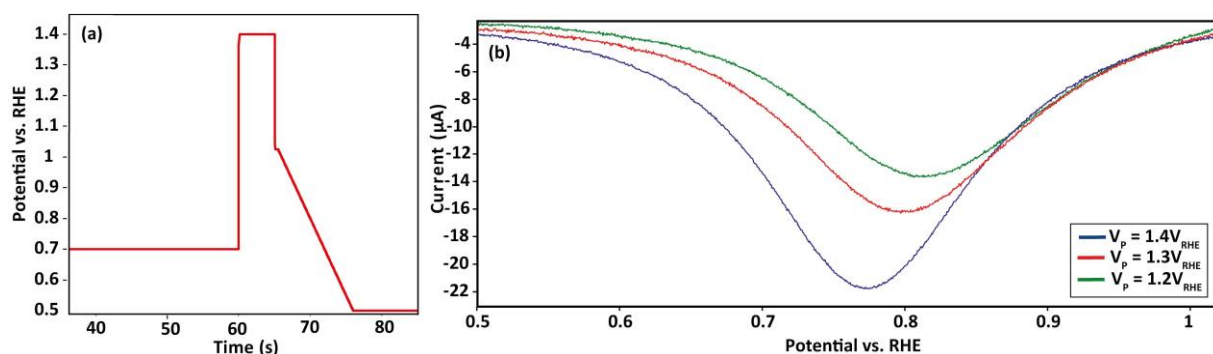


Figure 3.3: Potential transients to replicate and quantify oxide formation during fuel cell start-up and shut-down (a) Voltage scheme applied (b) Oxide reduction peak following pulses to various potentials ($V_p=1.2, 1.3$ and $1.4 V_{RHE}$). Inset shows the typical Current vs. Time response to the applied transient voltage scheme

The reduction peaks for different pulse potentials are shown in Figure 3.3(b). It can be clearly observed that increasing the pulse potential results in a larger reduction peak, i.e. more oxide formation. Concomitantly, the reduction peak shifts to lower potentials, indicating that the oxidation/reduction reaction becomes increasingly irreversible for larger amounts of oxide, in line with literature results^{50,51}.

Using our in situ XPS approach, we have explored the composition of the Pt oxides. To ensure that these measurements were conducted under representative wet electrochemical conditions, we recorded O-K edge XAS spectra during the experiments (see supporting information (supplementary information B3.6). In line with previous work^{38,39}, the spectra show a clear fingerprint of liquid water, confirming that the catalyst layer was properly wetted. Having established this, we recorded XPS and XAS spectra while stepwise increasing and decreasing the potential.

Chapter 3 : A structural model for transient Pt oxidation during fuel cell start-up using electrochemical X-ray photoelectron spectroscopy

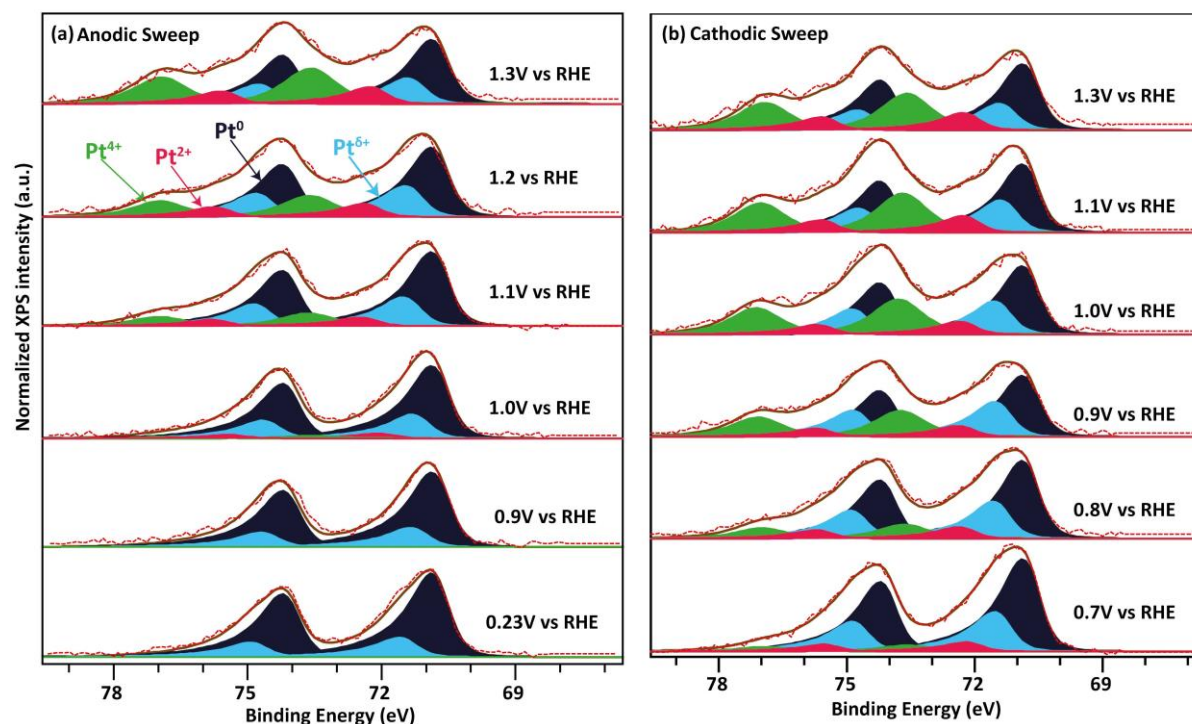


Figure 3.4: Pt 4f spectra of 2-4 nm Pt on Nafion during a stepwise increase and decrease of the potential. Excitation energy 600 eV, fit model: Pt^0 (Navy Blue), $\text{Pt}^{\delta+}$ (Sky Blue), Pt^{2+} (Pink) and Pt^{4+} (Green). The dashed red line shows the raw XPS data and the brown line shows the curve fitting for the raw data. A Shirley background subtraction was applied to all spectra. a) Stepwise anodization of the Pt nanoparticles. b) Stepwise decrease of the potential. All Pt 4f spectra are normalized to the Pt^0 peak at 71 eV.

Figure 3.4 shows the Pt 4f spectra recorded during the potential stepping. As described in the methods section, the collected spectra are fitted with doublets of Pt^0 , $\text{Pt}^{\delta+}$, Pt^{2+} , and Pt^{4+} . It can be observed that at low potentials (0.23 V_{RHE}), the main contributor other than Pt^0 is the $\text{Pt}^{\delta+}$ component. As highlighted in previous work, at potentials below the oxidation potential of Pt ($\sim 0.9 V_{\text{RHE}}$), this contribution likely occurs due to the interaction of Pt surface atoms with adsorbates such as R-SO_3^- , OH, or O. These adsorbates carry negative charge, inducing a $\delta+$ charge in the Pt surface atoms. Above the Pt oxidation potential (1.0 V_{RHE}), the formation of a Pt-PtO_x interface or 2D oxide could induce a similar effect on the Pt surface atoms, resulting in a similar $\text{Pt}^{\delta+}$ component. The intensity of the $\text{Pt}^{\delta+}$ component slightly increases as the potential is raised, particularly from 0.9 V_{RHE} to 1.0 V_{RHE} , consistent with the increased coverage of O_{ads} and OH_{ads} in this potential range. The onset of oxidation of Pt occurs at potentials higher than 0.9 V_{RHE} , where we start to observe the presence of 2+ and 4+ oxidation states. Beyond 1.0 V_{RHE} , a noticeable contribution of both Pt^{2+} and Pt^{4+} can be observed indicating the onset of oxidation. These oxides are likely hydrous, but this could not be clearly resolved by the comparison of the in situ O-K edge data (see supplementary information B3.6) to reference spectra of hydrous and non-hydrous PtO_2 . The appearance of both Pt^{2+} and Pt^{4+} at the onset of Pt oxidation indicates that a surface oxide with a complex structure is formed, in agreement with the poorly ordered structures observed by electrochemical scanning tunneling microscopy experiments³⁴ and the broad Pt L₃ absorption edge observed by Cuenya and

Chapter 3 : A structural model for transient Pt oxidation during fuel cell start-up using electrochemical X-ray photoelectron spectroscopy

coworkers³⁷. Hence, the surface oxidation of Pt clearly deviates from the regular $\text{Pt}^0 \rightarrow \text{Pt}^{2+} \rightarrow \text{Pt}^{4+}$ oxidation series predicted by Pourbaix diagrams.

Modeling of the observed oxide-to-metal ratio allows us to get a rough estimate of the thickness of the oxide layer. To obtain a reasonable estimate, it is important to consider the nanoparticle morphology of the sample, which boosts the XPS signal of the oxide shell relative to the metallic core. An exact consideration of the morphology is challenging, but we have made approximations using Shard's model⁵³ and Ertl and Küpper's model⁵⁴ (details in SI-B3.8). As shown in Figure 3.5, we obtain very modest oxide thicknesses, which do not exceed a monolayer. Hence, we conclude that only the outer Pt layer is oxidized in the potential range considered here. Note that the level of oxidation of the outer Pt layer likely varies for the different facets on the nanoparticles. However, this does not affect the quantitative analysis that we will discuss in the following paragraphs.

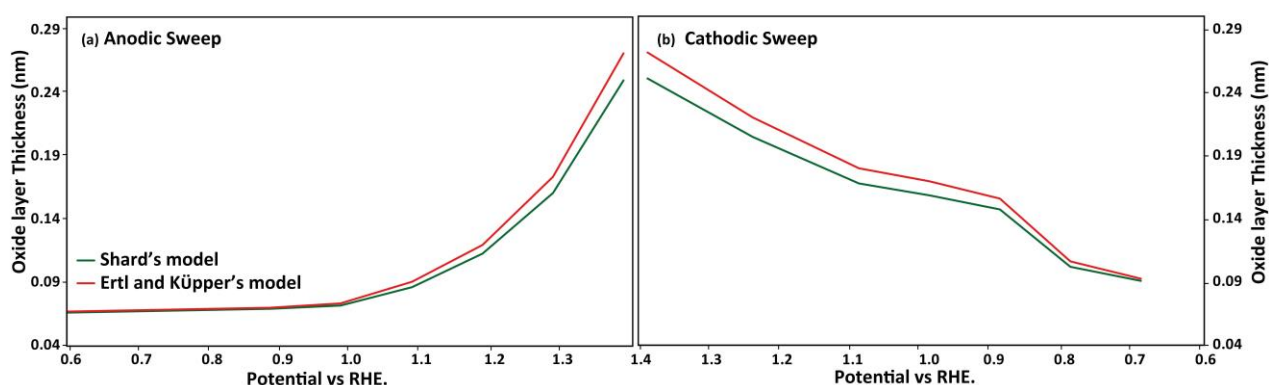


Figure 3.5: Modelling the oxide layer thickness by using Shard's model (green) and Ertl and Küpper's model (red) for (a) Anodic sweep and (b) Cathodic sweep

An essential difference between our XPS experiments and the transient pulses that occur during fuel cell start-up or shutdown is the time scale. For the XPS experiments, the potential is increased stepwise, at a rate of about 10 minutes per step. The pulses in a fuel cell, on the other hand, only last about 5 seconds¹⁷. To test how representative the XPS data is of the oxidation processes under transient conditions, we used the surface structures observed in XPS to predict the electrochemical oxidation charge observed during the pulse experiments of Figure 3.3. The details of how the XPS data shown in Figure 3.4 was modified to represent the surface of the nano-particle can be found in supplementary information B3.5. For modelling the oxidation charge, we used the $\text{Pt}^{\delta+}/\text{Pt}^{2+}/\text{Pt}^{4+}$ ratio observed in Figure 3.4a, and the oxide thickness (~ 1 monolayer). We assumed that a $1e^-$, $2e^-$, or $4e^-$ transfer was involved in creating $\text{Pt}^{\delta+}$, Pt^{2+} , and Pt^{4+} , respectively. For example, this would lead to $2e^-$ transferred per surface Pt atom in order to form a 100% Pt^{2+} layer from a fully metallic surface, or $3e^-$ transferred for a 50% Pt^{2+} , 50% Pt^{4+} layer. We also corrected for the contribution from surface adsorbed oxygen species by subtracting the no. of electrons transferred at $0.9 \text{ V}_{\text{RHE}}$ from the calculated total charge transfer. In this way, the oxidation charge per Pt surface atom from the XPS data was modeled for $1.2 \text{ V}_{\text{RHE}}$, $1.3 \text{ V}_{\text{RHE}}$, and $1.4 \text{ V}_{\text{RHE}}$ (extrapolated). To obtain the oxidation charge from the electrochemical experiments, the reduction peaks in Figure 3.3(b) were integrated. We

Chapter 3 : A structural model for transient Pt oxidation during fuel cell start-up using electrochemical X-ray photoelectron spectroscopy

excluded the contribution of double layer capacitance as much as possible by subtracting the baseline from the LSV curve prior to integration. To express the oxidation charge in e^- per surface Pt atom, we normalized the measured charge using the H_{UPD} peaks obtained in cyclic voltammetry.

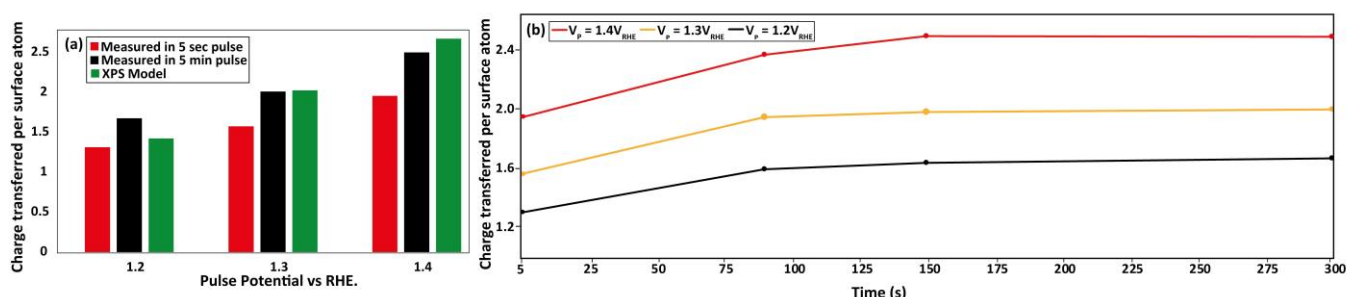


Figure 3.6: (a) Charge transferred during Pt oxidation, according to the measurements of Figure 3.3 and a model based on the XPS data. (b) Variation of charge transferred per Pt surface atom as a function of the pulse duration.

Figure 3.6 displays the comparison between the XPS model and the measured oxidation charge transferred for 5 sec and 5 min potential pulses. Clearly the agreement is good, indicating that the XPS measurements have adequately captured the oxidation processes during the potential spikes. The agreement is particularly good for the 5 minute pulses, which have a fairly similar time scale as the XPS measurements. However, even for the 5 sec potential spikes, the XPS model overestimates the transferred charge by only ~25%. The reason for this, is that the time scale of the oxidation has only a modest impact on the formed oxide. This is clearly visible in pulse oxidation experiments with varying pulse duration (see Figure 3.6b). The vast majority of the Pt oxidation occurs within the first few seconds as shown in Figure 3.6b (see also supplementary information B3.7 for in situ XAS confirmation of this), while only some ~25% additional oxidation charge is collected if the pulses are prolonged to several minutes. This indicates that the oxidation kinetics are fast, which is made possible by the fact that only the outer surface layer is oxidized in the potential range discussed here. Such surface oxidation does not require the (slow) diffusion of ions through the oxide layer, making it much faster than the bulk oxidation of Pt^{55} . As a result, we can conclude that our XPS data are representative of the oxides formed during transient potential spikes, i.e. that a surface layer of mixed oxidation state will also be formed under these conditions as well.

We will now shift our attention to the reduction of the oxides. Following the anodization up to 1.3 V_{RHE} in our XPS experiments, the potential was stepped down (cathodic sweep). Consistent with the typical irreversibility of Pt oxidation^{26,31,56} (see also Figure 3.2), the reduction of the Pt^{2+} and Pt^{4+} components follows a significantly different path than their formation (Figure 3.4 a, b and Supplementary information B3.2). Little change in the proportion of oxidation states is observed down to 1.0 V_{RHE} . At lower potentials (Figure 3.4 b), we see a sharp reduction in the amount of oxide, primarily in the Pt^{4+} component. Important to note is that despite the long time that was allowed for the cathodic sweep (~10 min per potential step), remnants of oxidized Pt remain on the surface of the particles at 0.9 V_{RHE} and 0.8 V_{RHE} , and to some extent even at 0.7 V_{RHE} . Since the typical operating range for fuel cell cathodes is about 0.7 V_{RHE} to 0.9

Chapter 3 : A structural model for transient Pt oxidation during fuel cell start-up using electrochemical X-ray photoelectron spectroscopy

V_{RHE} , this suggests that some oxides remain on the surface after a potential spike during start-up. Such oxide remnants would likely block active sites^{6,31,57}.

To further visualize the remnants of oxide following fuel cell start-up conditions, we conducted a transient voltammetry experiment, with three pulses of increasing potential on a baseline of 0.7 V_{RHE} (see Figure 3.7a). As shown in Figure 3.7(b), this experiment results in the accumulation of oxidative charge, again confirming that oxides remain following the pulses. The amount of oxide remnants scales with the pulse potential which can be estimated from the percentage of the oxidative charge that is not recovered during the reduction during the potential pulses (~6-8% of the oxidation charge). This can be explained by the larger amount of oxide that is formed at higher potentials. A second contributing factor, as Figure 3.3 showed, is that the irreversibility of the oxidation/reduction increases for higher pulse potentials.

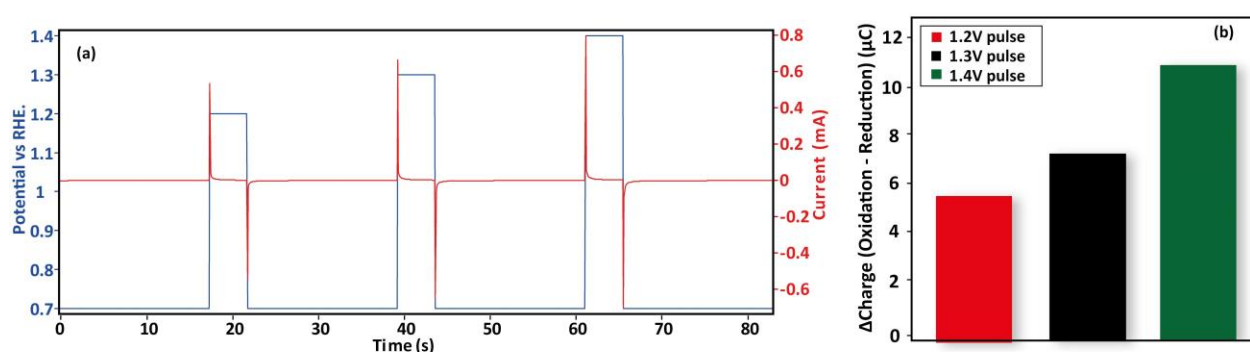


Figure 3.7: Consecutive pulse experiment (a) The applied voltage scheme (b) The difference between oxidation and reduction charge transfer

In the light of the observations above, we can say that following a potential pulse that occurs during the startup, a fuel cell operating at a potential of 0.7-0.8 V_{RHE} is likely to have oxides present on the catalyst surface that may affect the performance. Hence, mitigating potential spikes during the start-up of a fuel cell may not only help to reduce Pt dissolution, but could also suppress site blocking by oxide remnants.

3.4 Conclusions

Summarizing, we established a relationship between the equilibrium and transient oxidation behavior of Pt by combining in situ spectroscopy and electrochemical measurements under fuel cell-relevant conditions. We find that an oxide monolayer containing a mixture of $\text{Pt}^{6+}/\text{Pt}^{2+}/\text{Pt}^{4+}$ oxidation states is formed over a wide potential range under both equilibrium and transient conditions, contrary to the stepwise oxidation series predicted by the Pourbaix diagram. Oxidation during 5 second potential pulses, such as those occurring during the start-up and shutdown of fuel cells, results in an oxidation charge of only a ~25% less than for an equilibrated surface. This indicates that even under such transient conditions, the surface oxide structure approaches equilibrium. Further investigation of the transient pulses revealed that the oxides formed during the pulse are not fully reduced at the typical fuel cell operating potential of ~0.7 V_{RHE} . This shows that a potential pulse during fuel cell start-up will leave

Chapter 3 : A structural model for transient Pt oxidation during fuel cell start-up using electrochemical X-ray photoelectron spectroscopy

leftover oxides that potentially block some of the active sites during operation. In a more general view, our findings serve as a starting point for obtaining a mechanistic understanding of the transient phenomena that govern fuel cell degradation during start-up and shutdown.

Chapter 3 : A structural model for transient Pt oxidation during fuel cell start-up using electrochemical X-ray photoelectron spectroscopy

References

- (1) Zawodzinski, C.; Gottesfeld, S.; Materials, E.; Group, D.; Lahoralory, L. A. N.; Alamos, L. PEM Fuel Cells for Transportation and Stationary Generation Applications. *Int. Assoc. Hydrog. Energy* **1997**, 22, 1137–1144.
- (2) Yan, Q.; Toghiani, H.; Causey, H. Steady State and Dynamic Performance of Proton Exchange Membrane Fuel Cells (PEMFCs) under Various Operating Conditions and Load Changes. *J. Power Sources* **2006**, 161 (1), 492–502. <https://doi.org/10.1016/j.jpowsour.2006.03.077>.
- (3) Cieśliński, J. T.; Dawidowicz, B.; Smoleń, S. Influence of Stack Temperature on PEM Fuel Cell Performance. In *3rd International Conference, Low Temperature and Waste Heat Use in Energy Supply Systems Theory and Practice: proceedings*; Bremen, 2012; pp 39–43.
- (4) Borup, R.; Meyers, J.; Pivovar, B.; Kim, Y. S.; Mukundan, R.; Garland, N.; Myers, D.; Wilson, M.; Garzon, F.; Wood, D.; Zelenay, P.; More, K.; Stroh, K.; Zawodzinski, T.; Boncella, X. J.; Mcgrath, J. E.; Inaba, O. M.; Miyatake, K.; Hori, M.; Ota, K.; Ogumi, Z.; Miyata, S.; Nishikata, A.; Siroma, Z.; Uchimoto, Y.; Yasuda, K.; Kimijima, K.; Iwashita, N. Scientific Aspects of Polymer Electrolyte Fuel Cell Durability and Degradation. *Chem. Rev.* **2007**, 107 (10), 3904–3951. <https://doi.org/10.1021/cr050182l>.
- (5) Penga, Ž.; Radica, G.; Barbir, F.; Eckert, P. *Degradation Mechanisms in Automotive Fuel Cell Systems*; 2017.
- (6) Holby, E. F.; Morgan, D. Application of Pt Nanoparticle Dissolution and Oxidation Modeling to Understanding Degradation in PEM Fuel Cells. *J. Electrochem. Soc.* **2012**, 159 (5), B578–B591. <https://doi.org/10.1149/2.011204jes>.
- (7) Darling, R. M.; Meyers, J. P. Kinetic Model of Platinum Dissolution in PEMFCs. *J. Electrochem. Soc.* **2003**, 150 (11), A1523–A1527. <https://doi.org/10.1149/1.1613669>.
- (8) Zhang, S.; Yuan, X.; Ng, J.; Hin, C.; Wang, H.; Friedrich, K. A.; Schulze, M. A Review of Platinum-Based Catalyst Layer Degradation in Proton Exchange Membrane Fuel Cells. *J. Power Sources* **2009**, 194 (1), 588–600. <https://doi.org/10.1016/j.jpowsour.2009.06.073>.
- (9) Yeon, Y.; Cho, E.; Hyeun, J.; Lim, T.; Oh, I.; Kim, S.; Kim, H.; Hyun, J. Degradation of Polymer Electrolyte Membrane Fuel Cells Repetitively Exposed to Reverse Current Condition under Different Temperature. *J. Power Sources* **2011**, 196 (23), 9906–9915. <https://doi.org/10.1016/j.jpowsour.2011.08.035>.
- (10) Roshandel, R.; Parhizgar, T. A New Approach to Optimize the Operating Conditions of a Polymer Electrolyte Membrane Fuel Cell Based on Degradation Mechanisms. *Energy Syst.* **2013**, 4 (3), 219–237. <https://doi.org/10.1007/s12667-012-0075-8>.
- (11) Zhang, T.; Wang, P.; Chen, H.; Pei, P. A Review of Automotive Proton Exchange Membrane Fuel Cell Degradation under Start-Stop Operating Condition. *Appl. Energy* **2018**, 223 (January), 249–262. <https://doi.org/10.1016/j.apenergy.2018.04.049>.
- (12) Ā, P. P.; Chang, Q.; Tang, T. A Quick Evaluating Method for Automotive Fuel Cell Lifetime. *Int. J. Hydrogen Energy* **2008**, 33 (1), 3829–3836. <https://doi.org/10.1016/j.ijhydene.2008.04.048>.
- (13) Babu, S. K.; Spornjak, D.; Dillet, J.; Lamibrac, A.; Maranzana, G.; Didierjean, S.; Lottin, O.; Borup, R. L.; Mukundan, R. Spatially Resolved Degradation during Startup and Shutdown in Polymer Electrolyte Membrane Fuel Cell Operation. *Appl. Energy* **2019**, 254 (August), 113659. <https://doi.org/10.1016/j.apenergy.2019.113659>.

Chapter 3 : A structural model for transient Pt oxidation during fuel cell start-up using electrochemical X-ray photoelectron spectroscopy

- (14) Bruijn, F. A. De; Dam, V. A. T.; Janssen, G. J. M. Review : Durability and Degradation Issues of PEM Fuel Cell Components. *Fuel Cells* **2008**, 8 (1), 3–22. <https://doi.org/10.1002/fuce.200700053>.
- (15) Perry, M. L.; Darling, R. M.; Kandoi, S.; Patterson, T. W.; Reiser, C. Operating Requirements for Durable Polymer-Electrolyte Fuel Cell Stacks. In *Polymer Electrolyte Fuel Cell Durability*; Felix N. Büchi, Minoru Inaba, T. J. S., Ed.; Springer Science & Business Media, 2009; pp 399–415. <https://doi.org/10.1007/978-0-387-85536-3>.
- (16) Tang, H.; Qi, Z.; Ramani, M.; Elter, J. F. PEM Fuel Cell Cathode Carbon Corrosion Due to the Formation of Air / Fuel Boundary at the Anode. *J. Power Sources* **2006**, 158 (1), 1306–1312. <https://doi.org/10.1016/j.jpowsour.2005.10.059>.
- (17) Ferreira-aparicio, P.; Chaparro, A. M.; Folgado, M. A.; Conde, J. J.; Brightman, E.; Hinds, G.; Antonia, M.; Conde, J. J.; Brightman, E.; Hinds, G. Degradation Study by Start-Up/Shut-Down Cycling of Superhydrophobic Electrospayed Catalyst Layers Using a Localized Reference Electrode Technique. *ACS Appl. Mater. Interfaces* **2017**, 9 (1), 10626–10636. <https://doi.org/10.1021/acsami.6b15581>.
- (18) Rama, P.; Chen, R.; Andrews, J. A Review of Performance Degradation and Failure Modes for Hydrogen-Fuelled Polymer Electrolyte Fuel Cells. *J. Power Energy* **2008**, 222 (1), 421–441. <https://doi.org/10.1243/09576509JPE603>.
- (19) Lopes, P. P.; Tripkovic, D.; Martins, P. F. B. D. B. D.; Strmcnik, D.; Ticianelli, E. A.; Stamenkovic, V. R.; Markovic, N. M. Dynamics of Electrochemical Pt Dissolution at Atomic and Molecular Levels. *J. Electroanal. Chem.* **2017**, 819 (September), 0–1. <https://doi.org/10.1016/j.jelechem.2017.09.047>.
- (20) Mom, R.; Frevel, L.; Velasco-Vélez, J. J.; Plodinec, M.; Knop-Gericke, A.; Schlögl, R. The Oxidation of Platinum under Wet Conditions Observed by Electrochemical X-Ray Photoelectron Spectroscopy. *J. Am. Chem. Soc.* **2019**, 141 (16), 6537–6544. <https://doi.org/10.1021/jacs.8b12284>.
- (21) Yu, Y.; Tu, Z.; Zhang, H.; Zhan, Z.; Pan, M. Comparison of Degradation Behaviors for Open-Ended and Closed Proton Exchange Membrane Fuel Cells during Startup and Shutdown Cycles. *J. Power Sources* **2011**, 196 (1), 5077–5083. <https://doi.org/10.1016/j.jpowsour.2011.01.075>.
- (22) Joo, S.; Kim, S.; In, J.; Woong, C.; Lee, J.; Song, I.; Lee, N.; Kim, K.; Park, J. Lifetime Prediction of a Polymer Electrolyte Membrane Fuel Cell via an Accelerated Startup e Shutdown Cycle Test. *Int. J. Hydrogen Energy* **2012**, 37 (12), 9775–9781. <https://doi.org/10.1016/j.ijhydene.2012.03.104>.
- (23) Kim, J. H.; Jo, Y.; Cho, A.; Jang, H.; Kim, H. J.; Lim, T.; Oh, I.; Ko, J.; Jae, I. Effects of Cathode Inlet Relative Humidity on PEMFC Durability during Startup – Shutdown Cycling II . Diagnostic Study. *J. Electrochem. Soc.* **2010**, 157 (5), 633–642. <https://doi.org/10.1149/1.3327888>.
- (24) Jo, Yooyeon; Cho, Eunae; Kim, J. A Study on Performance Degradation of PEMFC by Repetitive Startup_Shutdown Cycling. *Transacitons Korean Hydrog. New Energy Soc.* **2009**, 20 (8), 318–322.
- (25) Kim, J. H.; Cho, E. A.; Jang, J. H.; Kim, H. J.; Lim, T. H.; Oh, I. H.; Ko, J. J.; Oh, S. C. Effects of Cathode Inlet Relative Humidity on PEMFC Durability during Startup–Shutdown Cycling. *J. Electrochem. Soc.* **2010**, 157 (1), B104. <https://doi.org/10.1149/1.3254170>.
- (26) Yu, Y.; Li, H.; Wang, H.; Yuan, X.; Wang, G.; Pan, M. A Review on Performance Degradation of

Chapter 3 : A structural model for transient Pt oxidation during fuel cell start-up using electrochemical X-ray photoelectron spectroscopy

- Proton Exchange Membrane Fuel Cells during Startup and Shutdown Processes : Causes , Consequences , and Mitigation Strategies. *J. Power Sources* **2012**, 205 (1), 10–23. <https://doi.org/10.1016/j.jpowsour.2012.01.059>.
- (27) Myers, D. J.; Wang, X.; Smith, M. C.; More, K. L. Potentiostatic and Potential Cycling Dissolution of Polycrystalline Platinum and Platinum Nano-Particle Fuel Cell Catalysts. *J. Electrochem. Soc.* **2018**, 165 (6), F3178–F3190. <https://doi.org/10.1149/2.0211806jes>.
- (28) Sugawara, Y.; Okayasu, T.; Yadav, A. P.; Nishikata, A.; Tsuru, T. Dissolution Mechanism of Platinum in Sulfuric Acid Solution. *J. Electrochem. Soc.* **2012**, 159 (11), F779–F786. <https://doi.org/10.1149/2.017212jes>.
- (29) Tang, L.; Li, X.; Cammarata, R. C.; Friesen, C.; Sieradzki, K. Electrochemical Stability of Elemental Metal Nanoparticles. *J. Am. Chem. Soc.* **2010**, 132 (33), 11722–11726. <https://doi.org/10.1021/ja104421t>.
- (30) Gilbert, J. A.; Kariuki, N. N.; Subbaraman, R.; Kropf, J. A.; Smith, M. C.; Holby, E. F.; Morgan, D.; Myers, D. J. In Situ Anomalous Small-Angle X-ray Scattering Studies of Platinum NP Degradation. *J. Am. Chem. Soc.* **2012**, 134 (1), 14823–14833.
- (31) Myers, D. J.; Wang, X.; Smith, M. C.; More, K. L.; Soc, J. E.; Myers, D. J.; Wang, X.; Smith, M. C.; More, K. L. Potentiostatic and Potential Cycling Dissolution of Polycrystalline Platinum and Platinum Nano-Particle Fuel Cell Catalysts. *J. Electrochem. Soc.* **2018**, 165 (6), F3178–F3190. <https://doi.org/10.1149/2.0211806jes>.
- (32) Imai, H.; Izumi, K.; Matsumoto, M.; Kubo, Y.; Kato, K.; Imai, Y. In Situ and Real-Time Monitoring of Oxide Growth in a Few Monolayers at Surfaces of Platinum Nanoparticles in Aqueous Media. *J. Am. Chem. Soc.* **2009**, 131 (17), 6293–6300. <https://doi.org/10.1021/ja810036h>.
- (33) Matsumoto, M.; Miyazaki, T.; Imai, H. Oxygen-Enhanced Dissolution of Platinum in Acidic Electrochemical Environments. *J. Phys. Chem. C* **2011**, 115 (1), 11163–11169. <https://doi.org/10.1021/jp201959h>.
- (34) Wakisaka, M.; Asizawa, S.; Watanabe, M.; Uchida, H.; Watanabe, M. In Situ STM Observation of Morphological Changes of the Pt(111) Electrode Surface during Potential Cycling in 10 MM HF Solution. *Phys. Chem. Chem. Phys.* **2010**, 12 (16), 4184–4190. <https://doi.org/10.1039/b923956a>.
- (35) Topalov, A. A.; Cherevko, S.; Zeradjanin, A. R.; Meier, J. C.; Katsounaros, I.; Mayrhofer, K. J. J. Towards a Comprehensive Understanding of Platinum Dissolution in Acidic Media. *Chem. Sci.* **2014**, 5 (2), 631–638. <https://doi.org/10.1039/c3sc52411f>.
- (36) Sasaki, K.; Marinkovic, N.; Isaacs, H. S.; Adzic, R. R. Synchrotron-Based in Situ Characterization of Carbon-Supported Platinum and Platinum Monolayer Electrocatalysts. *ACS Catal.* **2016**, 6 (1), 69–76. <https://doi.org/10.1021/acscatal.5b01862>.
- (37) Merte, L. R.; Behafarid, F.; Miller, D. J.; Friebe, D.; Cho, S.; Mbuga, F.; Sokaras, D.; Alonso-mori, R.; Weng, T. C.; Nordlund, D.; Nilsson, A.; Cuenya, B. R.; Roldan Cuenya, B. Electrochemical Oxidation of Size-Selected Pt Nanoparticles Studied Using in Situ High-Energy-Resolution X - Ray Absorption Spectroscopy. *ACS Catal.* **2012**, 2 (11), 2371–2376. <https://doi.org/10.1021/cs300494f>.
- (38) Falling, L. J.; Mom, R. V.; Diaz, L. E. S.; Nakhaie, S.; Stotz, E.; Ivanov, D.; Lunkenbein, T.; Knopgericke, A.; Schlo, R. Graphene-Capped Liquid Thin Films for Electrochemical Operando X - Ray Spectroscopy and Scanning Electron Microscopy. *ACS Appl. Mater. Interfaces* **2020**, 12 (1),

Chapter 3 : A structural model for transient Pt oxidation during fuel cell start-up using electrochemical X-ray photoelectron spectroscopy

37680–37692. <https://doi.org/10.1021/acsami.0c08379>.

- (39) Plodinec, M.; Knop-gericke, A.; Schlo, R.; Jones, T. E. In Situ X - Ray Spectroscopy of the Electrochemical Development Of. *J. Phys. Chem. C* **2019**, *123* (1), 9146–9152. <https://doi.org/10.1021/acs.jpcc.9b00731>.
- (40) Saveleva, V. A.; Papaefthimiou, V.; Daletou, M. K.; Doh, W. H.; Diebold, M.; Zafeiratos, S.; Savinova, E. R.; Ulhaq-bouillet, C.; Diebold, M.; Zafeiratos, S.; Savinova, E. R. Operando Near Ambient Pressure XPS (NAP-XPS) Study of the Pt Electrochemical Oxidation in H₂O and H₂O/O₂ Ambients. *J. Phys. Chem. C* **2016**, *120* (1), 15930–15940. <https://doi.org/10.1021/acs.jpcc.5b12410>.
- (41) Jerkiewicz, G.; Vatankhah, G.; Lessard, J.; Soriaga, M. P.; Park, Y. Surface-Oxide Growth at Platinum Electrodes in Aqueous H₂SO₄ Reexamination of Its Mechanism through Combined Cyclic-Voltammetry, Electrochemical Quartz-Crystal Nanobalance, and Auger Electron Spectroscopy Measurements. *Electrochem. Acta* **2004**, *49* (1), 1451–1459. <https://doi.org/10.1016/j.electacta.2003.11.008>.
- (42) Wang, H.; Macomber, C. S.; Dinh, H. N. Evaluation of PEMFC System Contaminants on the Performance of Pt Catalyst Via Cyclic Voltammetry. *ECS Trans.* **2013**, *50* (2), 659–669. <https://doi.org/10.1149/05002.0659ecst>.
- (43) Kumpulainen, H.; Peltonen, T.; Koponen, U.; Bergelin, M.; Valkiainen, M.; Wasberg, M. In Situ Voltammetric Characterization of PEM Fuel Cell Catalyst Layers. *VTT Tied. - Valt. Tek. Tutkimusk.* **2002**, *2137* (1), 3–28.
- (44) Sakthivel, M.; Radev, I.; Peinecke, V.; Drillet, J.-F. Highly Active and Stable Pt₃Cr/C Alloy Catalyst in H₂-PEMFC. *J. Electrochem. Soc.* **2015**, *162* (8), F901–F906. <https://doi.org/10.1149/2.0761508jes>.
- (45) Daubinger, P.; Kieninger, J.; Unmu, T.; Urban, G. A. Electrochemical Characteristics of Nanostructured Platinum Electrodes – a Cyclic Voltammetry Study. *Phys. Chem. Chem. Phys.* **2014**, *16* (18), 8392–8399. <https://doi.org/10.1039/c4cp00342j>.
- (46) Xu, H.; Song, Y.; Kunz, H. R.; Fenton, J. M. Effect of Elevated Temperature and Reduced Relative Humidity on ORR Kinetics for PEM Fuel Cells. *J. Electrochem. Soc.* **2005**, *152* (9), 1828–1836. <https://doi.org/10.1149/1.1984351>.
- (47) Ciureanu, M.; Wang, H. Electrochemical Impedance Study of Electrode – Membrane Assemblies in PEM Fuel Cells : I. Electro – Oxidation of H₂ and H₂/CO Mixtures on Pt – Based Gas – Diffusion Electrodes. *J. Electrochem. Soc.* **1999**, *146* (11), 4031–4040. <https://doi.org/10.1149/1.1392588>.
- (48) Reiser, C. A.; Bregoli, L.; Patterson, T. W.; Yi, J. S.; Yang, J. D.; Perry, M. L.; Jarvi, T. D. A Reverse-Current Decay Mechanism for Fuel Cells. *Electrochem. Solid-State Lett.* **2005**, *8* (6), 273–276. <https://doi.org/10.1149/1.1896466>.
- (49) Baumgartner, W. R.; Parz, P.; Fraser, S. D.; Walln, E.; Hacker, V. Polarization Study of a PEMFC with Four Reference Electrodes at Hydrogen Starvation Conditions. *J. Power Sources* **2008**, *182* (1), 413–421. <https://doi.org/10.1016/j.jpowsour.2008.01.001>.
- (50) Stuckey, P. A.; Zawodinski, T. A. Pulse Voltammetry: In Situ Measurements of Oxide Coverage on Platinum in Proton Exchange Membrane Fuel Cells. *ECS Trans.* **2011**, *41* (1), 651–660.
- (51) Nagai, T.; Murata, H.; Morimoto, Y. Analysis of the Relation between Oxidation State and ORR Activity of Pt by Linear Sweep Voltammetry. *ECS Trans.* **2010**, *33* (1), 125–130.

Chapter 3 : A structural model for transient Pt oxidation during fuel cell start-up using electrochemical X-ray photoelectron spectroscopy

- (52) Pourbaix, M., Zhang, H., & Pourbaix, A. *Presentation of an Atlas of Chemical and Electrochemical Equilibria in the Presence of a Gaseous Phase*; Roland Streiff, John Stringer, Richard C. Krutenat, M. C. and R. A. R., Ed.; 1997.
<https://doi.org/https://doi.org/10.4028/www.scientific.net/msf.251-254.143>.
- (53) Shard, A. G. A Straightforward Method for Interpreting XPS Data from Core-Shell Nanoparticles. *J. Phys. Chem. C* **2012**, *116* (31), 16806–16813.
<https://doi.org/10.1021/jp305267d>.
- (54) Ertl, G., Küppers, J., & Grasserbauer, M. Low Energy Electrons and Surface Chemistry. *Anal. Chim. Acta* **1987**, *199* (1), 272–273. [https://doi.org/https://doi.org/10.1016/s0003-2670\(00\)82831-7](https://doi.org/https://doi.org/10.1016/s0003-2670(00)82831-7).
- (55) Conway, B. E. Electrochemical Oxide Film Formation at Noble Metals as a Surface-Chemical Process. *Prog. Surf. Sci.* **1995**, *49* (4), 331–452. [https://doi.org/10.1016/0079-6816\(95\)00040-6](https://doi.org/10.1016/0079-6816(95)00040-6).
- (56) ANGERSTEIN-KOZLOWSKA, H.; CONWAY, B. E.; SHARP, W. B. A. THE REAL CONDITION OF ELECTROCHEMICALLY OXIDIZED PLATINUM SURFACES. *Electroanal. Chem. Interfacial Electrochem.* **1973**, *43*, 9–36. [https://doi.org/https://doi.org/10.1016/S0022-0728\(73\)80307-9](https://doi.org/https://doi.org/10.1016/S0022-0728(73)80307-9).
- (57) Ettingshausen, F.; Kleemann, J.; Marcu, A.; Toth, G.; Fuess, H.; Roth, C. Dissolution and Migration of Platinum in PEMFCs Investigated for Start / Stop Cycling and High Potential Degradation. *Fuel Cells* **2011**, *11* (2), 238–245. <https://doi.org/10.1002/fuce.201000051>.

Chapter 4

The potential-dependent structure of Pt₃Ni alloy electrocatalysts and its effect on electrocatalytic activity

Abstract

The distribution of elements within alloy nanoparticles is a critical parameter for their electrocatalytic performance. Here, we use the case of a Pt₃Ni alloy to show that this elemental distribution can dynamically respond to the applied potential, leading to strongly potential-dependent catalytic properties. Starting from the PtNi_x core and a Pt shell (formed by Pt-Ni alloys in acidic electrolyte due to Ni leaching), our electrochemical X-ray photoelectron spectroscopy measurements show that the Ni atoms can be reversibly moved between the core of the particles and the near-surface region using the applied potential. Through potential jump measurements, we show that this Ni migration modulates the hydrogen evolution reaction activity of the particles by over 30%. These observations highlight the potential of incorporating in situ restructuring of alloys as the final step in electrocatalyst design.

This Chapter has been submitted for publication:

Javed, H.; Kolmeijer, K.; Deka, N.; Sandhya, A. L. M.; Khalakhan, I.; Mom, R. V.
The Potential-Dependent Structure of Pt₃Ni Alloy Electrocatalysts and Its Effect
on Electrocatalytic Activity (*submitted*) 2025

Chapter 4 : The potential-dependent structure of Pt₃Ni alloy electrocatalysts and its effect on electrocatalytic activity

4.1 Introduction

Platinum-based alloys such as Pt₃Ni are a core component of modern fuel cells, serving as the oxygen reduction reaction (ORR) catalyst on the cathode side^{1–4}. Compared to pure Pt electrocatalysts used in older generations, these alloys show both higher activity and stability^{5–12}. Similar improvements have been observed for other reactions, such as methanol oxidation^{13,14} and hydrolytic hydrogenation¹⁵. The origin of these improvements can be attributed to strain and ligand effects in the alloys, which modulate the electronic structure of the active Pt surface atoms¹⁶. Briefly, the ligand effect^{17,18} refers to the change in the electronic structure of the Pt atoms due to the proximity of the alloying metal atoms, whereas the strain effect points to the reduction of the interatomic distance of the Pt metal atoms due to the introduction of relatively smaller transition metal (e.g. Pt: 0.139 nm, Ni:0.124 nm¹⁹) in the matrix, causing the compression of the surface atomic structure. Theoretical studies^{20–23} have shown that using the strain and ligand effects, the d-band center can be shifted to a more favorable position in alloys with respect to pure Pt. This optimizes the binding strength of the reaction intermediates on the surface and thus enhances the activity^{20–22}.

To exploit the strain and ligand effects in electrocatalyst design, it is critical to consider the evolution of the Pt-alloy structure under electrochemical conditions. For example, for Pt-Ni alloys in acidic electrolyte, the Ni atoms leach out at the surface, leading to the formation of a pure Pt skin and a Pt-alloy core^{23–25}. An inverse correlation between the ligand and strain effects and the Pt skin thickness is observed in the literature²⁶, with the compressive strain exerted on the surface Pt atoms as well as the electronic structure modification due to the ligand effect scale down with thicker Pt skins. Therefore, any enhancement due to ligand and strain effects, such as higher ORR activity, also depends inversely on the thickness of this Pt skin layer^{16,17}, making the skin layer formation properties of Pt-alloy electrocatalysts a critical design parameter^{26,27}.

Here, we hypothesized that the nature of the Pt skin layer in electrochemical systems may not only depend on the electrolyte pH, but also on the applied potential. This hypothesis is based on the alloy restructuring observed in heterogeneous catalysis, where elemental redistribution within the catalyst particles occurs depending on the adsorbates delivered from the gas phase. For example, in Pd-Rh alloys, it was shown that Rh is drawn to the surface in an oxidizing NO environment, whereas a Pd-Rh mixture is formed at the surface in a CO atmosphere²⁸. Importantly, these effects are reversible, meaning that the particle dynamically equilibrates to its environment. Similar restructuring has been observed for Pt bimetallic catalysts in gas-phase systems when the catalyst is thermally oxidized (drawing out e.g. Ni) or reduced (bringing Pt to the surface)^{23,29–31}. Here, we studied whether such reversible restructuring can also occur under electrochemical conditions, where the surface adsorbate structure is strongly dependent on the applied potential.

To observe the elemental distribution within Pt-alloy nanoparticles under electrochemical conditions, we have employed an electrochemical X-ray photoelectron spectroscopy (XPS) approach based on a graphene-covered membrane electrode assembly. Taking the example of

Chapter 4 : The potential-dependent structure of Pt₃Ni alloy electrocatalysts and its effect on electrocatalytic activity

a Pt₃Ni alloy, we demonstrate that its structure is highly dynamic under varying applied potentials, resulting in a potential-dependent catalytic activity.

4.2 Methods

i) In situ X-ray spectroscopy

To conduct the electrochemical XPS measurements, a graphene-covered membrane electrode assembly (MEA) (Figure 4.1a) was used in an in-house designed spectro-electrochemical cell. The detailed construction of the cell, as well as the MEA has been discussed in our earlier work^{32–34} and is described in detail in the supplementary information C4.1-4.6. Briefly, the MEA is made up of ~5 nm Pt₃Ni catalyst nanoparticles sputter-deposited onto a cleaned and activated Nafion membrane, and then coated with a bilayer graphene window. This graphene window is transparent for the incoming X-rays and escaping photoelectrons, permitting XPS measurements, and provides electrical contact with the catalyst. During the in situ measurements, the membrane is wetted from the back by the electrolyte (Ar-purged 0.1 M Sulfuric Acid, Sigma-Aldrich 99.9% purity). This electrolyte permeates through the proton-exchange membrane (Nafion) to the catalyst. The key function of the graphene window is to impede the evaporation of this electrolyte into the vacuum of the XPS chamber, so that XPS measurements can be conducted under wet electrochemical conditions.

To conduct the measurements, the near ambient pressure end station B-07C at Diamond Light Source, UK was utilized. The XPS signal was collected using the SPECS Phoibos NAP analyzer, whereas the total electron yield X-ray absorption spectroscopy (XAS) at the Ni L-edge was measured via the current collected on the analyzer cone. Care was taken to avoid beam damage on the Nafion membranes. Therefore, each spectrum was recorded at a new location on the MEA.

The data for XPS were processed using the CASA XPS software, and Athena was used for XAS. Details of the XPS and XAS data analysis are presented in the supplementary information C4.7.

ii) Electrochemical measurements

An Ag/AgCl reference electrode (eDAQ Leakless Miniature Ag/AgCl Reference Electrode), Pt counter electrode, and Biologic potentiostat (SP-200) were used in the XPS set-up. For reporting purposes, all the potentials mentioned in this work are converted to the RHE scale. Prior to the measurement, the potential was cycled between 0.1 V_{RHE} and 1.2 V_{RHE} at 50 mVs⁻¹ to prevent any memory effects and to aid the leaching of the unstable Ni atoms from the surface layer of the bi-metallic catalyst particles³⁵. For the chronoamperometry series, the potential was stepped between 0.1 V_{RHE} and 1.3 V_{RHE}.

Supporting glass cell measurements were conducted with a similar arrangement. However, the catalyst was deposited onto a polished glassy carbon disc (preparation described in the SI-C4.2) and measurements were conducted using a reversible hydrogen electrode (RHE) as a reference. All the measurements were done in a hanging meniscus configuration and the electrochemical data was *iR* corrected at 85%.

Chapter 4: The potential-dependent structure of Pt₃Ni alloy electrocatalysts and its effect on electrocatalytic activity

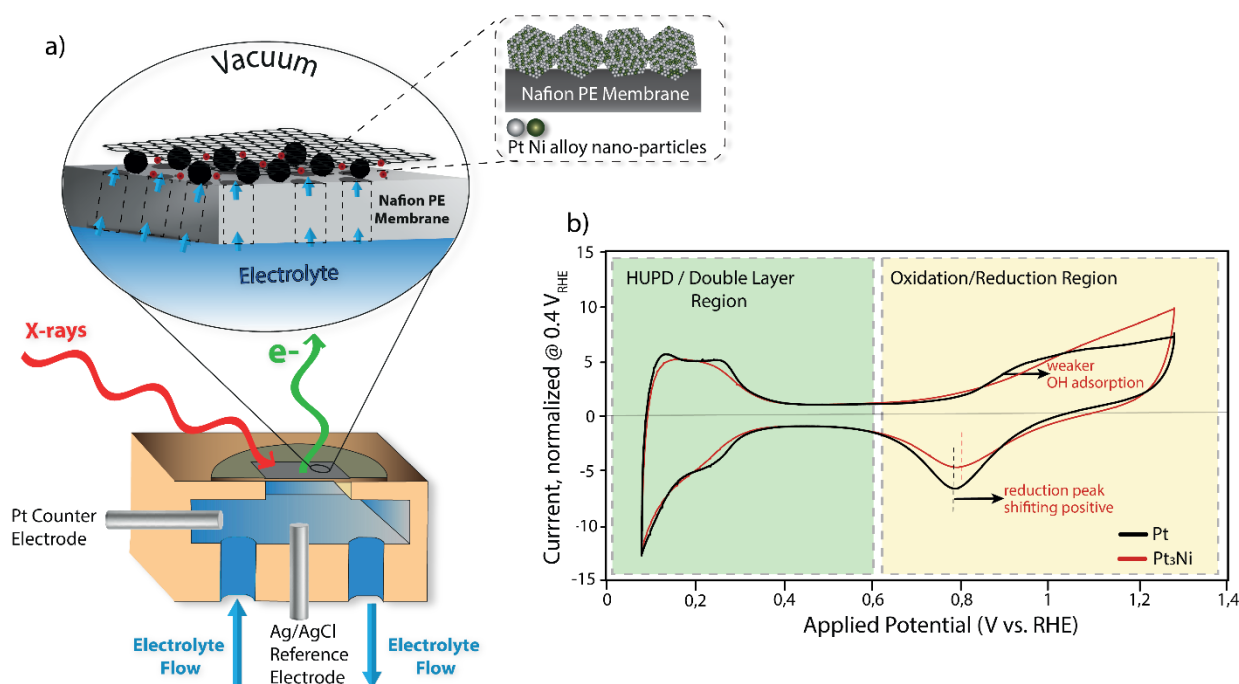


Figure 4.1: a) Cell for electrochemical XPS measurements containing an MEA consisting of the Pt₃Ni catalyst sandwiched between a Nafion membrane and a bi-layer graphene. b) Cyclic voltammograms of Pt and Pt₃Ni catalysts recorded in the XPS cell in 0.1 M H₂SO₄ at 50 mVs⁻¹, showing Hydrogen Underpotential Deposition (HUPD), Double Layer (DL) and oxidation/reduction regions

4.3 Results & Discussion

We first studied the electrochemical behavior of our Pt₃Ni catalyst. Figure 4.1b shows cyclic voltammograms (CVs) of Pt and Pt₃Ni particles recorded in the Spectro-electrochemical cell (complementary experiments in the glass cell are shown in supplementary information C4.11). The current for both curves is normalized to the double layer current at 0.4 V_{RHE} for the sake of comparison. In the oxidation region, it can be seen that the onset of oxidation, attributed to OH adsorption, is delayed for the Pt₃Ni particles compared to pure Pt, in line with the literature^{36,37}. This indicates weakened adsorbate bonding, which is considered favorable for ORR because strongly bonded adsorbates function as catalyst poison in the reaction^{41,42}. Other CV features frequently observed in the literature for Pt-Ni alloys, such as the PtO_x reduction peak shifting slightly positive^{38,39}, are also seen. Overall, these differences between Pt and Pt₃Ni highlight that Ni has a clear impact on the surface chemistry, in line with the literature^{43,44}.

Chapter 4 : The potential-dependent structure of Pt₃Ni alloy electrocatalysts and its effect on electrocatalytic activity

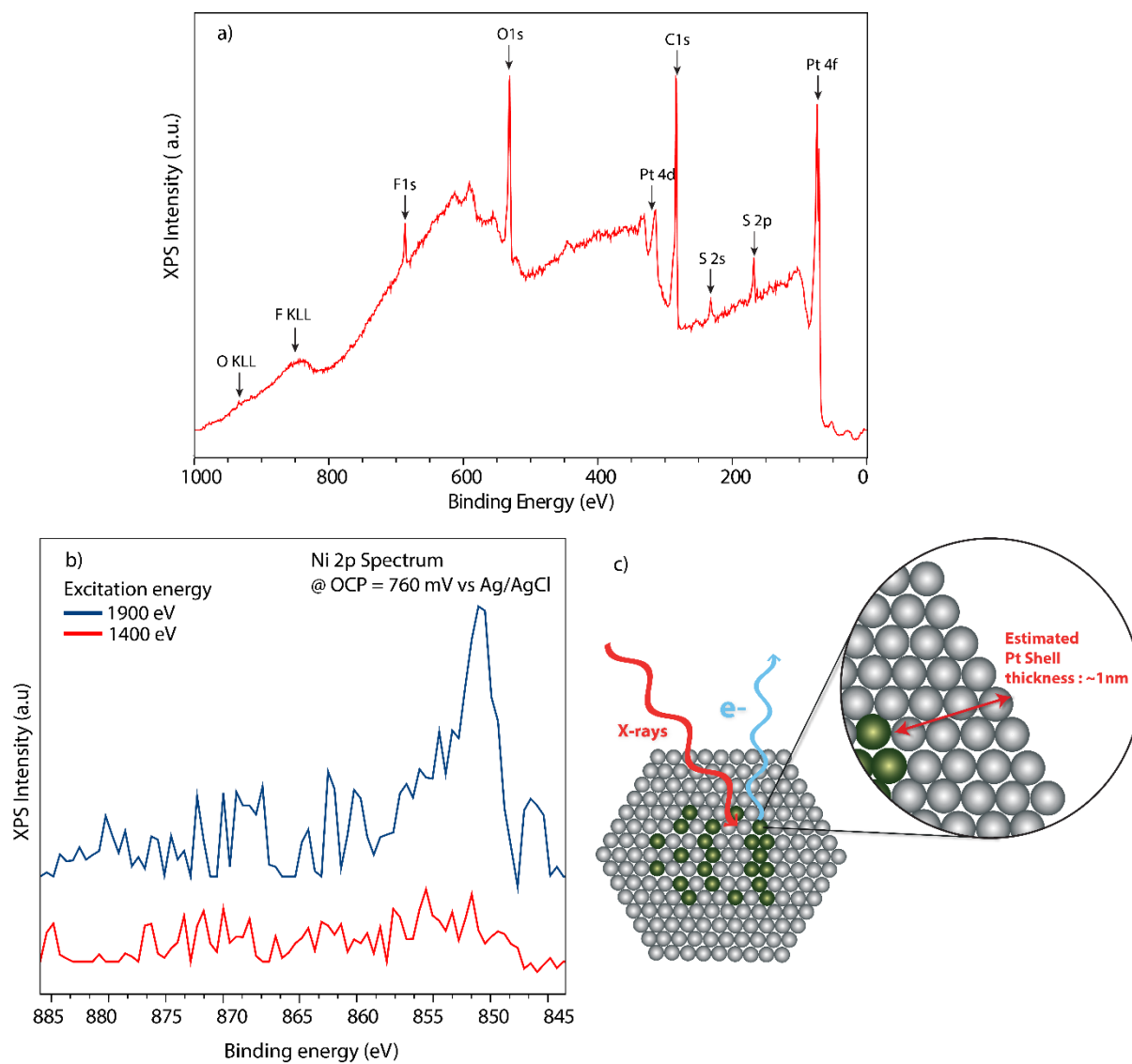


Figure 4.2 : a) Survey spectrum of OCP Pt₃Ni MEA highlighting the contributions from the membrane (S 2p, F 1s, O 1s, C 1s), graphene overlayer (C 1s), and the catalyst (Pt 4f), measured at 1400 eV, b) Ni 2p showing a noticeable Nickel contribution at a higher X-ray excitation energy (1900 eV) while almost no signal is seen at lower excitation energy (1400 eV), c) schematic impression of the in situ structure of the Pt₃Ni nanoparticles, with an ~1 nm Pt shell and mixed Pt-Ni alloy core.

As a next step, we studied the structure of the MEA and the Pt₃Ni particles using electrochemical XPS. Figure 4.2a shows a survey XPS spectrum recorded at open circuit potential (OCP, 760 mV vs. RHE) at $h\nu = 1400$ eV. The expected contributions from the Nafion membrane (S 2p, C 1s, O 1s and F 1s), the catalyst (Pt 4f), and the graphene window (C 1s) can be prominently seen. Notably, no Ni 2p contribution was observed at ~852-854 eV, indicative of the Ni leaching from the surface of the particles that is expected in acidic electrolyte^{40–44}. Such leaching leads to the formation of a core-shell structure, with a Pt shell and an alloy core⁴⁵. Indeed, Ni 2p spectra recorded at 1400 eV and 1900 eV (Figure 4.2b) show that for a higher probing depth ($h\nu = 1900$ eV), Ni is more clearly visible, consistent with a core-shell structure where the Ni resides in the core. Based on the intensity ratio of the two Ni 2p spectra

Chapter 4: The potential-dependent structure of Pt₃Ni alloy electrocatalysts and its effect on electrocatalytic activity

and the electron attenuation lengths calculated for Pt⁴⁶, the Pt shell thickness is estimated to be roughly 1 nm (Figure 4.2c). While this leached core-shell structure will contain less Ni than the initial Pt₃Ni composition, we will refer to the particles as Pt₃Ni particles for simplicity.

Following the characterization at open circuit potential, the catalyst behavior at various potentials was studied by stepping the potential down from 1.28 V_{RHE} to 0.1 V_{RHE}. In Figure 4.3, Pt 4f core levels show a steady decrease of the oxide contributions (Pt²⁺ and Pt⁴⁺) until ~0.5 V_{RHE}, in line with the reduction currents observed in the CV in Figure 4.1b. The remaining Pt^{δ+} contribution was previously also observed for pure Pt and is attributed to an adsorbate-induced peak shift of the surface atoms³².

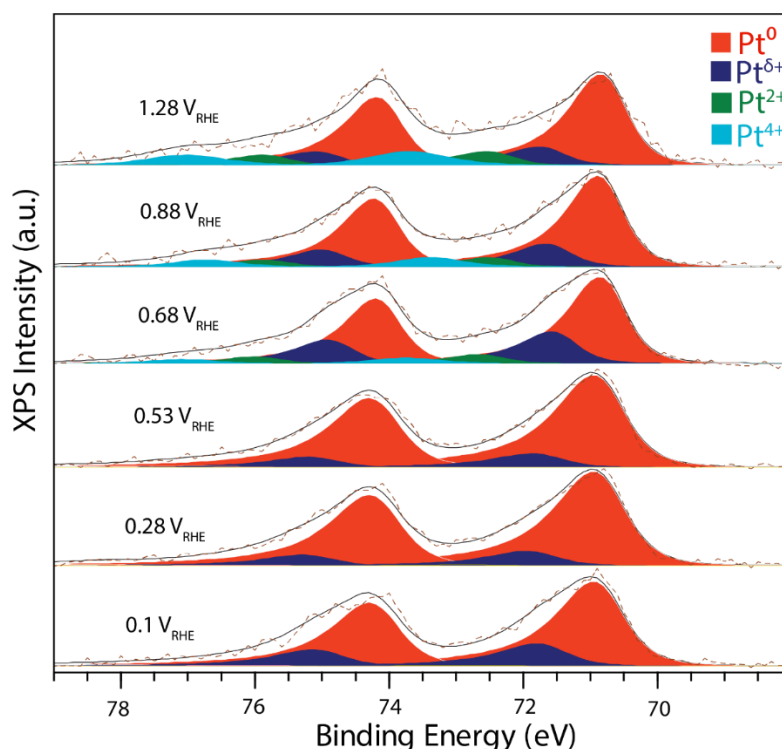


Figure 4.3: Pt 4f spectra showing the oxidation behavior of Pt in Pt₃Ni samples as a function of potential while moving from 1.28 V_{RHE} to 0.1 V_{RHE}, measured with a photon energy of 600 eV.

To track the chemistry of the Ni atoms, we recorded Ni L-edge XAS spectra within the same experiment, i.e. during the potential sequence from 1.28 V_{RHE} to 0.1 V_{RHE}. The intensity and multiplet peak pattern of the Ni L-edge are highly sensitive to the charge density of the Ni atoms, enabling the detection of even subtle changes in their electronic structure. To analyze these features, Figure 4.4 (a) displays normalized Ni L₃-edge spectra as a function of potential (normalization procedure in the supplementary information C4.10). Over the whole potential range, the spectra show a single asymmetric peak, which is typical for Ni in metal alloys^{47,48}. Importantly, no extra peaks from multiplet features⁴⁹ of Ni²⁺ or Ni³⁺ oxides are observed, showing that even when the Pt shell is oxidized, all Ni remains metallic in the core. This metallic state of the Ni is also confirmed by Ni 2p spectra (supplementary information C4.12).

Chapter 4: The potential-dependent structure of Pt₃Ni alloy electrocatalysts and its effect on electrocatalytic activity

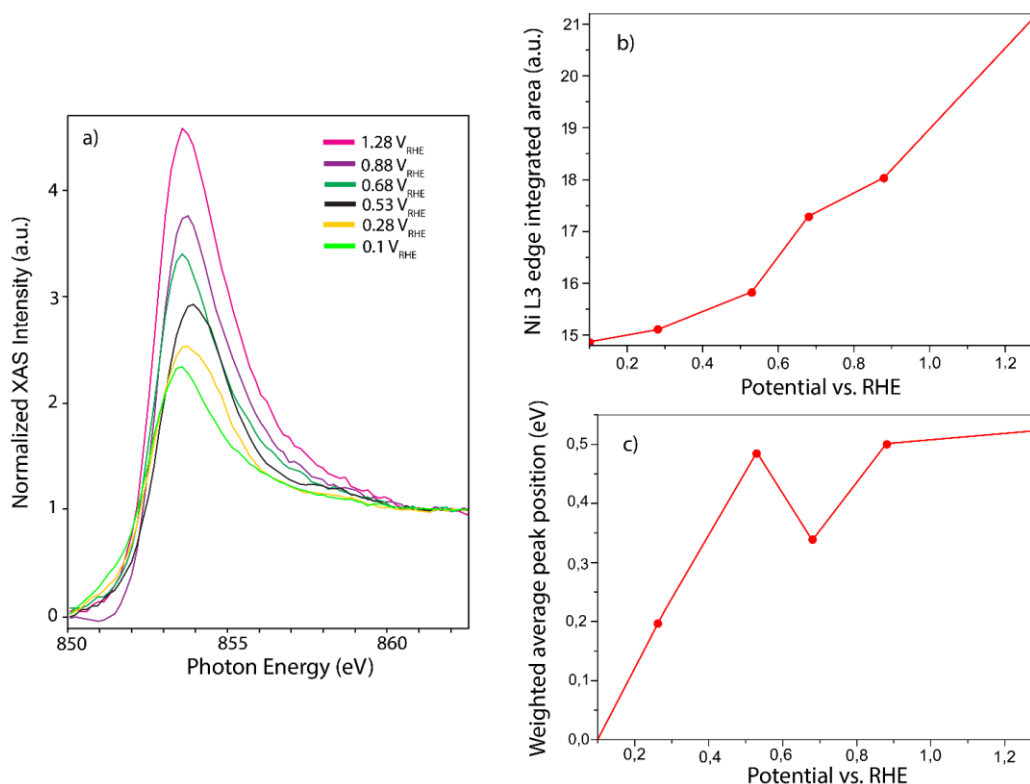


Figure 4.4: a) Ni L₃-edge spectra as a function of potential while moving from 1.28 V_{RHE} to 0.1 V_{RHE}. b) Ni L₃-edge integrated area plotted as a function of potential and c) Ni L₃-edge weighted shift in peak position plotted as a function of potential.

However, the Ni L-edge spectra do show a significant decrease in peak intensity as the potential is stepped down from 1.28 V_{RHE} to 0.1 V_{RHE}, indicating that on the more subtle level, the chemistry of the Ni atoms does change with the applied potential. Since the peak intensity in the Ni L-edge spectrum directly scales with the number of unoccupied Ni 3d states^{47,50–52}, the decreasing intensity indicates that the Ni d-band becomes more electron-rich as the potential is decreased. This can be rationalized based on the surface state of the particles: at low potential (<0.3 V_{RHE}), hydrogen atoms are adsorbed on the Pt shell, which do not draw much electron density from the nanoparticles. At intermediate potentials (0.3–0.6 V_{RHE}), sulfonate anions from the Nafion membrane and water molecules adsorb^{53–56}, which draw away slightly more electron density. Since the Ni atoms are less noble than the Pt atoms, this electron density is supplied by the Ni atoms, giving them a δ^+ state. Accordingly, a higher intensity is observed in the Ni L-edge. Above 0.6 V_{RHE}, the Pt shell is oxidized, drawing more electron density from the Ni atoms, further increasing their δ^+ character. Thus, although the Ni atoms are located in the core of the particle, they do play a role in the surface chemistry of the particles, in line with the observed Ni-induced effects in the CV (Figure 4.1b).

Figure 4.4a and c show that the peak position of the Ni L-edge is also affected by the potential-dependent chemical state of the Ni atoms. This can in part be explained by the partial oxidation of the Ni atoms to a δ^+ state: an increase Ni 3d vacancies reduces the electron-electron repulsion experienced by the Ni 2p core electrons, leading to a shift in the weighted average peak position of Ni L₃-edge to a higher energy as shown in Figure 4.4c (details of calculation of

Chapter 4: The potential-dependent structure of Pt₃Ni alloy electrocatalysts and its effect on electrocatalytic activity

the weighted average are presented in the supplementary information C4.10). However, a comparison of Figure 4.4b and c shows that there is a non-monotonous shift in the Ni L-edge peak position as well as a gradual broadening of the peak, which does not follow a consistent trend as the Ni L-edge intensity. Keeping in mind that the Ni L-edge peak position not only depends on the oxidation state, but also the coordination environment of the Ni atoms⁵⁷, this suggests that not only the charge density on the Ni atoms, but also their coordination environment changes.

To further investigate this potential-dependent restructuring of the particles, we studied the Ni 2p /Pt 4f peak area ratio (Figure 4.5, details of peak integration and ratio calculations in supplementary Information C4.8). This ratio provides an indication of the location of the Ni atoms: a low ratio indicates that the Ni atoms are located deeply in the core. Under these conditions, the Ni 2p signal is strongly attenuated due to scattering of the photoelectrons in the Pt shell, whereas the Pt 4f electrons in the shell can reach the electron analyzer essentially unhindered. If the Ni moves closer to the particle surface, this attenuation effect in the Ni 2p signal is decreased, resulting in a higher Ni 2p/Pt 4f ratio. This process is clearly observed in Figure 4.5, which shows that the Ni 2p/Pt 4f ratio markedly increases with increasing potential. This means that, as the adsorbates on the Pt₃Ni particles become increasingly electron-withdrawing at higher potentials, the Ni atoms are not only polarized to a δ^+ charge state, but also drawn closer to the surface. Note, however, that even at the highest potentials the Ni does not become part of the surface, as evidenced by the fact that the Ni atoms are not oxidized to Ni²⁺ at potentials where the Pt oxidizes. Hence, the migration of the Ni atoms is a subsurface event, as schematically depicted in Figure 4.5b. Importantly, the Ni migration is a reversible effect: it can be observed both when the potential is first held at 1.28 V_{RHE} and then stepped down to 0.1 V_{RHE} (red line in Figure 4.5a) and when the potential is held at 0.1 V_{RHE} and then stepped up to 1.28 V_{RHE} (black line in Figure 4.5a). Note that the offset between the two lines results from the fact that they were recorded using two different samples, with slight variation in catalyst structure.

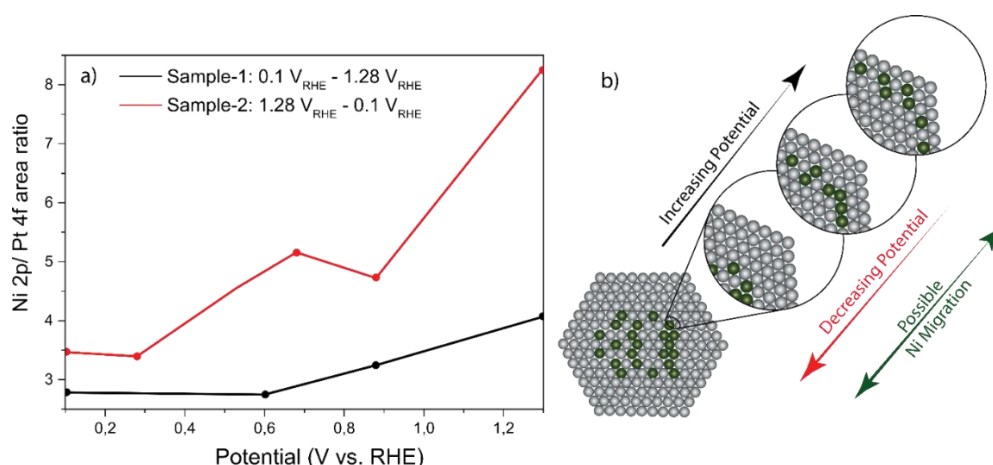


Figure 4.5: Ni location tracking via the Pt 4f/Ni 2p ratio as a function of potential and b) Pt₃Ni nanoparticle structure showing the migration of Ni towards and away from the surface as a function of potential

Chapter 4: The potential-dependent structure of Pt₃Ni alloy electrocatalysts and its effect on electrocatalytic activity

The potential-induced migration of Ni causes the thickness of the Pt shell to vary with the applied potential. As discussed in the introduction, the Pt shell thickness has an important effect on the catalytic properties of Pt-alloys^{26,27,58}. In order to probe this effect for our Pt₃Ni particles, we designed a potential step experiment where the potential was first held at either 0.3 V_{RHE} (thick Pt shell) or 0.9 V_{RHE} (thin Pt shell), followed by a switch to -0.01 V_{RHE} to measure the hydrogen evolution reaction (HER) activity of the particles. As shown in Figure 4.6, there is a marked difference between the two sequences: the HER activity following a hold at 0.9 V_{RHE} is 31% higher than after a hold at 0.3 V_{RHE}. Such a difference is not observed for pure Pt particles, confirming that the effect is caused by Ni migration. The important conclusion that can be drawn from these experiments is that the catalytic properties of Pt₃Ni electrocatalysts depend on the potential at which they are used.

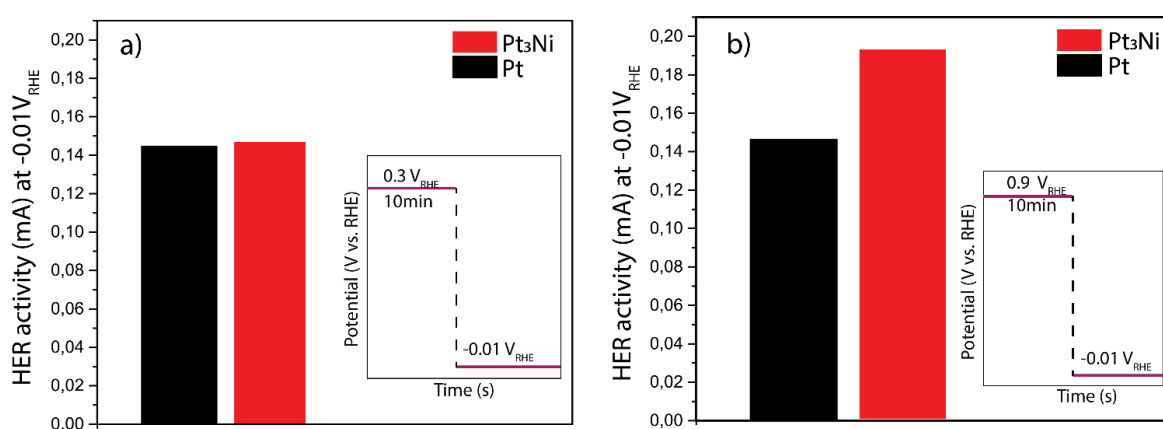


Figure 4.6: The effect of Ni migration on the hydrogen evolution reaction (HER) activity of Pt₃Ni; a) Low potential conditioning at 0.3 V_{RHE} (thick Pt shell) and b) high potential conditioning at 0.9 V_{RHE} (thin Pt shell). Pure Pt particles are shown for reference. The experiments were conducted in a glass cell in Ar-saturated 0.1 M HClO₄ with sputter-coated Pt₃Ni and Pt glassy carbon substrates. The HER current was averaged for 30 seconds after stabilization of the current to avoid (pseudo)capacitive contributions.

To obtain insight into the time scale of the Ni migration, the potential step experiment was repeated with different conditioning times at 0.9 V_{RHE}. As can be seen in Figure 4.7, the enhancement of the HER current stabilizes at a conditioning time of about 10 minutes. This indicates that the Ni atoms are able to move over several atomic spaces in a matter of minutes to find their equilibrium configuration at 0.9 V_{RHE}. Considering that the experiments were carried out at room temperature, this is a remarkable rate. It may therefore be hypothesized that Ni diffusion is accelerated by the adsorption-induced charge transfer from the Ni to the adsorbates, analogous to the Cabrera-Mott mechanism for metal oxide formation⁵⁹.

Chapter 4 : The potential-dependent structure of Pt₃Ni alloy electrocatalysts and its effect on electrocatalytic activity

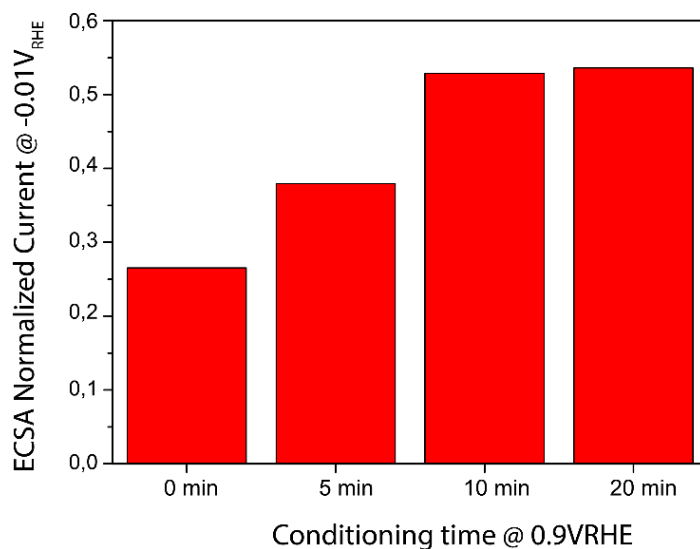


Figure 4.7: Effect of high potential ($0.9 V_{RHE}$) conditioning time on HER activity. The HER current here was averaged over 30 seconds and has been normalized to the case without the high potential conditioning step, to highlight the relative effect of high potential conditioning on Ni migration and the timescale on which it occurs.

Chapter 4 : The potential-dependent structure of Pt₃Ni alloy electrocatalysts and its effect on electrocatalytic activity

4.4 Conclusions

In conclusion, we have shown that the structure and catalytic properties of Pt₃Ni nanoparticles are dependent on the applied potential. The restructuring of the particles is subtle: a PtNi_x core – Pt shell structure is maintained over the entire potential range, but the thickness of the Pt shell varies due to Ni migration. Nonetheless, this restructuring has marked effect on the catalytic properties of the particles, as probed through the hydrogen evolution reaction. The driving force for the Ni migration is the interaction between the Ni atoms in the core and the adsorbates on the particle surface, which involves charge transfer from Ni to the surface. This interaction is strong enough to facilitate Ni migration on the time scale of minutes. Importantly, the adsorbate-interaction driven alloy restructuring uncovered here is a very general mechanism, that one may anticipate to occur for other alloys as well. Therefore, we expect that in situ restructuring of alloys is an important factor to consider in the design of bimetallic electrocatalysts with optimal binding properties.

Chapter 4 : The potential-dependent structure of Pt₃Ni alloy electrocatalysts and its effect on electrocatalytic activity

References

- (1) Colón-Mercado, H. R.; Popov, B. N. Stability of Platinum Based Alloy Cathode Catalysts in PEM Fuel Cells. *J Power Sources* **2006**, *155* (2), 253–263. <https://doi.org/10.1016/j.jpowsour.2005.05.011>.
- (2) Gu, J.; Zhang, G. M.; Yao, R.; Yu, T.; Han, M. F.; Huang, R. S. High Oxygen Reduction Activity of Pt-Ni Alloy Catalyst for Proton Exchange Membrane Fuel Cells. *Catalysts* **2022**, *12* (3). <https://doi.org/10.3390/catal12030250>.
- (3) Xu, W. C.; Zhang, Z. M.; Yang, C. H.; Zhao, K. M.; Wang, Y.; Tian, N.; Zhou, Z. Y.; Sun, S. G. Promotion Mechanism of PtCo Intermetallic Ordered Alloys in Oxygen Reduction Reaction and Its Application in Fuel Cells. *Electrochem commun* **2023**, *152*. <https://doi.org/10.1016/j.elecom.2023.107516>.
- (4) Kozhokar, E.; Pavlets, A.; Pankov, I.; Alekseenko, A. Platinum–Nickel Electrocatalysts for a Proton-Exchange Membrane Fuel Cell Cathode: Their Synthesis, Acid Treatment, Microstructure and Electrochemical Behavior. *Energies (Basel)* **2023**, *16* (16). <https://doi.org/10.3390/en16166078>.
- (5) Yu, W.; Porosoff, M. D.; Chen, J. G. Review of Pt-Based Bimetallic Catalysis: From Model Surfaces to Supported Catalysts. *ChemInform* **2013**, *44* (6). <https://doi.org/10.1002/chin.201306180>.
- (6) Lonergan, W. W.; Vlachos, D. G.; Chen, J. G. Correlating Extent of Pt-Ni Bond Formation with Low-Temperature Hydrogenation of Benzene and 1,3-Butadiene over Supported Pt/Ni Bimetallic Catalysts. *J Catal* **2010**, *271* (2), 239–250. <https://doi.org/10.1016/j.jcat.2010.01.019>.
- (7) Wang, J.; Li, B.; Yang, D.; Lv, H.; Zhang, C. Preparation Optimization and Single Cell Application of PtNi/C Octahedral Catalyst with Enhanced ORR Performance. *Electrochim Acta* **2018**, *288*, 126–133. <https://doi.org/10.1016/j.electacta.2018.09.005>.
- (8) Begum, M.; Yurukcu, M.; Yurtsever, F.; Ergul, B.; Kariuki, N.; Myers, D. J.; Karabacak, T. Pt-Ni/WC Alloy Nanorods Arrays as ORR Catalyst for PEM Fuel Cells. *ECS Trans* **2017**, *80* (8), 919–925. <https://doi.org/10.1149/08008.0919ecst>.
- (9) Wang, Q.; Mi, B.; Zhou, J.; Qin, Z.; Chen, Z.; Wang, H. Hollow-Structure Pt-Ni Nanoparticle Electrocatalysts for Oxygen Reduction Reaction. *Molecules* **2022**, *27* (8). <https://doi.org/10.3390/molecules27082524>.
- (10) Ye, S. H.; Feng, J. X.; Wang, A. L.; Xu, H.; Li, G. R. Multi-Layered Pt/Ni Nanotube Arrays with Enhanced Catalytic Performance for Methanol Electrooxidation. *J Mater Chem A Mater* **2015**, *3* (46), 23201–23206. <https://doi.org/10.1039/c5ta07098h>.
- (11) Navarro, R. M.; Pawelec, B.; Trejo, J. M.; Mariscal, R.; Fierro, J. L. G. *Hydrogenation of Aromatics on Sulfur-Resistant PtPd Bimetallic Catalysts*; 2000; Vol. 189. <http://www.idealibrary.comon>.
- (12) Jia, Q.; Lewis, A.; Grice, C.; Smotkin, S.; Segre, U. In Situ XAFS Studies of the Oxygen Reduction Reaction on Carbon Supported Pt and PtNi(1:1) Catalysts. *J Phys Conf Ser* **2009**, *190*. <https://doi.org/10.1088/1742-6596/190/1/012157>.
- (13) Zhou, Y. Y.; Liu, C. H.; Liu, J.; Cai, X. L.; Lu, Y.; Zhang, H.; Sun, X. H.; Wang, S. D. Self-Decoration of PtNi Alloy Nanoparticles on Multiwalled Carbon Nanotubes for Highly Efficient Methanol Electro-Oxidation. *Nanomicro Lett* **2016**, *8* (4), 371–380. <https://doi.org/10.1007/s40820-016-0096-2>.

Chapter 4 : The potential-dependent structure of Pt₃Ni alloy electrocatalysts and its effect on electrocatalytic activity

- (14) Qiu, H.; Zou, F. Nanoporous PtCo Surface Alloy Architecture with Enhanced Properties for Methanol Electrooxidation. *ACS Appl Mater Interfaces* **2012**, 4 (3), 1404–1410.
<https://doi.org/10.1021/am201659n>.
- (15) Liang, G.; He, L.; Arai, M.; Zhao, F. The Pt-Enriched PtNi Alloy Surface and Its Excellent Catalytic Performance in Hydrolytic Hydrogenation of Cellulose. *ChemSusChem* **2014**, 7 (5), 1415–1421.
<https://doi.org/10.1002/cssc.201301204>.
- (16) Shao, M.; Odell, J. H.; Peles, A.; Su, D. The Role of Transition Metals in the Catalytic Activity of Pt Alloys: Quantification of Strain and Ligand Effects. *Chemical Communications* **2014**, 50 (17), 2173–2176. <https://doi.org/10.1039/c3cc47341d>.
- (17) Adzic, R. R.; Zhang, J.; Sasaki, K.; Vukmirovic, M. B.; Shao, M.; Wang, J. X.; Nilekar, A. U.; Mavrikakis, M.; Valerio, J. A.; Uribe, F. Platinum Monolayer Fuel Cell Electrocatalysts. *Top Catal* **2007**, 46 (3–4), 249–262. <https://doi.org/10.1007/s11244-007-9003-x>.
- (18) Hammer, B.; Nørskov, J. K. Theoretical Surface Science and Catalysis-Calculations and Concepts; 2000; Vol. 45, pp 71–128.
- (19) Callister, W. D.; David Rethwisch, J. G. *MATERIALS SCIENCE and ENGINEERING*, 9th Edition.; Sayre, D.; Wiley, pp 691–699.
- (20) Stamenkovic, V. R.; Strmcnik, D.; Lopes, P. P.; Markovic, N. M. Energy and Fuels from Electrochemical Interfaces. *Nature Materials*. Nature Publishing Group December 20, 2016, pp 57–69.
<https://doi.org/10.1038/nmat4738>.
- (21) Stephens, I. E. L.; Bondarenko, A. S.; Perez-Alonso, F. J.; Calle-Vallejo, F.; Bech, L.; Johansson, T. P.; Jepsen, A. K.; Frydendal, R.; Knudsen, B. P.; Rossmeisl, J.; Chorkendorff, I. Tuning the Activity of Pt(111) for Oxygen Electroreduction by Subsurface Alloying. *J Am Chem Soc* **2011**, 133 (14), 5485–5491. <https://doi.org/10.1021/ja111690g>.
- (22) Stamenkovic, V. R.; Mun, B. S.; Mayrhofer, K. J. J.; Ross, P. N.; Markovic, N. M. Effect of Surface Composition on Electronic Structure, Stability, and Electrocatalytic Properties of Pt-Transition Metal Alloys: Pt-Skin versus Pt-Skeleton Surfaces. *J Am Chem Soc* **2006**, 128 (27), 8813–8819.
<https://doi.org/10.1021/ja0600476>.
- (23) Lim, C.; Fairhurst, A. R.; Ransom, B. J.; Haering, D.; Stamenkovic, V. R. Role of Transition Metals in Pt Alloy Catalysts for the Oxygen Reduction Reaction. *ACS Catalysis*. American Chemical Society November 17, 2023, pp 14874–14893. <https://doi.org/10.1021/acscatal.3c03321>.
- (24) Stamenkovic, V. R.; Mun, B. S.; Arenz, M.; Mayrhofer, K. J. J.; Lucas, C. A.; Wang, G.; Ross, P. N.; Markovic, N. M. Trends in Electrocatalysis on Extended and Nanoscale Pt-Bimetallic Alloy Surfaces. *Nat Mater* **2007**, 6 (3), 241–247. <https://doi.org/10.1038/nmat1840>.
- (25) Bogar, M.; Yakovlev, Y.; Sandbeck, D. J. S.; Cherevko, S.; Matolínová, I.; Amenitsch, H.; Khalakhan, I. Interplay among Dealloying, Ostwald Ripening, and Coalescence in PtXNi100-XBimetallic Alloys under Fuel-Cell-Related Conditions. *ACS Catal* **2021**, 11 (18), 11360–11370.
<https://doi.org/10.1021/acscatal.1c01111>.
- (26) Morris, A. R.; Skoglund, M. D.; Holles, J. H. Characterization of Ni@Pt and Co@Pt Overlayer Catalysts Using XAS Studies. *Appl Catal A Gen* **2015**, 489, 98–110.
<https://doi.org/10.1016/j.apcata.2014.10.019>.

Chapter 4: The potential-dependent structure of Pt₃Ni alloy electrocatalysts and its effect on electrocatalytic activity

- (27) Schlapka, A.; Lischka, M.; Groß, A.; Käsberger, U.; Jakob, P. Surface Strain versus Substrate Interaction in Heteroepitaxial Metal Layers: Pt on Ru(0001). *Phys Rev Lett* **2003**, *91* (1), 016101/1-016101/4. <https://doi.org/10.1103/PhysRevLett.91.016101>.
- (28) Tao, F.; Grass, M. E.; Zhang, Y.; Butcher, D. R.; Aksoy, F.; Aloni, S.; Altoe, V.; Alayoglu, S.; Renzas, J. R.; Tsung, C. K.; Zhu, Z.; Liu, Z.; Salmeron, M.; Somorjai, G. A. Evolution of Structure and Chemistry of Bimetallic Nanoparticle Catalysts under Reaction Conditions. *J Am Chem Soc* **2010**, *132* (25), 8697–8703. <https://doi.org/10.1021/ja101502t>.
- (29) Khalakhan, I.; Bogar, M.; Vorokhta, M.; Kúš, P.; Yakovlev, Y.; Dopita, M.; Sandbeck, D. J. S.; Cherevko, S.; Matolínová, I.; Amenitsch, H. Evolution of the PtNi Bimetallic Alloy Fuel Cell Catalyst under Simulated Operational Conditions. *ACS Appl Mater Interfaces* **2020**, *12* (15), 17602–17610. <https://doi.org/10.1021/acsami.0c02083>.
- (30) Xie, X.; Sandhya, A. L. M.; Piliat, L.; Vorokhta, M.; Matolínová, I.; Khalakhan, I. Surface Compositional Dynamics in a PtNi Bimetallic Alloy under Simulated Operational Conditions: Electrochemical and NAP-XPS Study. *Appl Catal B* **2023**, *325*. <https://doi.org/10.1016/j.apcatb.2022.122328>.
- (31) Ruban, A. V.; Skriver, H. L.; Nørskov, J. K. Surface Segregation Energies in Transition-Metal Alloys. *Phys Rev B Condens Matter Mater Phys* **1999**, *59* (24), 15990–16000. <https://doi.org/10.1103/PhysRevB.59.15990>.
- (32) Javed, H.; Knop-Gericke, A.; Mom, R. V. Structural Model for Transient Pt Oxidation during Fuel Cell Start-up Using Electrochemical X-Ray Photoelectron Spectroscopy. *ACS Appl Mater Interfaces* **2022**, *14* (31), 36238–36245. <https://doi.org/10.1021/acsami.2c09249>.
- (33) Mom, R.; Frevel, L.; Velasco-Vélez, J. J.; Plodinec, M.; Knop-Gericke, A.; Schlögl, R. The Oxidation of Platinum under Wet Conditions Observed by Electrochemical X-Ray Photoelectron Spectroscopy. *J Am Chem Soc* **2019**, *141* (16), 6537–6544. <https://doi.org/10.1021/jacs.8b12284>.
- (34) Frevel, L. J.; Mom, R.; Velasco-Vélez, J. J.; Plodinec, M.; Knop-Gericke, A.; Schlögl, R.; Jones, T. E. In Situ X-Ray Spectroscopy of the Electrochemical Development of Iridium Nanoparticles in Confined Electrolyte. *Journal of Physical Chemistry C* **2019**, *123* (14), 9146–9152. <https://doi.org/10.1021/acs.jpcc.9b00731>.
- (35) Glösen, A.; Dionigi, F.; Paciok, P.; Heggen, M.; Müller, M.; Gan, L.; Strasser, P.; Dunin-Borkowski, R. E.; Stolten, D. Dealloyed PtNi-Core-Shell Nanocatalysts Enable Significant Lowering of Pt Electrode Content in Direct Methanol Fuel Cells. *ACS Catal* **2019**, *9* (5), 3764–3772. <https://doi.org/10.1021/acscatal.8b04883>.
- (36) Matanovic, I.; Garzon, F. H.; Henson, N. J. Theoretical Study of Electrochemical Processes on Novel Platinum Group Metal Catalysts. *ACS National Meeting Book of Abstracts* **2011**, 10640–10650. <https://doi.org/10.1149/ma2011-02/16/1004>.
- (37) Wang, J.; Li, B.; Yang, D.; Lv, H.; Zhang, C. Preparation Optimization and Single Cell Application of PtNi/C Octahedral Catalyst with Enhanced ORR Performance. *Electrochim Acta* **2018**, *288*, 126–133. <https://doi.org/10.1016/j.electacta.2018.09.005>.
- (38) Stamenković, V.; Schmidt, T. J.; Ross, P. N.; Marković, N. M. Surface Segregation Effects in Electrocatalysis: Kinetics of Oxygen Reduction Reaction on Polycrystalline Pt₃Ni Alloy Surfaces. *Journal of Electroanalytical Chemistry* **2003**, *554–555* (1), 191–199. [https://doi.org/10.1016/S0022-0728\(03\)00177-3](https://doi.org/10.1016/S0022-0728(03)00177-3).

Chapter 4: The potential-dependent structure of Pt₃Ni alloy electrocatalysts and its effect on electrocatalytic activity

- (39) Bunch, J. S.; Van Der Zande, A. M.; Verbridge, S. S.; Frank, I. W.; Tanenbaum, D. M.; Parpia, J. M.; Craighead, H. G.; McEuen, P. L. Improved Oxygen Reduction Activity on Pt₃Ni(111) via Increased Surface Site Availability. *Science* (1979) **2007**, 315 (5811), 490–493. <https://doi.org/10.1126/science.1136836>.
- (40) Wang, C.; Van Der Vliet, D.; Chang, K. C.; You, H.; Strmcnik, D.; Schlueter, J. A.; Markovic, N. M.; Stamenkovic, V. R. Monodisperse Pt₃Co Nanoparticles as a Catalyst for the Oxygen Reduction Reaction: Size-Dependent Activity. *Journal of Physical Chemistry C* **2009**, 113 (45), 19365–19368. <https://doi.org/10.1021/jp908203p>.
- (41) Patrick, B.; Ham, H. C.; Shao-Horn, Y.; Allard, L. F.; Hwang, G. S.; Ferreira, P. J. Atomic Structure and Composition of “Pt₃Co” Nanocatalysts in Fuel Cells: An Aberration-Corrected STEM HAADF Study. *Chemistry of Materials* **2013**, 25 (4), 530–535. <https://doi.org/10.1021/cm3029164>.
- (42) Mukerjee, S.; Srinivasan, S. *Enhanced Electrocatalysis of Oxygen Reduction on Platinum Alloys in Proton Exchange Membrane Fuel Cells*; Elsevier Sequoia S.A, 1993; Vol. 357.
- (43) Huang, Y.; Zhang, J.; Kongkanand, A.; Wagner, F. T.; Li, J. C. M.; Jorné, J. Transient Platinum Oxide Formation and Oxygen Reduction on Carbon-Supported Platinum and Platinum-Cobalt Alloy Electrocatalysts. *J Electrochem Soc* **2014**, 161 (1), F10–F15. <https://doi.org/10.1149/2.018401jes>.
- (44) Zhang, K.; Yue, Q.; Chen, G.; Zhai, Y.; Wang, L.; Wang, H.; Zhao, J.; Liu, J.; Jia, J.; Li, H. Effects of Acid Treatment of Pt-Ni Alloy Nanoparticles@graphene on the Kinetics of the Oxygen Reduction Reaction in Acidic and Alkaline Solutions. *Journal of Physical Chemistry C* **2011**, 115 (2), 379–389. <https://doi.org/10.1021/jp108305v>.
- (45) Markovic, N.; Browning, A.; Stamenkovic, V.; Roy, J.; Grunder, Y.; Thompson, P.; Fowler, B.; Lucas, C. From Ultra-High Vacuum to the Electrochemical Interface: X-Ray Scattering Studies of Model Electrocatalysts. *Faraday Discussions*. 2008, pp 9–10. <https://doi.org/10.1039/b814058h>.
- (46) Cumpson, P. J.; Seah, M. P. Elastic Scattering Corrections in AES and XPS. II. Estimating Attenuation Lengths and Conditions Required for Their Valid Use in Overlayer/Substrate Experiments. *Surface and Interface Analysis* **1997**, 25 (6), 430–446. [https://doi.org/10.1002/\(SICI\)1096-9918\(199706\)25:6<430::AID-SIA254>3.0.CO;2-7](https://doi.org/10.1002/(SICI)1096-9918(199706)25:6<430::AID-SIA254>3.0.CO;2-7).
- (47) Chang, Y. K.; Lin, K. P.; Pong, W. F.; Tsai, M. H.; Hsieh, H. H.; Pieh, J. Y.; Tseng, P. K.; Lee, J. F.; Hsu, L. S. Charge Transfer and Hybridization Effects in Ni₃Al and Ni₃Ga Studies by X-Ray-Absorption Spectroscopy and Theoretical Calculations. *J Appl Phys* **2000**, 87 (3), 1312–1317. <https://doi.org/10.1063/1.372015>.
- (48) Van Der Laan, G.; Thole, B. T.; Sawatzky, G. A.; Verdaguer, M. *Multiplet Structure in the L_{2,3} x-Ray-Absorption Spectra: A Fingerprint for High-and Low-Spin Ni Compounds*; Vol. 37.
- (49) Regan, T. J.; Ohldag, H.; Stamm, C.; Nolting, F.; Lüning, J.; Stöhr, J.; White, R. L. Chemical Effects at Metal/Oxide Interfaces Studied by x-Ray-Absorption Spectroscopy. *Phys Rev B Condens Matter Mater Phys* **2001**, 64 (21). <https://doi.org/10.1103/PhysRevB.64.214422>.
- (50) Kasatkov, S.; Fantin, A.; Manzoni, A. M.; Sakhonenkov, S.; Makarova, A.; Smirnov, D.; Filatova, E. O.; Schumacher, G. *Chemical Interaction and Electronic Structure in a Compositionally Complex Alloy: A Case Study by Means of X-Ray Absorption and X-Ray Photoelectron Spectroscopy*.

Chapter 4 : The potential-dependent structure of Pt₃Ni alloy electrocatalysts and its effect on electrocatalytic activity

- (51) Hsieh, H. H.; Chang, Y. K.; Pong, W. F.; Pieh, J. Y.; Tseng, P. K.; Sham, T. K.; Coulthard, I.; Naftel, S. J.; Lee, J. F.; Chung, S. C.; Tsang, K. L. *Electronic Structure of Ni-Cu Alloys: The d-Electron Charge Distribution*; 1998.
- (52) Mukerjee, S.; Srinivasan, S.; Soriaga, M. P. Role of Structural and Electronic Properties of Pt and Pt Alloys on Electrocatalysis of Oxygen Reduction: An In Situ XANES and EXAFS Investigation. *J. Electrochem. Soc* **1995**, *142*, 1409.
- (53) Su, Z.; Climent, V.; Leitch, J.; Zamlynny, V.; Feliu, J. M.; Lipkowski, J. Quantitative SNIPTIRS Studies of (Bi)Sulfate Adsorption at the Pt(111) Electrode Surface. *Physical Chemistry Chemical Physics* **2010**, *12* (46), 15231–15239. <https://doi.org/10.1039/c0cp00860e>.
- (54) Kolics, A.; Wieckowski, A. Adsorption of Bisulfate and Sulfate Anions on a Pt(111) Electrode. *Journal of Physical Chemistry B* **2001**, *105* (13), 2588–2595. <https://doi.org/10.1021/jp003536f>.
- (55) Teliska, M.; Murthi, V. S.; Mukerjee, S.; Ramaker, D. E. Site-Specific vs Specific Adsorption of Anions on Pt and Pt-Based Alloys. *Journal of Physical Chemistry C* **2007**, *111* (26), 9267–9274. <https://doi.org/10.1021/jp071106k>.
- (56) Yano, H.; Uematsu, T.; Omura, J.; Watanabe, M.; Uchida, H. Effect of Adsorption of Sulfate Anions on the Activities for Oxygen Reduction Reaction on Nafion®-Coated Pt/Carbon Black Catalysts at Practical Temperatures. *Journal of Electroanalytical Chemistry* **2015**, *747*, 91–96. <https://doi.org/10.1016/j.jelechem.2015.04.007>.
- (57) Chen, J.; Finrock, Y. Z.; Wang, Z.; Sham, T. K. Strain and Ligand Effects in Pt-Ni Alloys Studied by Valence-to-Core X-Ray Emission Spectroscopy. *Sci Rep* **2021**, *11* (1). <https://doi.org/10.1038/s41598-021-93068-0>.
- (58) Strasser, P.; Koh, S.; Anniyev, T.; Greeley, J.; More, K.; Yu, C.; Liu, Z.; Kaya, S.; Nordlund, D.; Ogasawara, H.; Toney, M. F.; Nilsson, A. Lattice-Strain Control of the Activity in Dealloyed Core-Shell Fuel Cell Catalysts. *Nat Chem* **2010**, *2* (6), 454–460. <https://doi.org/10.1038/nchem.623>.
- (59) Cabrera, N.; Mott, N. F. Theory of the Oxidation of Metals. *Reports on Progress in Physics* **1949**, *12* (1), 163–184. <https://doi.org/10.1088/0034-4885/12/1/308>.

A Supplementary Information for Chapter 2

A Supplementary Information on Chapter 2

A2.1 Manipulator and Load lock Design

The manipulator design was made with three scenarios in mind: i) Ex-situ investigation of solid state samples in vacuum, ii) In situ investigation of electrochemical reactions and iii) In situ investigation of gas-solid reactions and interfaces at higher temperatures (under development). The first two scenarios are addressed using interchangeable extensions that can be fitted on the same manipulator platform, circumventing the need to design and construct separate manipulators for each purpose and thus greatly reducing the complexity of the setup. The primary application of the set-up is electrochemistry including fundamental studies on the electric double layer structure in electrochemical systems and effects of different ions in electrochemical reactions¹, cathodic corrosion of precious metal catalysts², and more applied research areas such as fuel cell degradation, energy storage and battery systems³, all of which require very different experimental conditions.

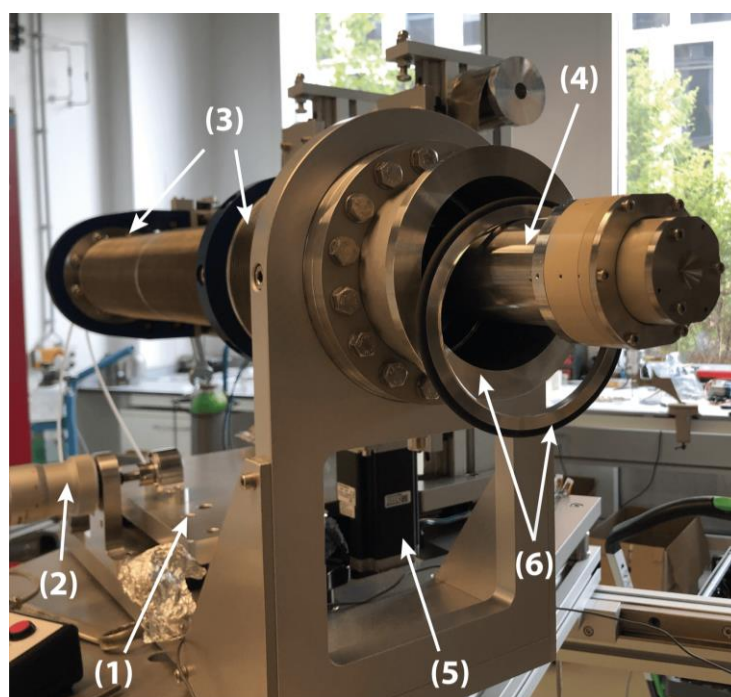


Figure A2.1 : External overview of manipulator assembly and the electrochemical cell and the manipulator shows the state before the cell is placed in the system. The axial movement of the cell is managed by an electronic drive unit for precise position, while the horizontal and vertical positions can be adjusted by micrometer screws

Figure A2.1 shows the manipulator assembly, where the manipulator is mounted on a rotation table (1) which is capable of rotating 45° to allow convenient sample exchange. The assembly is also fitted with micrometer screws to manually adjust the positioning of the sample in the X,Y and Z planes (2). The manipulator (3) consists of two annular tubes; the outer tube consists of two sections of expandable bellows supported by the manipulator manifold on which it is mounted, while the inner tube is a standard 316L stainless steel tube on which the electrochemical cell is mounted. The electrolyte supply lines, safety valves and potentiostat

A Supplementary Information on Chapter 2

wires connected to the cell run through the inside of the tube which is not part of the vacuum, so that standard components used in electrochemical labs can be employed without risk of vacuum contamination. The manipulator is fitted with step motors (5) and operated by an electronic console to move/ retract the sample into/out of the main chamber. The manipulator is connected to the sample preparation chamber (load lock) via an ISO flange (6), which can be opened quickly to facilitate rapid sample exchange. Once the sample is secured inside the load lock, it is pumped down via a scroll pump to $\sim 10^{-2}$ mbar before introducing the cell into the main chamber.

A2.2 Main Chamber

The main chamber of the setup is a spherical chamber made of 316L Austenitic stainless steel and is connected to the load lock via a gate valve (VAT Vakuumventile AG). This gate valve isolates the main chamber from the load lock during sample exchange and leak testing of the electrochemical cell. The chamber has a central window for a clear view and maintenance access. Figure 2.1 in the main text also shows a UHV chamber connected to the main chamber and is pumped by a large turbomolecular pump (Pfeiffer Vacuum HiPace 700). The UHV chamber is separated from the main chamber by a pneumatically operated butterfly valve (VAT Vakuumventile AG) which is kept open during the ex-situ measurements to maintain a lower pressure in the main chamber and kept closed during NAP-XPS measurements. The main chamber is fitted with two capacitive pressure gauges to cover the pressure range from ambient pressure up to 10^{-5} mbar. In order to shield the samples from the stray magnetic fields due to the electrical equipment around the setup, 3 pairs of Helmholtz coils are installed around the main chamber to counteract the in X,Y and Z directions. A measured current is run through these coils that generates a counter magnetic field, so that the resultant magnetic field strength inside the chamber is zero.

Additional features consist of a sputter gun (IS 40C1, PREVAC), a leak valve (VAT Vakuumventile AG) to dose gases into the main chamber, a PREVAC LED lighting system, and a high-resolution camera for sample alignment (Baumer Optronics GmbH).

A2.3 X-ray Source and Analyzer

The setup has a SPECS Al K α lab x-ray source (μ FOCUS 600 Monochromated X-ray Source, $E = 1486.7$ eV) which produces high intensity X-rays with a spot size under 200 μm on the sample. The small spot size permits a monochromator resolution of 0.25 eV to be achieved for Al K α . The lab source is equipped with a near ambient pressure (NAP) extension containing a SiN $_x$ window that separates the X-ray source chamber from the main chamber, enabling measurements at pressures as high as ~ 25 mbar, while maintaining high vacuum in the X-ray source chamber. The X-ray source is cooled by cooling water supplied through a control unit (SPECS CCX70 Control Unit) designed to provide high voltage isolation, controlled water pressure and temperature as well as filtering against particulate matter.

The analyzer unit is SPECS PHOIBOS 150, which contains a 3-stage differential pumping system with tunable apertures and a 1-D delay line detector (DLD). A pneumatic gate valve separates the pre-lens system from the rest of the analyzer in case a high pressure is detected in the

A Supplementary Information on Chapter 2

main chamber, which will be discussed in detail in the interlock section of the paper. The analyzer is interface with the main chamber through a 300 μm aperture nozzle. The apertures and pumping speed of the analyzer is tuned such that measurements up to 25 mbar can be performed. In order to keep track of the gaseous products formed during the heterogeneous reactions as well as water and other vapors escaping during electrochemical reactions during in situ XPS experiments, an online quadrupole mass analyzer (RGA 200, Stanford Research Instruments) is placed between the first and the second differential pumping stage. Gases and vapors escaping the main chamber into the analyzer unit are detected and analyzed inline in real time, giving information about the composition of the gaseous mixture at the sample surface.

A2.4 Electrolyte and Gas Supply

The electrochemical manipulator extension is connected to an electrolyte supply system capable of switching between different electrolytes. This is made possible by installing several electrolyte bottles to the same supply and return electrolyte lines with a selection valve in between. The selection valves used in this case enable up to four electrolyte bottles to be connected to the system, enabling a closed circulation by setting the supply and return selection valves to the same bottle. It is also possible to bubble a selection of gases through the electrolyte depending on the requirement of the reaction. Figure A2.2 shows the schematic diagram of the electrolyte supply system.

One of the most frequent problems encountered in in situ electrochemical spectroscopy is the air bubble entrapment at the electrodes. This disrupts the electrolyte connection between the electrodes and causes high solution resistance and noise in the voltametric readings. In order to solve this problem, we have installed a vacuum pumped bubble trap (Darwin Microfluidics) which removes any bubbles and undissolved gases from the electrolyte before it reaches the cell.

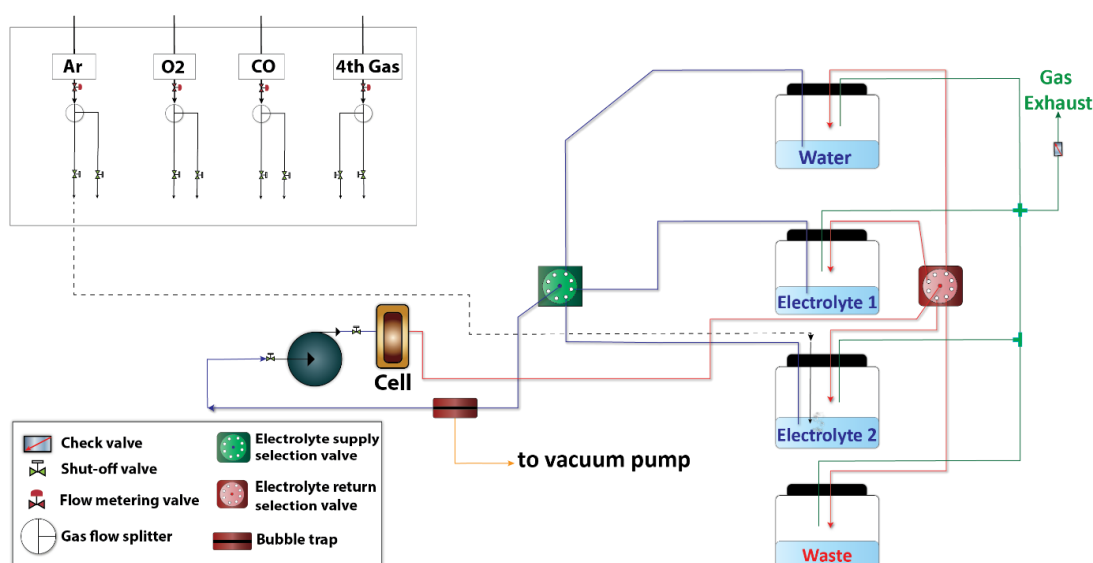


Figure A2.2 : Schematic diagram of the electrolyte and gas supply

A Supplementary Information on Chapter 2

A2.5 Safety Interlock System

A number of safety features are installed in the system to safeguard it in case of a variety of adverse scenarios. The idea behind designing the safety interlock system is to a) preserve the main chamber vacuum, b) prevent electrolyte leakage into the main chamber, c) protect the analyzer against the liquid droplets and d) protect the x-ray source and NAP extension window against liquid spillage and abrupt changes in pressure. Most of these securities become relevant while the electrochemical flow cell is in operation due to the risks associated with operating a liquid flow cell in a vacuum chamber. The safety systems can be broadly classified as *pressure safety system* and *power failure safety system*, which are briefly described as below and are shown as a schematic in Figure A2.3:

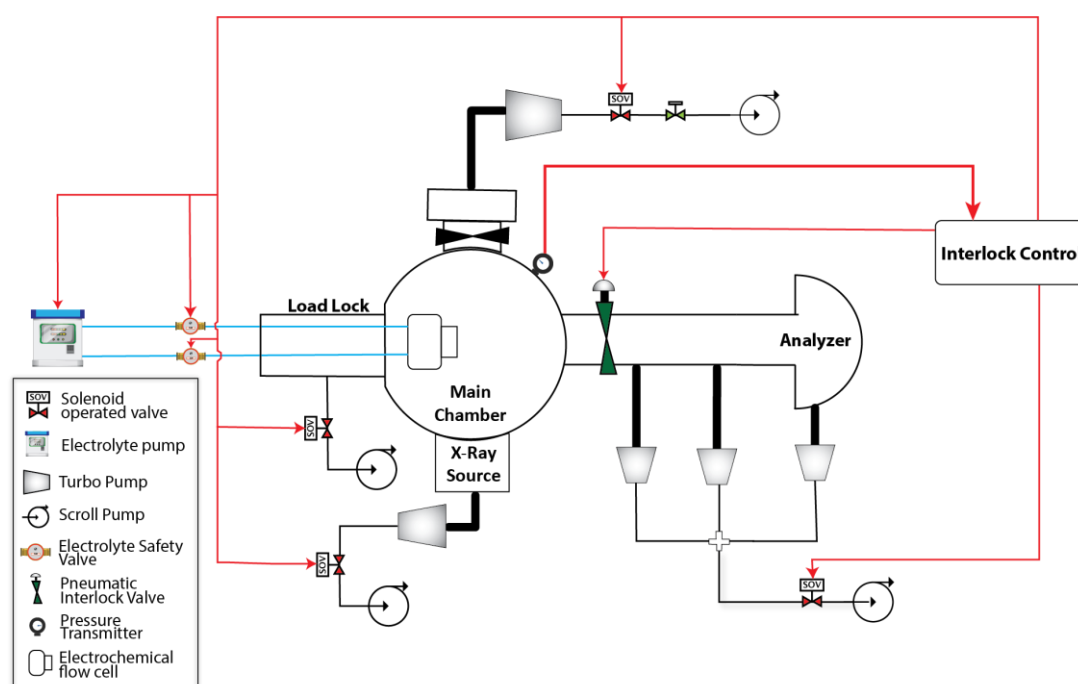


Figure A2.3 : Safety Interlock Schematic for EC-NAP-XPS

i) Pressure Safety Interlock

As mentioned earlier, there is a risk of electrolyte spillage from the flow cell into the vacuum. This can, in addition to spillage of (sometimes corrosive) electrolyte into the main chamber, result in electrolyte droplets being sucked into the high voltage parts of the analyzer and the X-ray source. In order to minimize the risk in case of leakage from the electrochemical cell, the pressure safety interlock is programmed to detect abrupt rises in pressure inside the main chamber. In case of detection of a pressure rise due to an electrolyte leak, the pressure transmitter coupled with the interlock control will trigger the emergency steps. These emergency steps include stopping the electrolyte pump, closing the safety valves on the electrolyte supply/return lines and closing the pneumatic interlock valve on the pre-lens stage of the analyzer system.

A Supplementary Information on Chapter 2

ii) Power Failure Interlock

The power failure interlock is aimed at preserving a static vacuum inside the setup in case of a power failure. In case of a power failure, the system can vent rapidly resulting in rupturing of the SiN_x window installed in the X-ray source NAP extension as well damage to the turbo pumps. To prevent that, the interlock is programmed to close all the solenoid operated valves (SOVs) installed between the turbo and scroll pumps immediately.

A2.6 Bake out

The entire setup can be baked out partially or all at once. In partial bake-out, the setup is divided into separate temperature zones, which makes it is possible to separately bake-out the analyzer, main chamber and the x-ray source using a combination of PREVAC BCU14 and Hemi Heating bakeout controllers.

A2.7 Cleaning procedure for components that are wetted in electrochemical experiments

Trace impurities present in the electrolyte can cause diminishing of the charge of existing voltametric measurements as well as introduce erroneous peaks⁴ rendering the results unreliable.

To be able to produce reliable electrochemistry, all the surfaces of the electrochemical setup that come in contact with the electrolyte can be cleaned to glass cell electrochemistry standards. An acidified solution KMnO₄ at pH 1 was prepared in one of the electrolyte bottles and circulated through the electrochemical cell for several hours on circulation. KMnO₄ is a strong oxidizing agent and removes the adsorbed impurities on the surfaces. The circulating solution was replaced with a 10% solution of H₂SO₄ and H₂O₂ (piranha solution) in ultra-high purity water (MiliQ, 18.2 MΩ.cm) followed by warm MiliQ water to rinse. The materials of construction for the electrochemical setup have been chosen such they are highly stable against harsh pH conditions⁵.

A2.8 Curve fitting parameters for Pt 4f

The raw XPS data was processed using CasaXPS Version 2.3.23. A Shirley background subtraction was used for all the datasets. The Lorentzian LF line shape was employed, which is an extension of Lorentzian LA line shape, the purpose of which is to limit the intensity of the asymmetric tails. It fits the data on the basis of 4 parameters; α , β , w and m . Varying ' α ' and ' β ' results in increasing or decreasing the spread of the tail for the Lorentzian curve, thereby affecting how steep are the edges of the line shape. ' m ' is the integer specifying the Lorentzian convolution by the gaussian function and ' w ' is the dampening factor to force the tails of the curve to reduce towards the limits of integration. An asymmetric form of Lorentzian LF line shape function was used for fitting the raw Pt 4f spectra. It is known through literature that, as a consequence of spin-orbit coupling, the electrons that leave Pt 4f orbital, generate two distinct energy peaks in the XPS spectrum categorized as 4f_{5/2} and 4f_{7/2}. Hence doublets for Pt⁰ Pt^{δ+}, Pt²⁺ and Pt⁴⁺ were used, with a constant spin-orbit splitting of 3.34 eV and a peak area

A Supplementary Information on Chapter 2

ratio of 3:4 for the $4f_{5/2}$ and $4f_{7/2}$ peaks. The details of the fitting parameters are shown in the table below.

The ranges for the peak positions of different Pt oxidation states were determined in accordance with the literature, especially cited in detail by Savelena and their group⁶ and previous work⁷. In order to accommodate the variations in the configuration of the beam energy for different experiments, a slight variation in the binding energy for Pt^0 (± 0.1 eV) was permitted. The line shape parameters were determined by comparing to the *ex-situ* XPS spectrum of a clean Pt foil to accommodate for the properties of the lab X-ray source. The Pt^{4+} line shape, peak position, and FWHM were determined by free fitting of a highly oxidized 3nm Pt sample produced at $1.5 V_{RHE}$, which displays a well-resolved Pt^{4+} peak. The line shape and FWHM of the other components was determined at low potential, where the metallic contribution is dominant. Note, however, that there is no potential at which only one component could be fitted. This is in line with the notion that the Pt surface atom are always in contact with adsorbates (e.g. H_2O , OH , O , $R-SO_3^-$), which generates a $Pt^{\delta+}$ and a bulk Pt^0 peak. The consistency of the fit model was ensured by applying it to several data sets.

	Pt^0	$Pt^{\delta+}$	Pt^{2+}	Pt^{4+}
Line shape	LF(0.63,2,20,50)	LF(0.63,2,20,50)	LF(0.63,2,20,50)	LF(1.8,2,10,0)
Peak Position	71.1 - 70.9	72 - 71.2	72.7 - 72	Determined at highest potential of the dataset
FWHM	Free	Same as Pt^0	Same as Pt^0	Determined at highest potential of the dataset

Table A1.1 : Fitting parameters for Pt 4f spectral decomposition

A2.9 SEM Images of Graphene on membrane electrode assembly

As mentioned in the main text, low magnification images show a clear contrast between graphene covered and uncovered parts of the MEA.

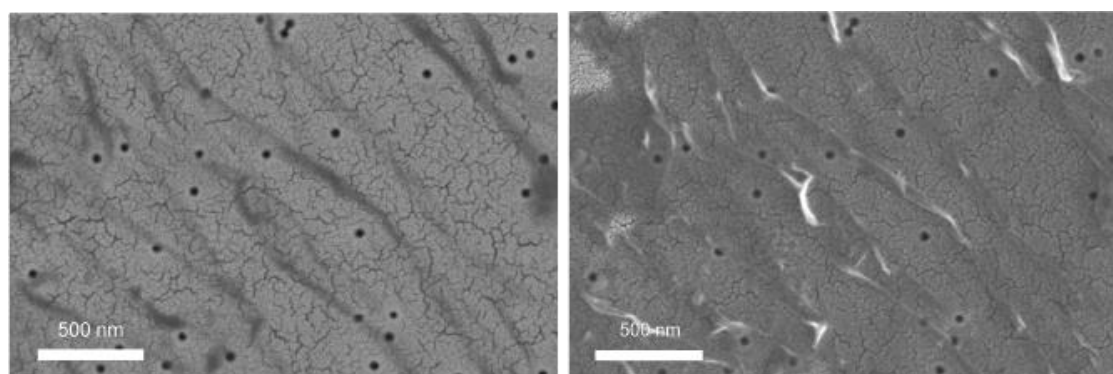


Figure A2.4 : Images of the 'pristine' film which show clearly the graphene layer on top of the Membrane Electrode Assembly

A Supplementary Information on Chapter 2

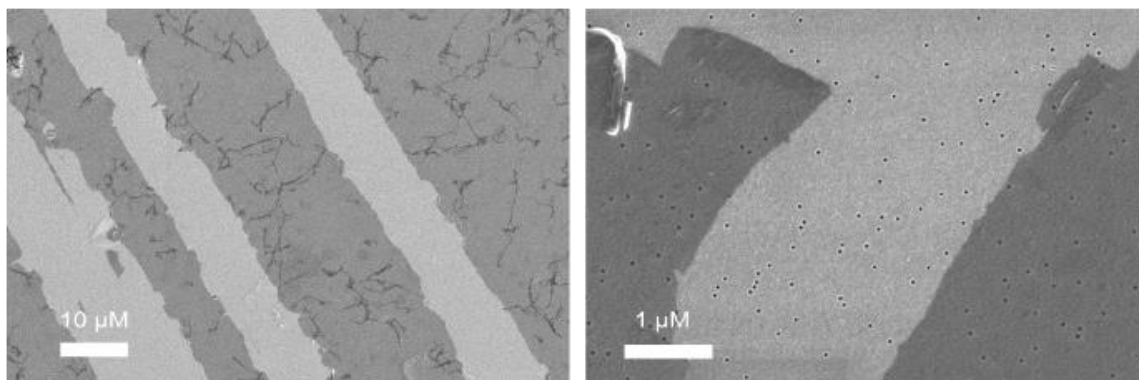


Figure A2.5: Contrast images showing the difference between graphene covered and uncovered parts of the MEA. The color contrast clearly shows the presence of graphene

In addition to slight film cracking observed in Pt, as mentioned in the main text, Figure A2.4 shows slight wrinkles in the bilayer graphene covering the MEA. Figure A2.5 shows SEM images taken at the edges of the graphene layer, showing a clear contrast between the graphene covered and uncovered portions of the MEA.

A Supplementary Information on Chapter 2

References

- (1) Favaro, M.; Jeong, B.; Ross, P. N.; Yano, J.; Hussain, Z.; Liu, Z.; Crumlin, E. J. Unravelling the Electrochemical Double Layer by Direct Probing of the Solid/Liquid Interface. *Nat Commun* **2016**, *7*. <https://doi.org/10.1038/ncomms12695>.
- (2) de Alwis, C.; Trought, M.; Crumlin, E. J.; Nemsak, S.; Perrine, K. A. Probing the Initial Stages of Iron Surface Corrosion: Effect of O₂ and H₂O on Surface Carbonation. *Appl Surf Sci* **2023**, *612*. <https://doi.org/10.1016/j.apsusc.2022.155596>.
- (3) Dietrich, P. M.; Gehrlein, L.; Maibach, J.; Thissen, A. Probing Lithium-Ion Battery Electrolytes with Laboratory near-Ambient Pressure Xps. *Crystals (Basel)* **2020**, *10* (11), 1–13. <https://doi.org/10.3390/cryst10111056>.
- (4) Fröhlich, N.; Fernández-Vidal, J.; Mascaró, F. V.; Shih, A. J.; Luo, M.; Koper, M. T. M. Effect of Trace Impurities in Perchloric Acid on Blank Voltammetry of Pt(111). *Electrochim Acta* **2023**, *466*. <https://doi.org/10.1016/j.electacta.2023.143035>.
- (5) VICI AG International. *Chemical Resistance PEEK® and Other Polymers General Reference*. https://www.daichem.co.jp/system/wp-content/themes/daichem2017/pdf/Chemical_resistance_jour.pdf. (accessed 2nd September, 2024)
- (6) Saveleva, V. A.; Papaefthimiou, V.; Daletou, M. K.; Doh, W. H.; Diebold, M.; Zafeiratos, S.; Savinova, E. R.; Ulhaq-bouillet, C.; Diebold, M.; Zafeiratos, S.; Savinova, E. R. Operando Near Ambient Pressure XPS (NAP-XPS) Study of the Pt Electrochemical Oxidation in H₂O and H₂O/O₂ Ambients. *Journal of Physical Chemistry C* **2016**, *120* (1), 15930–15940. <https://doi.org/10.1021/acs.jpcc.5b12410>.
- (7) Mom, R.; Frevel, L.; Velasco-Vélez, J. J.; Plodinec, M.; Knop-Gericke, A.; Schlögl, R. The Oxidation of Platinum under Wet Conditions Observed by Electrochemical X-Ray Photoelectron Spectroscopy. *J Am Chem Soc* **2019**, *141* (16), 6537–6544. <https://doi.org/10.1021/jacs.8b12284>.

B Supplementary Information on Chapter 3

B Supplementary Information on Chapter 3

B3.1 In situ cell sample preparation

The Polymer electrolyte membrane onto which Pt nanoparticles are to be deposited, is Nafion 117 supplied by Sigma-Aldrich. The membrane supplied by the vendor was cut into round discs of 11 mm in diameter, followed by the process of activation and cleaning. The Nafion membrane needs to be cleaned of the carbonaceous impurities. For this purpose, the Nafion discs were treated with a 3% H_2O_2 solution at 80°C for 2 hr and then with dilute H_2SO_4 solution (0.5 M) for the same duration and temperature.

The membrane electrode assembly (MEA) is prepared by sputter depositing Pt nanoparticles onto a polymer exchange membrane using a Pt target (ChemPUR GmbH, 99.5% purity) using a DC magnetron sputter coater 208HR by Cressington (Watford, UK). The process was carried out in an Argon atmosphere at 0.1 mbar and a pre-programmed sputtering current of 40 mA. The thickness of the Pt layer was controlled by automated MTM-20 high resolution thickness controller which constantly monitors the thickness of the deposited film as a function of the programmed density (for Pt = 19.45 g.cm^{-3}) of the material of interest and the particle deposition was calibrated using TEM. For our study, the thickness of the Pt layer was controlled between 3-4 nm.

Following the preparation of the MEA, a graphene layer is deposited on top of the Pt nanoparticles to impede the escape of the electrolyte during the spectroscopic measurements as well as to serve as an X-ray/photoelectron transparent window ($>300 \text{ eV}$) and as the electrical contact with the Pt nanoparticles. Graphene is deposited using a wet chemical method. Graphene supported on copper (Graphenea SA) was etched in a 40 g/L solution of ammonium sulfate overnight, dissolving copper and leaving the graphene layer floating on the liquid surface which is visible against a white background. The solution was then exchanged with pure water and the MEA was placed inside the water below the graphene and the liquid level was the lowered such that the graphene layer would land on the membrane. The prepared sample with graphene was dried at room temperature and proper placement of graphene was ensured on the membrane by visual inspection.

B3.2 Change in concentration of different oxidation states of Pt with changing potential

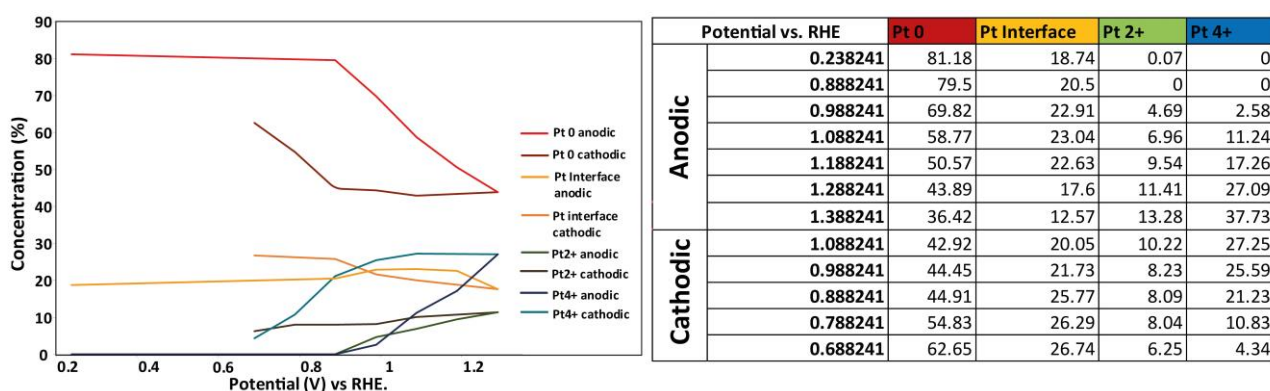


Figure B3.1: Percentage concentration of Pt oxidation states vs applied potential

B Supplementary Information on Chapter 3

Figure B3.1 shows a detailed picture of Pt oxidation observed at different step potentials. The difference in compositions at, for example, $0.9 V_{\text{RHE}}$ and $1.0 V_{\text{RHE}}$ during the cathodic and the anodic parts show the electrochemical irreversibility at which the oxide species on platinum are formed and reduced.

B3.3 Catalyst wetting observed via XAS spectrum

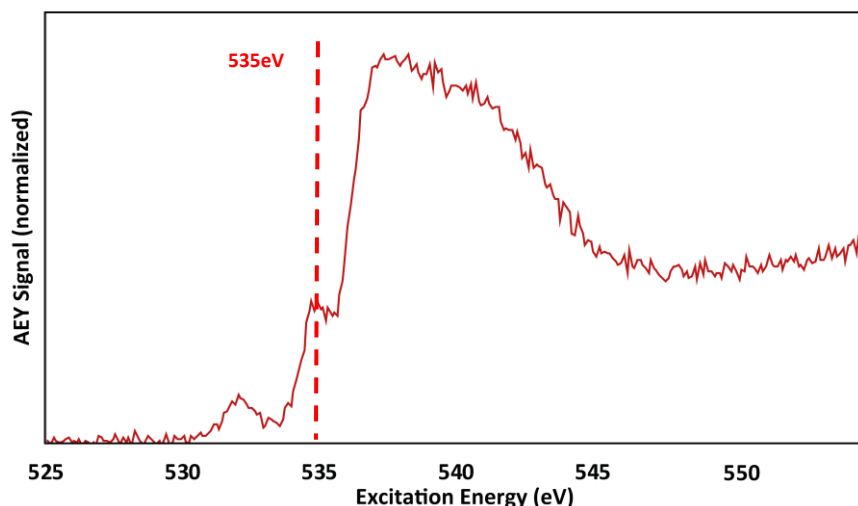


Figure B3.2: Effect of graphene covering on O-K edge spectra recorded at $0.7 V_{\text{RHE}}$

One of the most important features of the in situ spectroscopy cell is its ability to ensure the wettability of the catalyst under vacuum conditions. To check the wetting of the catalyst, we use in situ O-K-edge XAS spectroscopy, which is conducted during the in situ XPS experiments in the same geometry. One of the most important features in the O-K-edge spectrum that we have used to track the wetting of the Pt nanoparticles is the peak at 535 eV, which is very typical for liquid water^{1,2}. The O-K edge spectrum shown in Figure B3.2 is measured at a low potential of $0.7 V_{\text{RHE}}$ to avoid the contribution from platinum oxides. To reduce the noise in the PEY spectrum, an average of several spectra was taken at several locations on the catalyst surface to avoid the effects of beam damage.

As shown in Figure B3.2, the 535 eV peak is very pronounced. This can only be explained by either the presence of liquid water, or by a significant contribution from graphene oxide to the spectrum. However, graphene oxide also produces a strong resonance at about 531.9 eV. In our case, only a weak contribution is visible, ruling out the possibility that functional groups on the graphene window have contributed significantly to the 535 eV peak¹. Hence, we can say with certainty that the peak at 535 eV in the O-K edge spectrum predominantly originates from water, i.e. that the catalyst layer was properly wetted during the in situ XPS experiments.

B Supplementary Information on Chapter 3

B3.4 XPS Data fitting parameters

The raw XPS data was processed using CasaXPS Version 2.3.23. A Shirley background subtraction was used for all the datasets. The Lorentzian LF line shape was employed, which is an extension of Lorentzian LA line shape, the purpose of which is to limit the intensity of the asymmetric tails. It fits the data on the basis of 4 parameters; α , β , w and m . Varying ' α ' and ' β ' results in increasing or decreasing the spread of the tail for the Lorentzian curve, thereby affecting how steep are the edges of the line shape. ' m ' is the integer specifying the Lorentzian convolution by the gaussian function and ' w ' is the dampening factor to force the tails of the curve to reduce towards the limits of integration. An asymmetric form of Lorentzian LF line shape function was used for fitting the raw Pt4f spectra. It is known through literature that, as a consequence of spin-orbit coupling, the electrons that leave Pt4f orbital, generate two distinct energy peaks in the XPS spectrum categorized as $4f_{5/2}$ and $4f_{7/2}$. Hence doublets for Pt⁰ Pt ^{δ^+} , Pt²⁺ and Pt⁴⁺ were used, with a constant spin-orbit splitting of 3.34 eV and a peak area ratio of 3:4 for the $4f_{5/2}$ and $4f_{7/2}$ peaks. The details of the fitting parameters are shown in the table below.

	Pt ⁰	Pt ^{δ^+}	Pt ²⁺	Pt ⁴⁺
Line shape	LF(0.63,2,20,70)	LF(0.63,2,20,70)	LF(0.63,2,20,70)	LF(1.8,2,10,0)
Peak Position	70.81 - 70.7999	72 - 71.2	72.7 - 72	Determined at highest potential of the dataset
FWHM	Free	Same as Pt0	Same as Pt0	Determined at highest potential of the dataset

Table C3.1: Fitting parameters for Pt 4f spectral decomposition

The ranges for the peak positions of different Pt oxidation states were determined in accordance with the literature, especially cited in detail by Savelena and their group³ and previous work¹. In order to accommodate the variations in the configuration of the beam energy for different experiments, a slight variation in the binding energy for Pt⁰ (± 0.1 eV) was permitted. The line shape parameters were determined in similar fashion as in previous work¹. The Pt⁴⁺ line shape, peak position, and FWHM were determined by free fitting of a highly oxidized 4nm Pt sample produced at 1.85 V_{RHE}, which displays a well-resolved Pt⁴⁺ peak. The line shape and FWHM of the other components was determined at low potential, where the metallic contribution is dominant. Note, however, that there is no potential at which only one component could be fitted. This is in line with the notion that the Pt surface atom are always in contact with adsorbates (e.g. H₂O, OH, O, R-SO₃⁻), which generates a Pt ^{δ^+} and a bulk Pt⁰ peak. The consistency of the fit model was ensured by applying it to several data sets.

B Supplementary Information on Chapter 3

B3.5 Charge transfer calculation for XPS data

As mentioned in the main text, an oxidation charge transfer value was calculated based on the ratio of oxidation states observed in the XPS data. Since the comparison of this value is to be drawn with the measured surface oxidation charge of Pt nanoparticles in the electrochemical cell, the XPS data (as shown in Figure B3.1) had to be corrected to represent the surface of the nanoparticle only. To estimate the fraction of the total XPS signal emerging from the nanoparticle surface, it was assumed that at 1.4 V_{RHE} the surface layer is completely oxidized (as confirmed by oxide layer thickness modelling). Hence, the signal from Pt⁰ at 1.4 V_{RHE} arises from subsurface while Pt^{δ+}, Pt²⁺ and Pt⁴⁺ species constitute the surface signal, which comes out to be ~63% of the measured XPS signal. The intensities of the Pt^{δ+}, Pt²⁺ and Pt⁴⁺ contributions shown in Figure B3.1 were rescaled using this number, so that they represent the fraction of the surface that was occupied by these species.

The basis of oxidation charge calculation is the formation of a monolayer of oxides on the Pt surface and considering the formation of PtO(Pt²⁺), PtO₂(Pt⁴⁺) and Pt_{Interface oxide}(Pt^{δ+}) as 2e⁻, 4e⁻ and 1e⁻ transfer processes, respectively. The average no. of e⁻ transferred by the surface Pt atoms was calculated for each value of the step potentials shown in Figure B3.1 as follows:

$$Avg. e - transferred = \frac{(x_{Pt\delta+} * 1) + (x_{Pt2+} * 2) + (x_{Pt4+} * 4)}{0.63} \quad (2)$$

Where $x_{Pt\delta+}$ is the measured fraction of Pt species and 0.63 represents the fraction of the XPS signal originating from the surface of the nanoparticle. The calculated average number of electrons transferred has to be corrected to exclude the contribution from adsorbed oxygen or OH species (O_{ads}/OH_{ads}) that are already present at the base potential of the pulses in the electrochemical experiment (0.7 V_{RHE}). We approximated this correction by subtracting the number of electrons transferred at 0.9 V_{RHE} from the ones calculated at higher potentials:

$$Corrected e - transferred at V_{pulse} = (Calculated e - transferred at V_{pulse}) - (e - transferred at 0.9 V_{RHE}) \quad (3)$$

Where $V_{pulse} = 1.2, 1.3$ and $1.4 V_{RHE}$.

B Supplementary Information on Chapter 3

B3.6 XAS experiments with consecutive voltage pulses

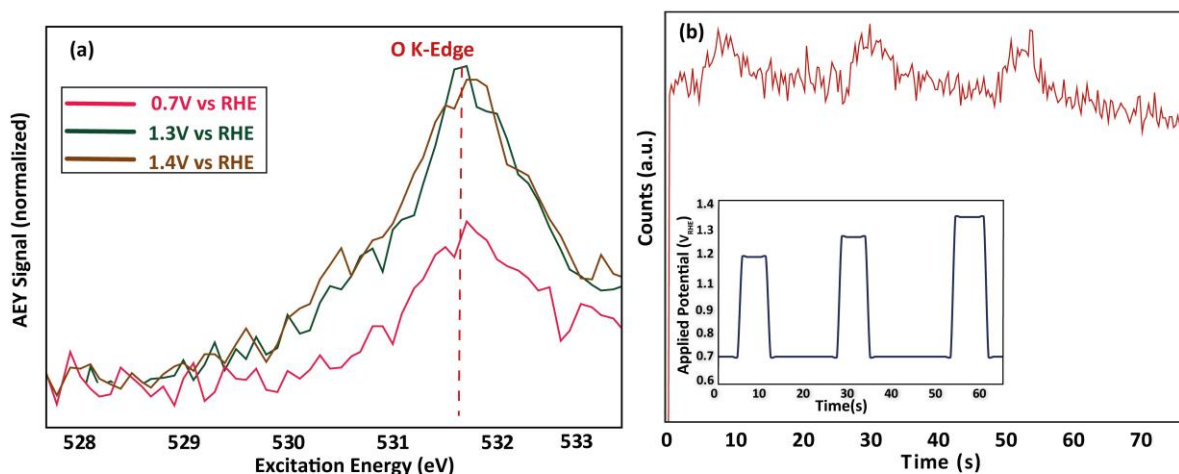


Figure B3.3: XAS spectra for applied pulse potentials. (a) Inset shows the consecutive pulses applied and the main set shows tracked XAS spectrum peak at 531.9 eV while (b) shows the same peak at different pulse potential in overlay arrangement

Figure B3.3(a) shows XAS spectra tracking the O K-edge peaks at 531.9 eV, which is associated with the formation of Pt oxides¹ exhibiting significant oxidation at higher anodic potentials. It is also indicated in the literature that a high O K-edge intensity between 529.5 eV and 532 eV at potentials as high as 1.3 V_{RHE} and 1.4 V_{RHE} can be associated with the formation of a considerable amount of PtO_2 ^{4–6} which is consistent with our XPS results. The O K-edge spectrum in the main set of Figure B3.3(b) show a corresponding sharp spike at 531.9 eV for every potential pulse applied as shown in the inset, indicating significant oxidation during SU/SD pulses. It is also noticeable that for each of these pulse responses, the rise is much steeper than the fall which tells us about the kinetics of oxidation (rise) being much faster than reduction (fall).

B3.7 Extended potential pulse experiment (XAS)

To observe the oxidation behavior for prolonged oxide conditioning times, the applied potential was raised instantaneously from 0.7 V_{RHE} and to 1.4 V_{RHE} and maintained, with the intensity of the O-K edge at 531.9 eV tracked as a function of time. It can be seen clearly from Figure B3.4 that the O-K edge peak shows a plateau following an instantaneous spike in counts as a function of potential pulse, indicating swift surface oxidation of Pt nanoparticles after which the role of diffusion becomes more important and oxidation slows down. This observation confirms the conclusion that was drawn from similar electrochemical experiment indicated in Figure 3.6.

B Supplementary Information on Chapter 3

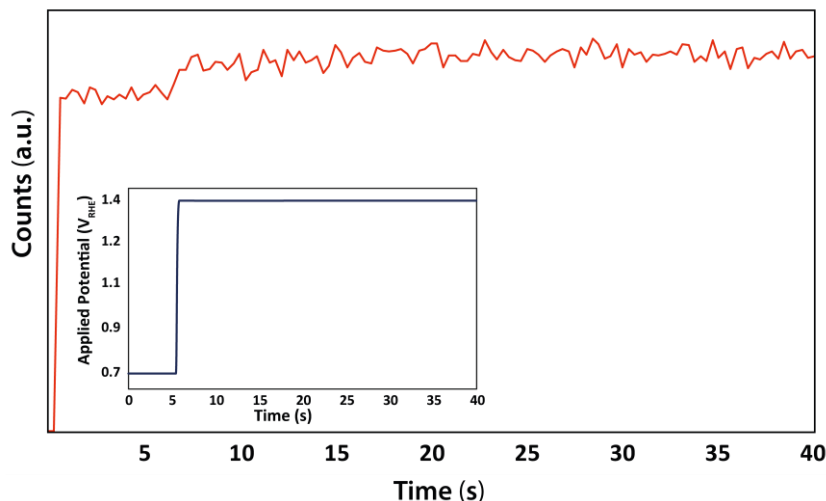


Figure B3.4: Time resolved O-K edge peak intensity at 531.9 eV (main set) for potential hold scheme at 1.4 V_{RHE} (inset)

B3.8 Modelling of oxide layer thickness

The initial particle size before oxidation was taken as 2.5 nm. All the components highlighted in the XPS data fitting (see Figure 3.4) were incorporated in the thickness modelling for both the models discussed below.

a) Shard's model

Shard's model⁷ provides us with a straightforward approach to estimate the thickness of the overlayer on a nanoparticle as a function of the normalized XPS intensities observed experimentally. In our paper, the fundamental equation adopted from the Shard's model to estimate the oxide layer thickness is as follows;

$$T_{NP} = \frac{T_{R\sim 1} + \beta T_o}{1 + \beta} \quad (4)$$

Where T_{NP} is the thickness of the oxide layer, while $T_{R\sim 1}$, β and T_o are variables which are calculated as a function of α , β and core radius of the nanoparticle (R). α and β are calculated as follows:

$$\alpha = \frac{1.8}{A^{0.1} B^{0.5} C^{0.4}} \quad (5)$$

$$\beta = \frac{0.13 \alpha^{2.5}}{R^{1.5}} \quad (6)$$

Based on previous TEM data¹, we estimate the core radius to be around 2.5 nm for unoxidized particles.

Shard's model in essence takes into account one¹ component in the core of the particle and one component in the oxide shell. For our model, a weighted average of the relative electron attenuation length and normalized XPS intensities had to be incorporated into variables A and C to take into account all the oxide components identified in the XPS analysis:

B Supplementary Information on Chapter 3

$$A = \left(\left(\frac{x_{Pt\delta+}}{x_{Pt\delta+} + x_{Pt2+} + x_{Pt4+}} \right) \left(\frac{I_{Pt\delta+}}{I_{Pt}} \right) \left(\frac{I_{Pt}^0}{I_{Pt\delta+}^0} \right) \right) + \left(\left(\frac{x_{Pt2+}}{x_{Pt\delta+} + x_{Pt2+} + x_{Pt4+}} \right) \left(\frac{I_{Pt2+}}{I_{Pt}} \right) \left(\frac{I_{Pt}^0}{I_{Pt2+}^0} \right) \right) + \left(\left(\frac{x_{Pt4+}}{x_{Pt\delta+} + x_{Pt2+} + x_{Pt4+}} \right) \left(\frac{I_{Pt4+}}{I_{Pt}} \right) \left(\frac{I_{Pt}^0}{I_{Pt4+}^0} \right) \right) \quad (7)$$

$$C = \left(\left(\frac{x_{Pt\delta+}}{x_{Pt\delta+} + x_{Pt2+} + x_{Pt4+}} \right) \left(\frac{L_{Pt\delta+}}{L_{Pt}} \right) \right) + \left(\left(\frac{x_{Pt2+}}{x_{Pt\delta+} + x_{Pt2+} + x_{Pt4+}} \right) \left(\frac{L_{Pt2+}}{L_{Pt}} \right) \right) + \left(\left(\frac{x_{Pt4+}}{x_{Pt\delta+} + x_{Pt2+} + x_{Pt4+}} \right) \left(\frac{L_{Pt4+}}{L_{Pt}} \right) \right) \quad (8)$$

where

$x_{Pt\ i}$ (where $i = \delta+, 2+, 4+$) : concentration of $Pt^{\delta+}$, Pt^{2+} and Pt^{4+}

$\frac{I_{Pt\ i}}{I_{Pt}}$ = ratio of measured XPS intensity of oxide component i in the shell and metallic Pt (assumed to be) in the core

$\frac{L_{Pt\ i}}{L_{Pt}}$ = ratio of the attenuation length of the photoelectrons arising from material i when travelling in the shell to the attenuation length of the photoelectrons arising from material i when traveling in the core

$\frac{I_{Pt}^0}{I_{Pt\ i}^0}$ = ratio of XPS intensities for a flat, pure Pt metal surface and a flat pure version of material i .

B is the ratio of attenuation lengths of the core and shell material for photoelectrons traveling in the shell. Since the kinetic energy of the photoelectrons of all species discussed here is roughly the same, B can be taken as 1.

The pure component intensities are estimated in this model using the following expression;

$$\frac{I_{Pt\ i}^0}{I_{Pt}^0} = \frac{N_{Pt}^0 \cdot L_{Pt\ in\ Pt} \cdot G(E_{Pt})}{N_{Pt\ i}^0 \cdot L_{i\ in\ i} \cdot G(E_{Pt\ i})} \quad (9)$$

In the above equation, N_{Pt}^0 and $N_{Pt\ i}^0$ are the number densities ($g \cdot cm^{-3}$) of pure metal and pure oxide components ($Pt = 21.45$, $Pt^{\delta+}(Pt_{\text{interface oxides}}) = 20$, $Pt^{2+}(PtO) = 14.9$, $Pt^{4+}(PtO_2) = 10.2$), $L_{Pt\ in\ Pt}$ is the attenuation length in pure metallic Pt, $L_{i\ in\ i}$ is the attenuation length in material i , and $G(E_{Pt})$ and $G(E_{Pt\ i})$ are the spectrometer transmission factors as a function of photoelectron kinetic energies. Since the kinetic energy of the photoelectrons of all species discussed here is roughly the same, the transmission factors are taken as equal and cancel out.

Note that the shell thickness T and the particle radius R are expressed in units of $L_{Pt\ i}$ in the model.

B3.8 Ertl and Küpper's model

Ertl and Küpper's model is an alternative way to estimate the oxide layer thickness (d) on the nanoparticles⁸. The equation used in the modelling of the thickness is as follows;

B Supplementary Information on Chapter 3

$$d = L_{avg} \cdot \cos\theta \cdot \ln\left(1 + \frac{I_{ox} \cdot I_M^o}{I_M \cdot I_{ox}^o}\right) \quad (10)$$

Where L_{avg} stands for the average photoelectron attenuation length based on the weighted average of the metal and oxide species (done similarly as in Shard's model), θ is the take-off angle normal to the surface (taken as 57° here). The value of take-off angle is derived from the publication of Castner and coworkers, who have used similar values for nanoparticles of a comparable size as our application⁹.

B Supplementary Information on Chapter 3

References

- (1) Mom, R.; Frevel, L.; Velasco-Vélez, J. J.; Plodinec, M.; Knop-Gericke, A.; Schlögl, R. The Oxidation of Platinum under Wet Conditions Observed by Electrochemical X-Ray Photoelectron Spectroscopy. *J. Am. Chem. Soc.* **2019**, *141* (16), 6537–6544. <https://doi.org/10.1021/jacs.8b12284>.
- (2) Merte, L. R.; Behafarid, F.; Miller, D. J.; Friebe, D.; Cho, S.; Mbuga, F.; Sokaras, D.; Alonso-mori, R.; Weng, T. C.; Nordlund, D.; Nilsson, A.; Cuenya, B. R.; Roldan Cuenya, B. Electrochemical Oxidation of Size-Selected Pt Nanoparticles Studied Using in Situ High-Energy-Resolution X-Ray Absorption Spectroscopy. *ACS Catal.* **2012**, *2* (11), 2371–2376. <https://doi.org/10.1021/cs300494f>.
- (3) Saveleva, V. A.; Papaefthimiou, V.; Daletou, M. K.; Doh, W. H.; Diebold, M.; Zafeiratos, S.; Savinova, E. R.; Ulhaq-bouillet, C.; Diebold, M.; Zafeiratos, S.; Savinova, E. R. Operando Near Ambient Pressure XPS (NAP-XPS) Study of the Pt Electrochemical Oxidation in H₂O and H₂O/O₂ Ambients. *J. Phys. Chem. C* **2016**, *120* (1), 15930–15940. <https://doi.org/10.1021/acs.jpcc.5b12410>.
- (4) Kaya, S.; Casalongue, H. S.; Friebe, D.; Anniyev, T.; Miller, D. J. Oxidation of Pt (111) under Near-Ambient Conditions. **2011**, 195502 (November), 1–5. <https://doi.org/10.1103/PhysRevLett.107.195502>.
- (5) Costa, D.; Dintzer, T.; Arrigo, R.; Knop-gericke, D. A. Chemical Science In Situ Investigation of Dissociation and Migration Phenomena at the Pt / Electrolyte Interface of An. **2015**, 5635–5642. <https://doi.org/10.1039/C5SC01421B>.
- (6) H.Yoshida, S. Nonoyama, Y. Yazawa, T. H. Quantitative Determination of Platinum Oxidation State by XANES Analysis. *Phys. Scr. T* **2005**, *115* (1), 813–815. <https://doi.org/https://doi.org/10.1238/Physica.Topical.115a00813>.
- (7) Shard, A. G. A Straightforward Method for Interpreting XPS Data from Core-Shell Nanoparticles. *J. Phys. Chem. C* **2012**, *116* (31), 16806–16813. <https://doi.org/10.1021/jp305267d>.
- (8) Ertl, G., Küppers, J., & Grasserbauer, M. Low Energy Electrons and Surface Chemistry. *Anal. Chim. Acta* **1987**, *199* (1), 272–273. [https://doi.org/https://doi.org/10.1016/s0003-2670\(00\)82831-7](https://doi.org/https://doi.org/10.1016/s0003-2670(00)82831-7).
- (9) Techane, S. D.; Gamble, L. J.; Castner, D. G. Multitechnique Characterization of Self-Assembled Carboxylic Acid-Terminated Alkanethiol Monolayers on Nanoparticle and Flat Gold Surfaces. **2011**, 9432–9441.

C Supplementary Information on Chapter 4

C Supplementary Information on Chapter 4

C4.1 Nafion Membrane Activation

The Polymer electrolyte membrane with sputtered Pt nanoparticles is Nafion 117 supplied by Sigma-Aldrich. The membrane was cut into 1 cm squares, followed by the process of activation and cleaning. The Nafion membrane needs to be cleaned of the carbonaceous impurities. For this purpose, the samples were treated with a 3% H₂O₂ solution at 80°C for 2 hr and then with dilute H₂SO₄ solution (0.5 M) for the same duration and at the same temperature. Following the cleaning procedure, the membranes were rinsed with deionized water and stored dry.

C4.2 Glassy Carbon (GC) electrode preparation

5 mm diameter GC discs were polished with polycrystalline diamond suspension (MetaDi™ Supreme, Buehler) to a mirror finish. The electrodes were then ultrasonicated in deionized water to remove polishing solution residue. Clean GC discs were dried in an Argon gas stream. Pt and Pt₃Ni nanoparticles were sputter deposited onto the cleaned discs.

C4.3 Membrane Electrode Assembly Preparation

Pt₃Ni alloy and Pt metal were used to prepare the membrane electrode assembly (MEA) by sputter depositing the catalyst nanoparticles onto activated Nafion 117 polymer exchange membranes.

For Pt MEA samples, a Pt target (ChemPUR GmbH, 99.5% purity) and a DC magnetron sputter coater 208HR by Cressington (Watford, UK), were employed. A sputtering current of 40 mA was used with the sputter chamber pressure maintained at $\sim 4 \times 10^{-4}$ Pa. The sputtering process lasted for 2 minutes and 45 seconds to deposit a 5 nm thick layer of Pt.

Pt₃Ni alloys were deposited using two circular TORUS magnetrons (Kurt J. Lesker) operating simultaneously. 2" Pt (99.99% Safina) and 2" Ni (99.99% Kurt J. Lesker) targets were employed for the sputtering of Pt and Ni, respectively. Prior to deposition, the sputtering chamber was evacuated to a base pressure of 1×10^{-4} Pa. Sputtering was then performed in a 2.6 Pa argon atmosphere in DC mode, with the power set to 28 W for Pt and 30 W for Ni to achieve the desired alloy composition. The deposition lasted for 1 minute and 35 seconds to attain a 5 nm thickness of the deposited layer.

C4.4 Graphene deposition on the Nafion MEA

Following the preparation of the MEA, a graphene bi-layer is deposited on top of the Pt nanoparticles to impede the escape of the electrolyte during the spectroscopic measurements in the XPS vacuum chamber. This graphene serves as both an X-ray/photoelectron transparent window (>300 eV) and as the electrical contact with the Pt nanoparticles. Graphene is deposited using a wet chemical method. For this purpose, graphene supported on copper (Graphenea SA) was etched in a 40 g/L solution of ammonium persulfate overnight, dissolving copper and leaving the graphene layer floating on the liquid surface. The solution was then exchanged with pure water and the floating graphene was scooped off the surface of the water with the MEA. The prepared sample with graphene was dried at room temperature and proper placement of graphene was ensured on the membrane by visual inspection.

C4.5 EDX Sample Analysis

The sample composition was verified through bulk-sensitive Energy-Dispersive X-ray Spectroscopy (EDX), utilizing an XFlash detector (Bruker) integrated into the Mira 3 Scanning electron microscope (Tescan) operated at electron energy of 30 keV.

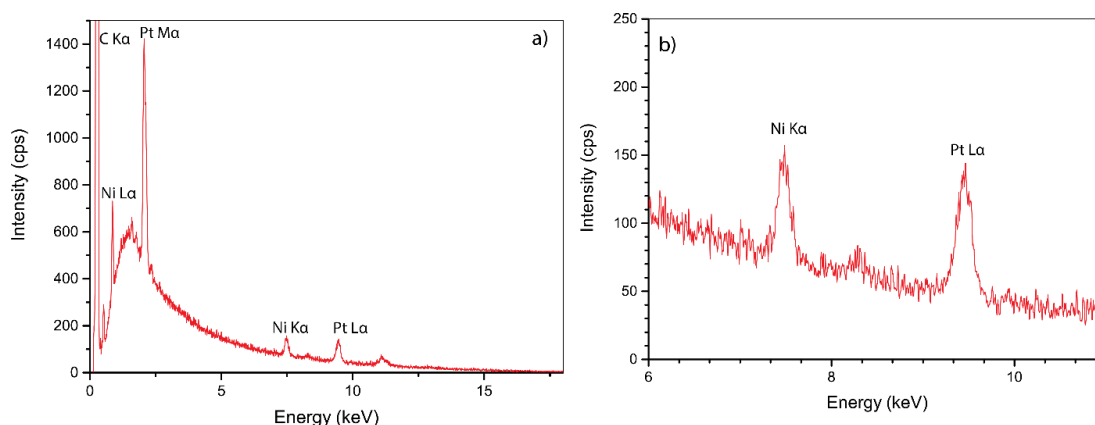


Figure C4.1: Energy Dispersive X-ray (EDX) analysis of as-prepared Pt₃Ni samples

The bulk composition of the as-deposited Pt₃Ni layer was quantified from the EDX spectra shown in Figure C4.1 by integrating the Ni Kα₁ (7.480 keV) and Pt Lα₁ (9.442 keV) lines. The calculated composition was Pt₇₃Ni₂₇, close to the intended Pt₃Ni composition.

C4.6 Cell Design

All experiments were performed in the newly designed Spectro-electrochemical flow-cell shown in Figure C4.2. A titanium top plate secures the MEA in the cell. A Pt wire is used as a counter electrode and Ag/AgCl electrode is used as a reference. Electrolyte connections are present at the rear of the cell, to which the electrolyte lines are connected via PTFE fittings. The main body of the cell is made out of PEEK. The cross section of the cell shown on the right hand side in Figure C4.2 shows the internal electrolyte cavity and the circulation. A minimum dead volume is maintained inside the cavity, minimizing the distance between the electrodes and the cell resistance.

C Supplementary Information on Chapter 4

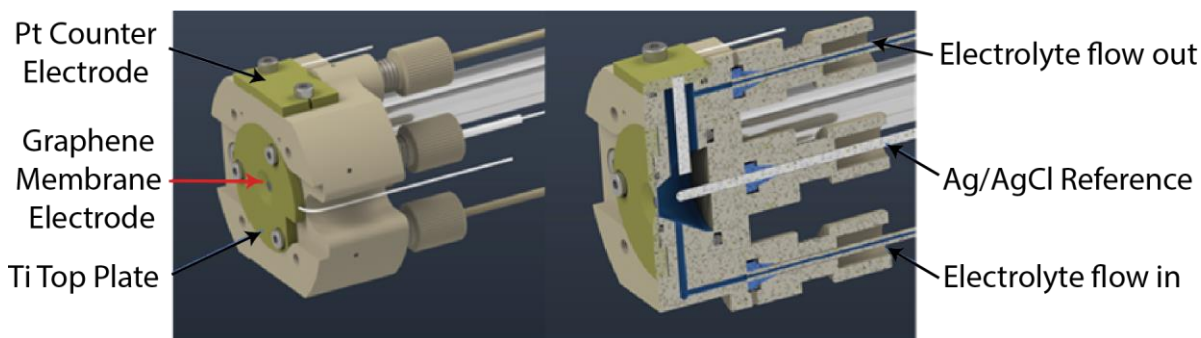


Figure C4.2: Schematic of the three-electrode spectro-electrochemical cell set-up for in-situ X-ray spectroscopy.

C4.7 Pt 4f XPS Data fitting

The raw XPS data was processed using CasaXPS Version 2.3.23. A Tougaard background subtraction was used for all the datasets. The Lorentzian LF line shape was employed, which is an extension of the Lorentzian LA line shape, the purpose of which is to limit the intensity of the asymmetric tails. It fits the data on the basis of 4 parameters; α , β , w and m . Varying ' α ' and ' β ' results in increasing or decreasing the spread of the tail for the Lorentzian curve, thereby affecting the steepness of the edges of the line shape. ' m ' is the integer specifying the Gaussian convolution with the Lorentzian function and ' w ' is the dampening factor to force the tails of to zero towards the limits of integration. An asymmetric form of Lorentzian LF line shape function was used for fitting the raw Pt 4f spectra. Doublets for Pt^0 , $\text{Pt}^{\delta+}$, Pt^{2+} and Pt^{4+} were used, with a constant spin-orbit splitting of 3.34 eV and a peak area ratio of 3:4 for the $4f_{5/2}$ and $4f_{7/2}$ peaks. The details of the fitting parameters are shown in the table below.

The ranges for the peak positions of different Pt oxidation states were determined in accordance with the literature, as summarized by Saveleva *et al.*¹, and previous work². In order to accommodate the variations in the configuration of the beam energy for different experiments, a slight variation in the binding energy for Pt^0 (± 0.1 eV) was permitted. The Pt^{4+} line shape, peak position, and FWHM were determined by free fitting of a highly oxidized 5nm Pt sample produced at 1.7 V_{RHE} , which displays a well-resolved Pt^{4+} peak. The line shape and FWHM of the other components was determined at low potential, where the metallic contribution is dominant. Note, however, that there is no potential at which only one component could be fitted. This is in line with the notion that the Pt surface atom are always in contact with adsorbates (e.g. H_2O , OH , O , R-SO_3^-), which generates a $\text{Pt}^{\delta+}$ and a bulk Pt^0 peak. The consistency of the fit model was ensured by applying it to several data sets.

C Supplementary Information on Chapter 4

	Pt ⁰	Pt ^{δ+}	Pt ²⁺	Pt ⁴⁺
Line shape	LF(0.9,2,60,50)	LF(0.9,2,60,50)	LF(0.9,2,60,50)	LF(3,3,30,10)
Peak Position	71.2 - 70.9	72 - 71.2	72.7 - 72	Determined at highest potential of the dataset
FWHM	Free	Same as Pt ⁰	Same as Pt ⁰	Determined at highest potential of the dataset

Table C4.1 : Fitting parameters for Pt 4f spectral decomposition

C4.8 Pt 4f / Ni 2p peak area integration

Pt 4f spectra were recorded at 600 eV excitation energy with 10 eV pass energy while the Ni 2p spectra were measured at 1900 eV excitation energy with 50 eV pass energy at same measurement spot. A different measurement spot was chosen for every potential to avoid beam damage to the Nafion membrane. A Tougaard background subtraction was applied to the spectra and the area under the curve was integrated in CasaXPS. The Pt 4f / Ni 2p ratio was calculated by simply dividing the area under the Pt 4f and Ni 2p spectra.

C4.9 Pt₃Ni SEM Images

Figure C4.3 shows the SEM images taken for an 'as prepared' Pt₃Ni MEA sample. A clear contrast between the graphene covered (dark) and bare catalyst surface (bright) on the MEA can be seen in Figure C4.3a by imaging at the edge of the deposited graphene. An area in the middle the graphene window is shown in Figure C4.3b. The lack of microscopic tears in the graphene confirms the quality of the window. Figure C4.3c shows a higher magnification. Here, the contrast originates from the catalyst layer (light) with respect to the non-conductive underlying Nafion (dark), both of which are imaged through the (fairly) electron-transparent graphene window. A clear cracking pattern can be observed, which is formed when the Pt₃Ni-coated Nafion membrane is inserted in water to pick up the graphene window. Nafion swells by about 10% in water, cracking up the film.

C Supplementary Information on Chapter 4

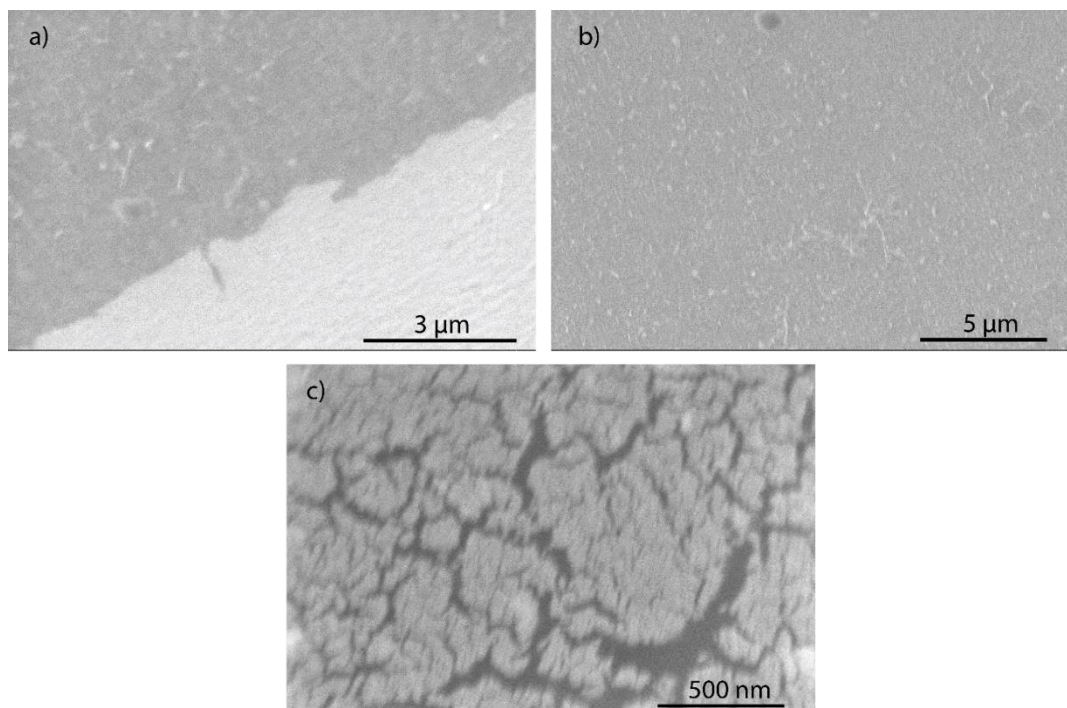


Figure C4.3: SEM Images for Pt_3Ni catalyst sputter deposited onto cleaned and activated Nafion membrane

Unfortunately, attaining higher resolution images of the MEA was not possible due to charging and beam damage of the Nafion membrane. However, Figure C4.4 shows a collection of SEM images for a similar catalyst loading deposited on a polished glassy carbon surface. Clusters of aggregated catalyst particles can be seen, with a grain size of about 8 nm.

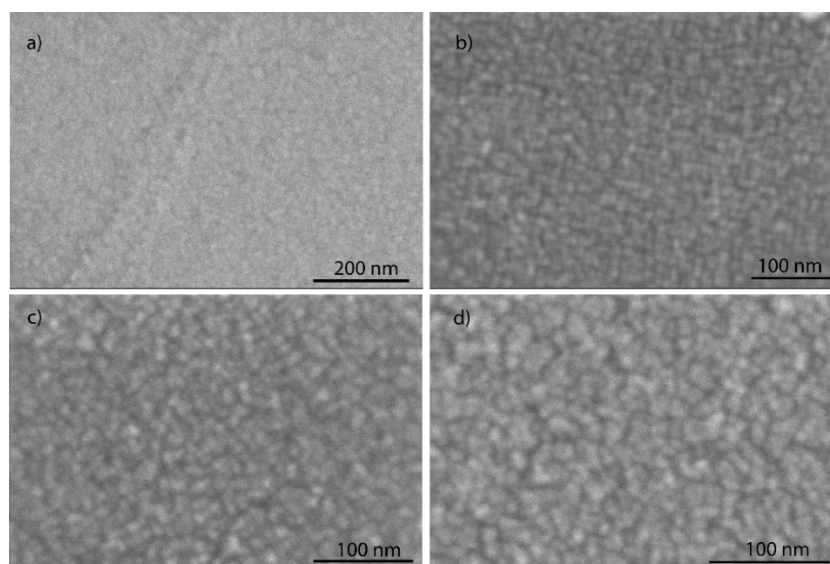


Figure C4.4: SEM Images for Pt_3Ni catalyst sputter deposited onto polished glassy carbon disk

C4.10 XAS Data processing and arctan correction for Ni L3 edge

Ni L-edge XAS data was processed using Athena (version 0.9.26), applying a linear pre-and post-edge correction and a normalization to the edge jump. The correctness of the processing was verified using the L_2 -edge jump, which should be 0.5 for a spectrum normalized to the L_3

C Supplementary Information on Chapter 4

edge jump due the spin-orbit splitting ratio of the 2p core level. In addition, we checked that the L₂ edge whiteness intensities showed the same trends as the L₃-edge whiteness intensity.

For the analysis of the intensity and weighted average peak position of the Ni L₃-edge in Figure 4.4 in the Main Text, an arctan baseline subtraction was applied using OriginPro 2017. Figure C4.5a (red curve) shows an example. The resultant background corrected curve is shown in Figure C4.5b, whereas Figure C4.5c shows its integrated version. The dotted lines in Figure C4.5c coincide with the middle (half) of the integrated intensity on the y-axis. The corresponding photon energy was used as the weighted average peak position in Figure C4.5c. For the peak intensity in Figure C4.4b of the Main Text, the plateau value of the integral was used, i.e. the area under the arctan baseline subtracted peak.

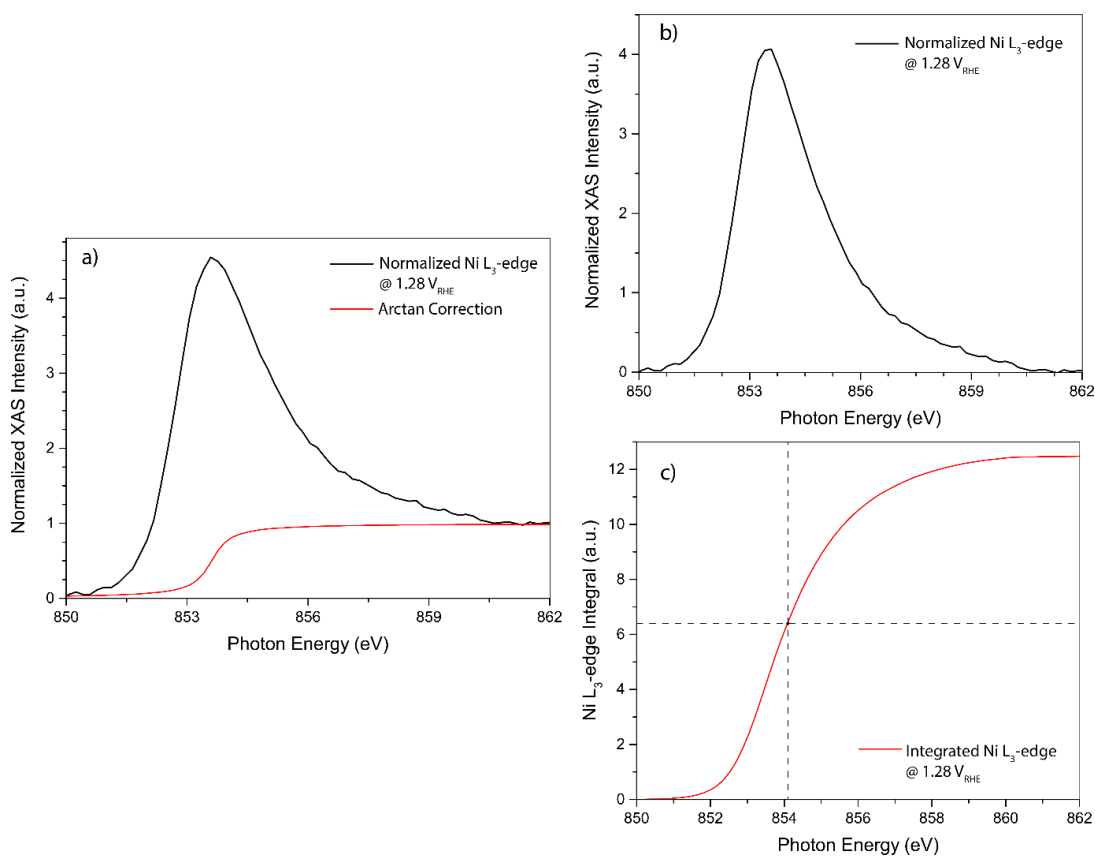


Figure C4.5: Arctan correction for the analysis of the Ni L₃-edge spectra; a) shows an example spectrum (black curve) and an arctan function to be subtracted (red curve), b) shows the resultant curve after the subtraction and c) shows the integrated version of b), where the dotted line indicated the weighted average peak position on the x-axis

C4.11 Pt & Pt₃Ni Cyclic voltammogram and activity

Pt and Pt₃Ni catalysts were tested in a glass cell for their electrochemical behavior measured in Argon purged 0.1 M H₂SO₄. Figure C4.6 shows similar voltametric behavior in the glass cell as observed in the spectro-electrochemical experiments discussed in the main text (Figure 4.1b), where weak adsorbate interaction in Pt₃Ni, as well as higher oxidation current as compared to bulk Pt catalyst, can be observed.

C Supplementary Information on Chapter 4

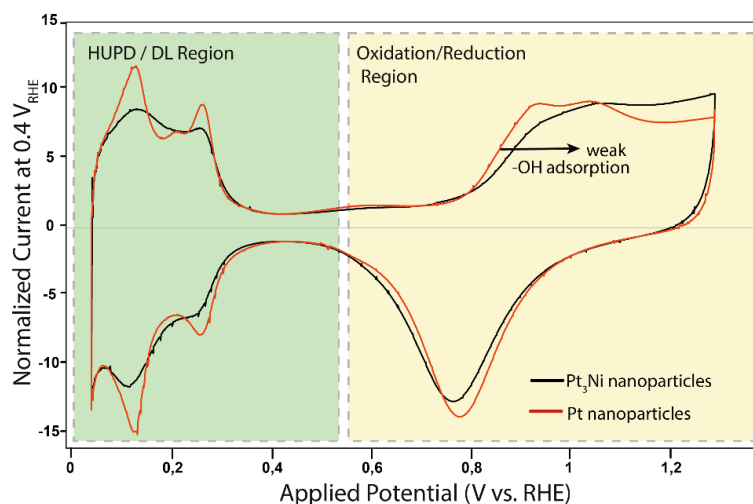


Figure C4.6: Cyclic voltammograms of Pt and Pt₃Ni catalyst nanoparticles deposited on glassy carbon substrate in Ar purged 0.1M H₂SO₄ highlighting Hydrogen Underpotential Deposition (HUPD), Double Layer (DL) and oxidation/reduction regions

C4.12 Ni 2p potential dependent XPS Spectra

Figure C4.7 shows Ni 2p XPS spectra measured at different potentials. The binding energy is consistent with metallic Ni.

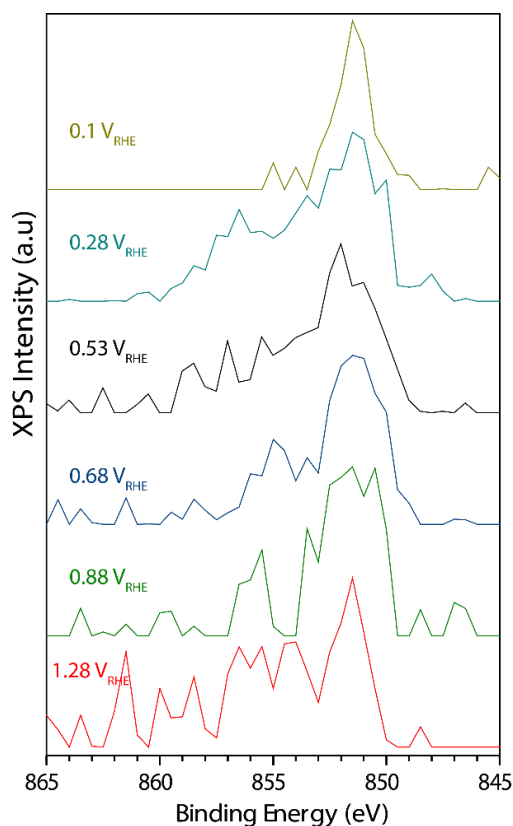


Figure C4.7: Ni 2p XPS spectra as a function of potential at 1900 eV excitation energy

C Supplementary Information on Chapter 4

References

- (1) Saveleva, V. A.; Papaefthimiou, V.; Daletou, M. K.; Doh, W. H.; Diebold, M.; Zafeiratos, S.; Savinova, E. R.; Ulhaq-bouillet, C.; Diebold, M.; Zafeiratos, S.; Savinova, E. R. Operando Near Ambient Pressure XPS (NAP-XPS) Study of the Pt Electrochemical Oxidation in H₂O and H₂O/O₂ Ambients. *Journal of Physical Chemistry C* 2016, 120 (1), 15930–15940. <https://doi.org/10.1021/acs.jpcc.5b12410>.
- (2) Javed, H.; Knop-Gericke, A.; Mom, R. V. Structural Model for Transient Pt Oxidation during Fuel Cell Start-up Using Electrochemical X-Ray Photoelectron Spectroscopy. *ACS Appl Mater Interfaces* 2022, 14 (31), 36238–36245. <https://doi.org/10.1021/acsami.2c09249>.

D Summary & Outlook

Summary:

Operando Spectro-electrochemical investigations of Pt and Pt-alloys as Fuel Cell Catalysts

Platinum and platinum alloys are considered the current state-of-the-art catalysts in fuel cells. However, although these materials have enabled the commercial use of fuel cells, they are still the limiting factor in the efficiency and lifetime of the fuel cell. Understanding the molecular mechanisms that lead to these limitations is essential to ensure optimal catalytic activity in the long term. In line with this, the oxygen reduction reaction at the fuel cell cathode, where the main degradation and efficiency losses occur, has been the focus of intensive research in the past decades. The developments in the past 20 years show that despite the considerable number of H₂ fuel cell vehicles on the road, there is still much room for improvement in catalyst design.

During the course of this thesis, we have focused on probing the electrode-electrolyte interface under fuel cell operation conditions to develop a better understanding of the structure-activity-degradation dynamics at the atomic scale. To enable this, we commissioned a modular NAP-XPS system in our own lab as discussed in *Chapter 2*, facilitating *operando* electrochemical studies on nano-structured electrocatalysts in any aqueous electrolyte, including those with dissolved gases. In the context of fuel cell studies, this enables *operando* studies on the electrode-electrolyte interface structure in oxygen-saturated electrolytes, deconvoluting the behaviors of the electrode, adsorbates, oxides and the electrolyte species during electrocatalysis.

In *Chapter 3*, we develop a deeper understanding of the Pt nanoparticle degradation during fuel cell start-up conditions, where rapid Pt catalyst degradation occurs during transient oxidation and reduction of the electrode surface. In our studies on Pt oxidation behavior under simulated start-up conditions, we show that a mixture of the Pt^{δ+}, Pt²⁺ and Pt⁴⁺ oxidation states are present on the catalyst from the onset of the oxidation. This structure is formed and equilibrated in a matter of seconds, i.e. within the time-scale of transient oxidation during fuel cell start-up. We also show that the oxides formed during initial transient startup/shutdown stages of the fuel cell may not fully reduce at operation conditions, which likely has negative impact on the catalytic activity.

In *Chapter 4*, we shift focus to Pt₃Ni catalysts, which are used in modern fuel cells due to their higher activity and stability compared to pure Pt. It has been shown in the literature that Pt-Ni alloys form a multi-atom thick Pt skin under electrochemical conditions. Here, we investigated dynamics of the subsurface Ni beneath this Pt skin as a function of applied

potential, and its role in the catalytic properties of the alloy. We show that the Ni in the particle core is highly mobile, moving closer to the surface at high potential and further from the surface at low potential. This affects their electron transfer properties to the catalytic intermediates on the catalyst surface, leading to potential-dependent catalytic properties.

The conclusions made in this thesis shed light on the dynamically changing electrocatalyst structure under fuel cell operating conditions. We have shown that the surface chemistry of Pt and Pt alloys is rich, with a variety of involved oxidation states and subtle structural rearrangements. These structural changes have profound effects on the activity and long-term stability of the catalyst. Thus, our work provides a stepping stone towards understanding the atomic-level mechanisms that govern activity and stability in Pt and Pt alloy catalysts, paving the way towards better catalyst design and efficient fuel cells.

Nederlandse Samenvatting :

Operando spectro-elektrochemische studie van platina en platina-nikkel katalysatoren

Platina en platina legeringen gelden als de huidige state-of-the-art katalysatoren in brandstofcellen. Echter, hoewel deze materialen commercieel gebruik van brandstofcellen mogelijk hebben gemaakt zijn ze nog altijd de limiterende factor in de efficiëntie en levensduur van de brandstofcel. Inzicht in de moleculaire mechanismes die tot deze limitaties leiden zijn essentieel om optimale katalytische activiteit op de lange termijn garanderen. In lijn hiermee is de zuurstofreductiereactie op de brandstofcelkathode, waar de voornaamste degradatie en efficiëntieverliezen plaatsvinden, de afgelopen decennia het middelpunt geweest van intensief onderzoek. De ontwikkelingen in de afgelopen 20 jaar laten zien dat ondanks het aanzienlijke aantal H₂-brandstofcelvoertuigen op de weg er nog veel ruimte is voor verbetering in het katalysatorontwerp.

In dit proefschrift is de atomaire structuur van het elektrode-elektrolyt grensvlak van platina katalysatoren onderzocht onder de operationele condities van brandstofcellen, om een beter begrip te ontwikkelen van de structuur-activiteit-degradatie relaties van platina katalysatoren. Om dit mogelijk te maken hebben we modulaire röntgen-fotoelectronenspectroscopie opstelling opgebouwd, zoals besproken in hoofdstuk 2. Hiermee kunnen operando studies aan nano-gestructureerde elektrokatalysatoren in elk waterig elektrolyt worden uitgevoerd, inclusief die met opgeloste gassen. In de context van brandstofcellen maakt dit operando-studies waarbij de elektrode-elektrolyt-grensvlakstructuur wordt bestudeert onder brandstofcelkathode condities, ofwel in met zuurstof verzadigde elektrolyten. Hierdoor kan het gedrag van de elektrode, adsorbaten, en ionen uit het elektrolyt tijdens elektrokatalyse worden bestudeerd.

In Hoofdstuk 3 ontwikkelen we een dieper inzicht in de degradatie van Pt-nanodeeltjes tijdens het opstarten van brandstofcellen, waarbij snelle degradatie van de platina katalysator optreedt tijdens tijdelijke oxidatie en reductie van het elektrodeoppervlak. In onze studies naar het Pt-oxidatiegedrag onder gesimuleerde opstartomstandigheden laten we zien dat er vanaf het begin van de oxidatie een mengsel van de Pt^{δ+}, Pt²⁺ en Pt⁴⁺ oxidatietoestanden op de katalysator aanwezig is. Deze structuur wordt binnen enkele seconden gevormd, dat wil zeggen binnen de tijdschaal van de potentiaalpiek die optreedt tijdens het opstarten van de brandstofcel. We laten ook zien dat de oxiden die worden gevormd tijdens de opstartfase van de brandstofcel niet onmiddellijk wordt gereduceert in de daarop volgende fase (gebruik van de brandstofcel), wat waarschijnlijk een negatieve invloed heeft op de katalytische activiteit.

In Hoofdstuk 4 verleggen we de focus naar Pt₃Ni-katalysatoren, die in moderne brandstofcellen worden gebruikt vanwege hun hogere activiteit en stabiliteit vergeleken met puur Pt. In de

literatuur is aangetoond dat Pt-Ni-legeringen onder elektrochemische omstandigheden een Pt-“huid” vormen van enkele atoomlagen dik. In Hoofdstuk 4 hebben we de dynamiek van het Ni onder deze Pt-huid bestudeerd als functie van de aangelegde potentiaal, en het effect dat deze dynamiek heeft op de katalytische eigenschappen van de legering. We laten zien dat de Ni zeer mobiel is binnen de kern van de nanodeeltjes: bij hoge potentiaal komt Ni dicht naar het oppervlak en bij lage potentiaal beweegt Ni verder van het oppervlak af. Dit beïnvloedt elektronenoverdracht van de Ni atomen naar de katalytische tussenproducten op het katalysatoroppervlak, wat leidt tot potentiaalafhankelijke katalytische eigenschappen.

De conclusies uit dit proefschrift werpen licht op de dynamisch veranderende structuur van de elektrokatalysator onder de operationele omstandigheden van brandstofcellen. We hebben aangetoond dat de oppervlaktechemie van Pt en Pt-legeringen rijk is, met een verscheidenheid aan

betrokken oxidatietoestanden en subtiele structurele herschikkingen. Deze structurele veranderingen hebben diepgaande gevolgen voor de activiteit en de stabiliteit op lange termijn van de katalysator. Ons werk vormt daarmee een opstapje naar het begrijpen van de atomaire mechanismen die activiteit en stabiliteit in Pt- en Pt-legeringskatalysatoren bepalen, waardoor de weg wordt vrijgemaakt voor een beter katalysatorontwerp en efficiënte brandstofcellen.

Outlook

The ability to probe the electrode-electrolyte interface for Pt and Pt alloy catalysts and its relation to catalytic activity and stability hints at the immense potential of electrochemical XPS for the study of electrocatalysis. Once the challenge of a stable electrolyte film on the catalyst surface in a vacuum environment is overcome, X-ray spectroscopy becomes a very powerful and often highly surface sensitive tool, allowing us to follow different surface species in real-time via the different core levels they contain. In this regard, the conclusions presented in this thesis barely scratch the surface of the possibilities that the developed methodology offers.

In *Chapter 2*, we discussed our in house NAP-XPS and its versatility to incorporate a variety of reactions. Examples include biomass conversion, e.g. glucose oxidation on Pt, which is still in developmental phase in our lab and can offer an exciting start to my successor. In *Chapter 3*, we discussed the Pt oxidation under steady state and transient conditions. The same setup could be utilized to study surface degradation during accelerated stress tests (AST), surface structure changes under long term operation and the effect/lifetime of accumulated oxides formed during startup/shutdown stages. In *Chapter 4*, changes in catalyst properties due to subtle changes in catalyst structure in the Pt₃Ni alloy were discussed. Among many possible next steps in this project, one of the most promising seems to be the significantly higher HER activity in alloy catalysts, if conditioned properly. Spectroscopic examination of the surface/bulk structure responsible for the enhanced activity as well as long-term stability of this enhancement still need to be studied. Furthermore, other alloys such as Pt-Fe, Pt-Co and Pt-Au etc. could also be studied under similar conditions to paint a holistic picture of the effects of alloying under reaction conditions, contributing significantly towards our fundamental understanding of alloy electrocatalysis.

Perspectief op vervolgonderzoek

Deze thesis laat het potentieel zien van elektrochemische röntgen-fotoelectronenspectroscopie voor de studie het elektrode-elektrolyt grensvlak onder elektrokatalytische omstandigheden. Zodra de uitdaging van een stabiele elektrolytfilm op het katalysatoroppervlak in een vacuümomgeving is overwonnen, wordt röntgenspectroscopie een zeer krachtig en vaak zeer oppervlaktegevoelig hulpmiddel, waardoor de verschillende componenten van het elektrode-elektrolyt grensvlak in realtime kunnen worden gevolgd via de verschillende kernorbitalen die ze bevatten. In hoofdstuk 2 bespraken we de veelzijdigheid van onze röntgen-fotoelectronenspectroscopie opstelling en de verscheidenheid aan reacties die ermee kunnen worden bestudeerd. Een voorbeeld is de conversie van biomassa, zoals glucose-oxidatie op Pt, dat zich nog in de ontwikkelingsfase bevindt in ons laboratorium en een spannende start kan bieden voor mijn opvolger.

In Hoofdstuk 3 bespraken we de Pt-oxidatie onder potentiostatische en potentiodynamische omstandigheden. Dezelfde opstelling zou kunnen worden gebruikt om de degradatie van het oppervlak te bestuderen tijdens stresstests die gebruikt worden om de stabiliteit van Pt katalysatoren versneld te bepalen, om veranderingen van de oppervlaktestructuur bij langdurig gebruik te volgen, of om de reductie van oxide-restanten gevormd tijdens de opstart-/uitschakelfasen onder operationele omstandigheden te volgen. In Hoofdstuk 4 worden veranderingen in de katalysatoreigenschappen als gevolg van subtiele veranderingen in de katalysatorstructuur in een Pt₃Ni-legering besproken. Van de vele mogelijke volgende stappen in dit project lijkt een van de meest veelbelovende nader onderzoek naar de aanzienlijk hogere HER-activiteit van de legeringskatalysator naar aanleiding van geconditionering bij hoge potentiaal. Spectroscopisch onderzoek van de oppervlakte-/bulkstructuur die verantwoordelijk is voor de verhoogde activiteit, evenals de termijn van deze verbetering, moet nog worden bestudeerd. Bovendien zouden andere legeringen zoals Pt-Fe, Pt-Co en Pt-Au enz. ook onder soortgelijke omstandigheden kunnen worden bestudeerd om een holistisch beeld te schetsen van de effecten van legeringen onder reactieomstandigheden, wat aanzienlijk bijdraagt aan ons fundamentele begrip van de elektrokatalyse van legeringen.

E List of Publications

Chapter 2 is based on

Javed, H.; Kolmeijer, K.; Klein, N.; Trindell, J. A.; Schneider, G.; Mom, R. V. A Laboratory-Based Electrochemical NAP-XPS System for Operando Electrocatalysis Studies. *Vacuum* 2025, 231 (PA), 113755.
<https://doi.org/10.1016/j.vacuum.2024.113755>.

Chapter 3 is based on

Javed, H.; Knop-Gericke, A.; Mom, R. V. Structural Model for Transient Pt Oxidation during Fuel Cell Start-up Using Electrochemical X-Ray Photoelectron Spectroscopy. *ACS Appl Mater Interfaces* 2022, 14 (31), 36238–36245.
<https://doi.org/10.1021/acsami.2c09249>.

Chapter 4 is based on

Javed, H.; Kolmeijer, K.; Deka, N.; Sandhya, A. L. M.; Khalakhan, I.; Mom, R. V. The Potential-Dependent Structure of Pt₃Ni Alloy Electrocatalysts and Its Effect on Electrocatalytic Activity. *JACS (submitted)* 2025.

F Curriculum vitae

Hassan Javed was born on 4th of June, 1992 in Lahore, Pakistan. In 2014, he obtained his Bachelor of Chemical Engineering from University of Engineering and Technology, Lahore. After graduation, Hassan worked as a Process and Operations Engineer at Engro Fertilizers, Pakistan for 2 years. In 2016, he moved to Germany for his master's degree in Chemical and Energy Engineering from TU Berlin. He completed his master in 2019 after finishing his master's thesis with Dechema Forschungsinstitut, Frankfurt, on the topic of "*Synthesis of mesoporous carbon by soft template methods for PEMFC applications*". Hassan continued his academic journey in the Netherlands, where he completed a 1-year diploma in Chemical Product Design at the Faculty of Applied Sciences, TU Delft.

In 2020, he joined the group of Dr. Rik Mom at Leiden University. His project was a part of ECCM tenure track grant, and the research primarily focused on in-situ spectro-electrochemical studies of Pt and Pt alloy fuel cell cathodes. He had the opportunity to assemble the NAP-XPS at the Leiden Institute of Chemistry as a part of his PhD project. Hassan's project was mainly focused on investigating the stability and degradation of precious metal catalysts by bringing together electrochemical and X-ray spectroscopy techniques under realistic fuel cell conditions. In the 1st year of his PhD, he participated in ECCM Graduate School in Garderen and the 2nd year, SurfCat Summer School in Copenhagen, Denmark. At both these occasions, and later at the 23rd Netherlands Catalysis and Chemistry Conference in Noordwijkerhout, he presented his research findings as a poster. The results of Hassan's research are presented in this thesis as well as showcased in several national and international conferences, such as in December 2022 at APXPS in Windisch, Switzerland, in September 2023 at International Society of Electrochemistry in Lyon, France, and in April 2024 at Ecatalytix in Strasbourg, France.

During his PhD, Hassan also supervised several bachelor and master's students towards their final projects as well as assisted in LST (Life Science and Technology) and BFW (Biofarmaceutische Wetenschappen), where a small group of bachelor students perform a joint project in a research lab. Hassan also followed several transferrable skills courses, notably the 'High impact writing course' of the HRSMC (Holland research School of Molecular Chemistry and courses like scientific conduct and effective time management offered by HRM-learning and development.

G Acknowledgements

Finishing my PhD has been one of the most challenging but rewarding experiences of my academic career. I would like to extend my heartfelt gratitude to everyone who has guided and supported me through this journey.

First and foremost, I would like to express my deepest gratitude to Prof. Marc Koper and Dr. Rik Mom for giving me the opportunity to embark on a PhD journey as one of Rik's first PhD students. Over the years, I have received in depth guidance, knowledge and endless patience from him. Being an engineer by profession, I was given the opportunity to work on a project which beautifully combined the engineering aspect with the fundamental science during my PhD. I would also like to acknowledge his truly high standards against which my work has been judged; was difficult at times, but looking back, I am thankful because they only made me a better scientist.

I am also thankful to my colleagues, past and present, that contributed their valuable effort towards the success of my work. I would like to thank Akansha Goyal, for teaching me how to build an RHE and many other basic things around the lab. I would like to thank Arthur Shih, for his insightful late-in-the-evening lab discussions when I was struggling with my experiments. Francesc, for his insightful knowledge regarding Pt and its degradation, Kees for an endless supply of graphene. I would also like to extend my gratitude to Jan Rodriguez and Nipon Deka for their support during the beamtimes.

Furthermore, my close friends whose company made it possible for me to keep my sanity during the toughest of the hours; Aleksandra, Julia, Rafael, Taissa, Nicci, Arthur, Aude and others also deserve my gratitude. A special thanks to Dr. Zeenat Hameed for her support and care, and making this journey bearable. All of you have always been there to help and bring an uplifting attitude.

Concluding, I would love to thank my parents for their unwavering support. Their sacrifices have brought me this far and I owe them every bit of the success and prosperity that I have today.